# From Elastic Electrodes to Fabric Systems

by

Juliette Marion

B.S., Engineering, Ecole Polytechnique (2015)
M.S., Materials Chemistry, Ecole Polytechnique (2016)

Submitted to the Department of Materials Science and Engineering
in partial fulfillment of the requirements for the degree of

Doctor of Philosophy in Materials Science and Engineering

at the

MASSACHUSETTS INSTITUTE OF TECHNOLOGY

September 2022



Author .....
Department of Materials Science and Engineering
July 19, 2022

Certified by .....
Yoel Fink
Professor of Materials Science and Engineering
Professor of Electrical Engineering and Computer Science
Thesis Supervisor

Certified by .....
Polina Anikeeva
Professor of Materials Science and Engineering
Professor in Brain and Cognitive Sciences
Thesis Supervisor

Accepted by .....
Frances Ross
Chairman, Department Committee on Graduate Theses

**From Elastic Electrodes to Fabric Systems**

by

Juliette Marion

Submitted to the Department of Materials Science and Engineering
on July 19, 2022, in partial fulfillment of the
requirements for the degree of
Doctor of Philosophy in Materials Science and Engineering

## Abstract

Textile-based electronics hold promise for wearable sensors and devices, as well as flexible and conformable electronics. In recent years, research has focused on realizing specific devices or even system level functions within a single fiber. Harnessing thermal drawing, significant developments in fiber functionality have been achieved over the last couple of decades. However, certain essential properties of device containing fibers still require attention. In particular, yarns in an electronic textile must withstand large strains and bending, while maintaining their functional integrity. As metal electrodes are necessary to connect devices over hundreds of meters of fiber, they preclude fiber devices from having the elasticity necessary to sustain weaving, knitting, and daily use.

In this thesis, we investigate the use of in-fiber structural elasticity as a mean to build elasticity in thermally drawn functional fibers. We explore thermal drawing of elastomers and expose how the drawing stress can affect the fibers mechanical properties. We propose two approaches to achieve metal electrodes demonstrating high elasticity ($> 10\%$), through buckling of a metal microwire within a cavity, or through twisting of a fiber to yield helical metal electrodes. We later examine the mechanical constraints involved in weaving and knitting, and enrich the list of principles for fiber design, to limit friction and kinking. We finally devise a method to connect micro-devices in fibers via buckled electrodes, and demonstrate two fabric systems: a woven, three-dimensional optical antenna, and a knitted garment able to detect localized changes in skin temperature.

Thesis Supervisor: Yoel Fink
Title: Professor of Materials Science and Engineering
Professor of Electrical Engineering and Computer Science

Thesis Supervisor: Polina Anikeeva
Title: Professor of Materials Science and Engineering
Professor in Brain and Cognitive Sciences

# Acknowledgments

"You anoint my head with oil, my cup overflows" (Psalm 22)
In so many ways have I been blessed all along my life, and more specifically during these years of PhD. In particular, many blessings came through people whose path crossed mine.

I still do not understand exactly how I ended up doing my master thesis in Prof. Yoel Fink's lab, but it happened, and it made a tremendous difference in my life. I am infinitely grateful to Yoel, for bringing me in for 6 more years at MIT, and for being the mentor and friend he became to me. If the scientific and academic teaching was precious (for example this openness towards apparently crazy idea combined with an exhausting scrutiny towards every result), even more important was the role he played to help me grow as a person. Not fearing to point to my weaknesses, but always supportive, caring, deeply touched by things and always here when life was rough. I will miss our discussions about faith and life. And part of our disagreements, but only the philosophical ones, not the scientific ones. I rejoice in thinking that if I will not call you my PI any more, I will keep calling you my friend.
A year after starting at MIT, I met Prof. Polina Ankikeeva. Through her mentoring, she gave me advice, a broader scientific scope, but most importantly an example. An example of a great mentor who really cares, takes the time, digs deep into the details and the science, while also caring for your life outside work and your peace of mind. A flawless intellectual honesty. When it is my turn to be a mentor, I wish to imitate your beautiful mix of toughness and tenderness,.
From Prof. Jung Tae Lee who taught me how to draw my first fiber, to my UROP student Kirmina Monir spending hours weaving an antenna with me, I have shared the joys and hardships of research whith many. Special thanks to Dr. Michael Rein, Prof. Tural Khudyiev, Prof. Chong Hou, Dr. Rodger Yuan, Dr. Ben Grena, Dr. Gabriel Loke, Prof. Wei Yan, Grace Noel (bearing with me at work and at home!), Nikhil Gupta, Henry Cheung, Dr. Andres Canales, Dr. Marc Joseph Antonini, Atharva Sahasrabudhe, Rajib Monir, Dr. Caroline Apra and Harisson Allen for the good

work shared together. I am also especially grateful to David Bono, Mike Tarkanian, Shaymus Hudson and James Hunter for their patience, availability and help to... make anything work. They taught me that, with enough creativity, you can construct any apparatus you need. And more importantly, it is thanks to them that I feel at home in the department. Many thanks to Tina Gilman, Cindy Higgins, Molly Kruko and Catherine Bourgeois for dealing with our administrative mess with such patience and gentleness. Prof. Rohan Abeyaratne and Prof. David Parks taught me the basics of mechanics, which I knew nothing of, and which would be at the heart of my PhD. They teach incredibly well. Thank you for sharing science with energy and clarity, allowing us to take part in it.

Life in Cambridge has been rich way beyond MIT. I am deeply grateful for the beautiful friendships built here. Through faith, adventures, parties, these years were filled with joy, making a wholesome beautiful life. Thanks to the saint Paul's, Saint Mary's and the Emmanuel communities, thanks to the Zigotos, the French crew v1, v2, v3, v8000... Thank you for your love, your prayer, your help in crises, your dancing until dawn, your stupid jokes, your sport enthusiasm... thank you for making Cambridge my home. A very special thanks to the Kinnaird street ladies, Aileen, Elisa, Grace and Angie. This home has seen laughter, drama, hard work and such benevolence that after moving out it still feels like home whenever I come back.

To my family, especially my parents and Mamine et Daddy: merci. You believed in me way more than I did, and you taught me to aim for excellence while keeping a childlike mind. I strive to imitate your humility and your generosity. Thank you for the countless hours of phone calls, that kept us close to each other although an ocean apart.

Tanguy, one could not ask for more support, love and tenderness than you give. A whole life shared together is the most beautiful perspective that I have and will ever have. Thanks be to God.

# List of abbreviations

**COC** Cyclic Olefin Copolymer

**COCe** Cyclic Olefin Copolymer elastomer E-140

**CPE** Conductive Polyethylene

**HAY** Helical Auxetic Yarn

**LED** Light Emitting Diode

**PC** Polycarbonate

**PDMS** Polydimethylsiloxane

**PEDOT:PSS** Poly(3,4-ethylenedioxythiophene):Polystyrenesulfonate

**PMMA** Polymethyl Methacrylate

**PTFE** Polytetrafluoroethylene

**PVDF** Polyvinylidene Fluoride

**SEBS** Cyclic Olefin Copolymer

**TPE** Thermoplastic Elastomer

**TPU** Thermoplastic Polyurethane

# List of symbols

| | |
|---|---|
| $a$ | Tube diameter |
| $\alpha_0$ | Helical angle |
| $c$ | Length of line contact |
| $\Delta$ | End displacement |
| $E$ | Young's Modulus |
| $\varepsilon$ | Strain |
| $\varepsilon_{clad}$ | Cladding strain |
| $\varepsilon_\Delta$ | Relaxed cladding strain |
| $\phi$ | Draw-down ratio |
| $\varphi$ | Filling factor of a fabric with fibers |
| $h$ | Distance between the walls = gap width |
| $\eta_{metal}$ | Excess metal length |
| $I$ | Area moment of inertia |
| $\kappa$ | Curvature |
| $L$ | Arc length of the bent portion of the wire |
| $L_0$ | Initial cladding length |
| $L_f$ | Fiber length |
| $L_{metal}$ | Metal trace length |
| $n$ | Optical refractive index or Number of buckles |
| $\nu$ | Poisson ratio |
| $P$ | Compressive load |
| $p$ | Pitch of the helix |
| $\rho$ | Radius of curvature |
| $r$ | Radius of the wire |
| $r_h$ | Radius of the helix |
| $U$ | Mechanical energy |
| $v_{capstan}$ | Speed of the capstan (linear speed) |
| $v_{feed}$ | Speed of preform feeding |
| $\chi$ | Thickness to radius ratio of a tube |
| $\zeta$ | flattening ratio of a tube |

# Contents

# List of Figures

# Chapter 1

# Introduction

## 1.1 From fibers to fabrics

### 1.1.1 Background

In Washington DC, on the Mall, one finds, side-by-side, the National Museum of the American Indian, and the Smithsonian National Air and Space Museum. If, in the course of a museum-athon, you happen to hop from the former to the latter, you might need a little time to adjust to the switch in topic. After contemplating a piece of woven garment from Mexico, AD 700-1475 (catalog number 8/3811), you are now facing a spacesuit. The beauty of it though, is that, if you look close enough, they look so similar...

Most fabrics are hierarchical structures, constructed from fibers and yarns. Fibers are the basic unit of the fabric. They can be either short (staples) or long continuous filaments of the fabric's material. Natural fibers develop in fiber form from plants, animals or minerals while manufactured fibers are made from chemical compounds. Multiple fibers are then assembled together, to form a yarn (except in non-woven fabrics, which are not covered in this work). Yarns are turned into fabrics, using various techniques such as weaving and knitting. Each level brings additional degrees of freedom, from materials choice to the degree of twisting of the yarn to weaving pattern, which results in the stunning variety in appearances and properties of fabrics.

But looking at an ancient piece of cloth or at the orthofabric of the spacesuit [1], one will distinguish the same hierarchy, the same weaving process and, under the microscope, microfibers, of wool for one and of Kevlar for the other.

For the longest time, textile innovation has focused on creating new structures of yarns and fabrics. Despite being ubiquitous to our environment, fabrics remained limited to a narrow range of applications, either structural or protective. In the early 2000's, finally, the textile world met with the fast developing and expanding world of electronics. Fabrics started to be engineered to encompass device-like functionalities ranging from mechanical sensing [2, 3, 4] to energy harvesting and storage [5, 6, 7, 8]. This new field of smart fabrics, has since been growing exponentially. One finds an obvious illustration of this growth, in research, by looking at the number of scientific publications per year that include the terms "smart fabric" or "intelligent textile" (Figure 1-1).

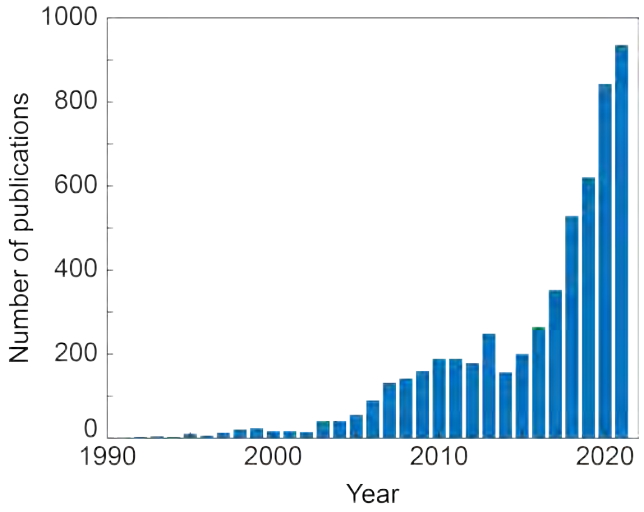


Figure 1-1: Number of scientific publications per year that contain either "smart fabric" or "intelligent textile". Source: Web of Science.

More recently, the path to realizing functional textiles has moved down one fabric length scale, shifting from devices added on top of a fabric to devices that are actually embedded into the yarn itself, and will constitute the fabric [9, 10]. This approach has the advantage that, compared to weaving or knitting bare interconnects with regular yarns, or attaching devices to the surface of fabrics, encapsulating both elec-

trodes and devices inside the cladding of a single fiber grants enhanced mechanical and environmental protection and allows for increased electrode and device density. Much of the works in fiber-based electronics have focused on achieving specific device functions, but some more generic aspects of the fibers still require attention. This work focuses on one of those characteristics: the mechanical properties of functional fibers, in particular elasticity. We show why elasticity is a fundamental requirement for textile fibers and how to achieve it concurrently with sophisticated functionalities.

### 1.1.2 A key requirement for elasticity

When considering elasticity in the context of fabrics it is important to distinguish between contributions of the disparate hierarchical levels constituting the fabric: the structure of the fabric, woven or knitted, grants it elasticity [11, 12], but this structural elasticity, though valuable, does not negate the importance of the fiber's elasticity. For example, a monofilament yarn inside a woven textile can experience almost half of the elongation endured by the fabric beyond 10% fabric strain [12]. This is not only a matter of comfort for the user, but also a requirement to maintain the integrity of the fiber under the mechanical constraints of weaving [13] or knitting [14] and daily use. More details are given in chapter 6. Fabric manufacturing will notably impose stretching and bending on the fibers, while fabric usage necessitates a long cycling life at low strains for the durability of the fabric, and good flexibility for comfort. The table below summarizes the types of mechanical constraints and relevant figures of merit for our fibers.

| Constraint | Figures of Merit (unit) | Impact |
|---|---|---|
| Stretching | Young's Modulus (MPa)<br>Elasticity (%) | Manufacturing<br>Comfort |
| Bending | Young's Modulus (MPa)<br>Diameter (mm) | Manufacturing<br>Comfort |
| Cyclic loading | Fatigue life (# cycles) | Durability |

It is important, here, to specify what is meant by elasticity. As Lipomi [15] pointed

out, it is common, in the field of stretchable electronics, to find figures of merit at least as stretchable as the devices themselves. This lack of accuracy leads to confusion and the impossibility to compare between different devices. In this work, we stick to the original meaning of elasticity: the maximum amount of elongation that can be recovered by the material when a load is removed. Yield strain is a synonym. In particular, this is different from the strain to failure, which is the maximum elongation that a material can undergo without breaking. So, when we describe a material, electrode, fiber or else as "highly stretchable" or having a "large elasticity", we refer to elasticity and not strain-to-failure.

In this work, we will then aim at making functional fibers that exhibit:

- Low Young's Modulus: $\leq$ 100MPa
- Large elasticity: $\geq$ 5%
- Small diameter: $\leq$ 1.5mm
- Long fatigue life at relevant strains: $\geq$ 1000cycles

## 1.2 Multimaterial fiber drawing

### 1.2.1 Background

In the past two decades, research on functional fibers has worked towards a complete change in the technical abilities and variety of applications that are possible in fibers: from a passive device to a multimaterial platform that can embed active components, sense and interact from a single fiber to a network level. Traditional fiber-making processes used in textile, such as melt-spinning or extrusion, quickly showed limitations in their ability to combine disparate classes of materials, and to create arbitrary cross-sectional geometries, two essential features for functional fibers. In parallel, in a completely different field of application, the thermal drawing process has been developed and perfected to create sophisticated multimaterial optical fibers, for example with the invention of photonic bandgap fibers in the 2000's [16]. During the past 15 years, this process has been exploited beyond waveguides, enabling fiber functionali-

ties ranging from light detection [17] and energy storage [18, 19] to biosensing [20]. In particular, thermal drawing has allowed for the introduction of novel materials and novel geometries in fibers at a micrometer to nanometer scale [21, 22], which makes it an excellent candidate for fiber processing for next generation textiles.

### 1.2.2 Thermal drawing process

#### Overview

The process is depicted in figure 1-2. Thermal drawing starts with the fabrication of a macroscopic version of the fiber called a preform. The preform is fed into a vertical furnace, which softens the materials into a high viscosity fluid. Tension is applied to the bottom part of the preform, first by hanging weights, then by the rotation of a capstan. This tension is the motor of size reduction, which happens in a region in the furnace called the necking zone, where the viscous fluid deforms into meters of microscopic fiber. Below the necking zone, outside of the furnace, the fiber solidifies. Under a stable draw, the fiber will show the same cross-sectional shape as the preform and minimal radial variations. In this work, we focus on drawing of polymer fibers and leave aside glass fibers.

#### Preform

The preform has the same composition and geometry as the final fiber but is much thicker and much shorter in length. The main material, a polymer which carries the structure, is called cladding. Usual cladding materials are Polycarbonate, Polyethylene, Cyclic Olefin Copolymer... Once the multiple parts of the preform are assembled and consolidated together, usually by heating, the preform is drawn in the draw tower. Because the cladding represents the main part of the preform in weight, it dictates the draw temperature.

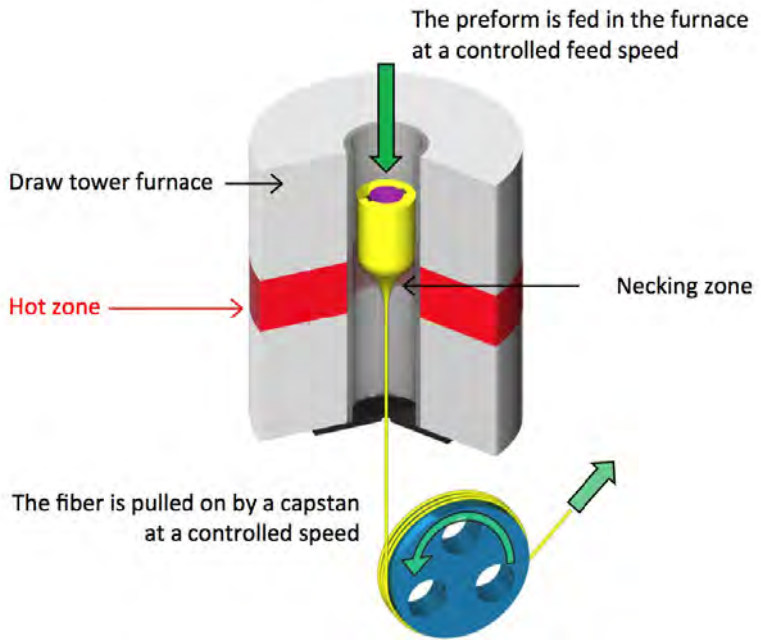


Figure 1-2: Schematic of the thermal drawing process. Figure courtesy of G. Lestoquoy.

### Drawing

The temperature in the furnace is controlled in three different zones: the preheating zone, the necking zone and the cooling zone. Temperatures are set so that the cladding material can flow but remains viscous enough to retain the structure. A viscosity between $10^3$ and $10^6$ Pa.s is needed for successful drawing. The preform is fed into a furnace at a controllable speed $v_{feed}$. At the bottom of the tower, a capstan pulls the materials together at a controllable speed $v_{capstan}$. The difference between $v_{feed}$ and $v_{capstan}$ generates a tensile stress that allows for axial elongation and cross-sectional reduction. Concurrently, thanks to the materials viscosity, cross-sectional stress develops, which will maintain the geometry while drawing. Conservation of volume dictates the change in cross-sectional dimension from the preform to the fiber, defining the draw-down ratio as:

$$\phi = \frac{d_{preform}}{d_{fiber}} = \sqrt{\frac{v_{capstan}}{v_{feed}}} \tag{1.1}$$

where $d$ refers to a cross-sectional dimension. A set of lasers measures the size of the final fiber while a tension meter records tension in the fiber. This immediate feedback not only informs on the stability of the draw (variations in fiber diameter) but also allows for adjusting the different parameters, namely speed and temperatures. Notably, both types of knobs have a direct effect on the draw tension, either by directly controlling it or by affecting the materials viscosity.

### 1.2.3 Materials requirements

Thermal drawing imposes a few constraints on the choice of materials.

Concerning the cladding material, two constraints arise:

1. The cladding should be a thermoplastic polymer, that can deform without degrading upon heating.
2. There needs to be a large enough temperature window where the material viscosity lies between $10^3 - 10^6$Pa.s.

In particular, these conditions leave aside all thermoset polymers which would degrade, as well as most non-amorphous polymers, whose drop in viscosity upon heating is too sharp to find a stable draw temperature, as illustrated in figure 1-3.

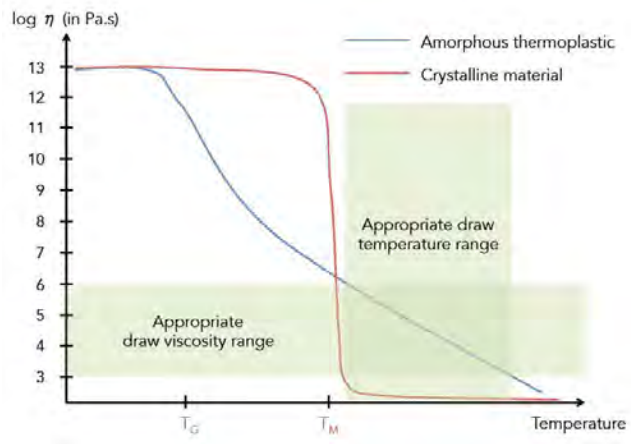


Figure 1-3: Comparison of the rheological behavior of an amorphous and a crystalline polymer. The amorphous material shows a range of available draw temperatures, while the crystalline material does not. Figure courtesy of B. Grena

Other materials, embedded within the cladding, need to be able to withstand the draw temperature (usually 150-300°C) without degrading. In terms of flow conditions, three possibilities emerge.

1. As a general rule, materials with similar viscosity as the cladding at the draw temperature will be co-drawable.
2. If a material has a much lower viscosity than the cladding (molten solder, crystalline polymer), it needs to be fully enclosed by materials with higher viscosity. Else it will pool under gravity and/or change shape to accommodate surface tension.
3. If a material has a much higher viscosity than the cladding, it will not deform, resulting most of the times in failure. On should note, though, that solid micro particles [23] or microchips [24] can be inserted in the preform. They will not deform during the draw but flow along with their encapsulating material.

Despite these constraints, thermal drawing enables the incorporation of a large range of materials from polymer composites [23, 25] and metals [20, 26] to semiconductors [17]. Submicron features extending kilometers in length have been obtained, demonstrating both the versatility and scalability of thermal drawing.

## 1.3 Thesis Outline

In this thesis, we wish to build a framework, that guides the design and fabrication of functional fabric systems using thermally drawn fibers, understanding that the mechanical properties of fibers are key to their use in textiles. From the fundamentals of drawing elastomers, to designing elastic electrodes, to knitting and weaving fabrics, to actual systems, we explore each step of design and fabrication. We want to derive fundamental principles of fibers and fabrics engineering, while remaining general enough to be agnostic to the specific function, materials or shape of the final object.

In chapter 2, we start with the elementary step of drawing elastomeric materials to make elastic fibers. After reviewing the fundamentals of rubber elasticity, we analyze

their consequences for thermal drawing. We design and fabricate elastomeric fibers, including multimaterial elastic optical fibers.

In chapter 3, we highlight the need for electrodes with large elasticity in functional fibers. We review the different materials and approaches that have been developed, both in and outside of thermal drawing.

In chapter 4, we develop a method to make fibers with buckled metallic electrodes capable of up to 90% elasticity. We present an analytical model of the buckling process and an experimental characterization of the fibers. We show that the design of these fibers is a multi-parameter problem, which gives this method a great adaptability.

In chapter 5, we demonstrate in-fiber helical metal electrodes that can reach 10% elasticity. We characterize the fibers through experimentation, and we establish how this method allows to control for the fibers mechanical properties.

In chapter 6, we embed our fibers into fabrics using weaving and knitting. We analyze the constraints that these techniques apply onto fibers and define the conditions that the fibers have to meet to survive the process.

In chapter 7, we shift our focus from mechanical properties to functionality. We establish a method to incorporate micro-devices connected via buckled electrodes into fibers. We use this method to demonstrate two fabric systems. The first one is a woven, three-dimensional optical antenna. The second system is a knitted temperature sensing fabric able to monitor body temperature.

# Chapter 2

# Thermal drawing of elastomers

The fabrication of elastic functional fibers for smart fabrics necessarily starts with the ability to draw elastomers. These will be needed as cladding materials and sometimes also as the active material. In this section we present thermoplastic elastomers and the modalities of drawing them. We also present the application a solely elastomeric optical fiber as a medical implant.

## 2.1 Thermoplastic elastomers

### 2.1.1 Rubber elasticity

The first discovered elastomer is natural rubber, already used by Mesoamerican cultures as early as 1600 BC, which gave its name to what is now called rubber elasticity. The origin of rubber elasticity is the thermodynamics of long polymer chains. When the material is at rest, the chains are in a folded, high entropy state. This is the naturally favorable configuration. When the material is stretched, the polymer chains unfold, elongate and align in the direction of loading, and their entropy decreases. Upon removal of the external load, they will fold back into their initial state. However, the fluctuations of the chains would lead to the material falling apart if the chains were not held together by fixed points. Topological entanglement between long polymer chains creates a first type of fixed points, but these are lost upon large

deformation as the chains slip against one another. Hence, elastomers are designed to have cross-links between the chains, which restrict the relative movement of the chains and force the polymer back into its original configuration after elongation. The modulus of an elastomer increases with the density of cross-links. For example natural rubber, as collected from the rubber tree, is an entangled network of polymer chains. After a process called vulcanization, covalent bonds are created between the chains, thus creating permanent cross-links. These cross-links are permanently destroyed if the material is heated above its melting point. This makes vulcanized rubber a thermoset elastomer. On the contrary, when the cross-links are heat-reversible, the polymer is a ThermoPlastic Elastomer (TPE).

### 2.1.2 Structure of TPEs

While there is active research on heat reversible chemical cross-links [27] , current TPEs mostly rely on the mixing of two micro-separated phases, a hard one and a soft one, either through blending of different polymers or through segmented co-polymerization [28]. The soft phase is usually an amorphous phase made of long linear chains and gives the polymer its flexibility and elasticity at working temperature. The hard phase can be either a crystalline block between the soft segments or a sterically hindered block (such as polystyrene) that acts as a physical cross-link between the chains, providing shape recovery. Above the melting temperature ($Tm$) or glass transition temperature ($Tg$) of the hard phase, the polymer can be formed in any desired shape. Below that temperature, it behaves like a cross-linked elastomer. In this work, we used two TPEs: a semi-crystalline cyclic olefin block co-polymer from TOPAS, COC e-140 (COCe, $Tg \leq 90$°C, $Tm = 84$°C, $E = 50$MPa) and an amorphous co-polymer of poly(styrene-b-(ethylene-co-butylene)-b-styrene) from Kraton, SEBS G1657 (SEBS, $Tg \simeq 120$°C, $E = 2{,}4$MPa). They have been chosen for their advantageous mechanical properties (stretchability >500%, low Young Modulus) and optical properties (good transparency).

### 2.1.3 Drawability

The recent development of TPEs has opened new possibilities for the processing of elastomers. While thermoset elastomers have to be polymerized directly into their final shapes, TPEs can be reshaped at will through processes such as melt-molding, extrusion, thermoforming... The first mention of thermal drawing of an elastomer was by Lu et al. [29] in 2017, using COCe, but it was drawn inside a fiber made of a PMMA cladding. The use of an elastomer (SEBS) as a cladding material was reported later by Qu and al. [30]. The late emergence of TPEs as cladding materials is explained by the fact that, beyond thermoplasticity, they also need to match the rheological criteria mentioned in section 1.2.2. This has to be determined polymer by polymer. Let us look at the two materials chosen in this study.

#### SEBS

Qu et al. [30] identified SEBS as being thermally drawable by comparing its measurement of shear viscosity depending on temperature, with that of polycarbonate (PC), which is a common cladding material in thermal drawing. In their work, they suggest a criterion for drawability that is more precise than a simple range of viscosity: the loss modulus should change slowly with temperature, crossing over the storage modulus which decreases rapidly. Thermal drawing is an extensional flow, so extensional viscosity seems like a better criterion. Nonetheless, this shear viscosity approach has shown good results in identifying drawable elastomers. In our work, SEBS has been successfully drawn between 200°C and 250°C. It is a versatile cladding material, that allows for fibers with sophisticated cross-sections [30, 4], and its relatively high draw temperature makes it compatible with a large range of materials including liquid metal [30], CPE or PVDF [23].

#### COCe

It has long been believed that only amorphous polymer could serve as cladding materials in thermal drawing [21]. Hence COCe was only drawn inside another cladding

material [29, 31]. We experimentally invalidated this theory by drawing COCe as a cladding material with various cross-sections [32]. This points to the fact that, more than the type of microstructure of the polymer, what matters is its rheological behavior. COCe has not been tested for the criterion defined by Qu and al., but it was successfully drawn from 115°C to 240°C. It could be used as a fiber cladding for other materials such as CPE and PVDF.

## 2.2 TPEs and extensional flow

Although SEBS and COCe could be drawn into fibers, it is not obvious that these fibers would exhibit the same elasticity as the bulk polymers, because of the extensional nature of thermal drawing.

Drawing and extrusion of semi-crystalline polymers is a well-studied problem [33]. During these extensional processes, we observe a global alignment and elongation of the structure along the drawing axis. On the one hand, the crystallites tend to break down into smaller pieces and align in the direction of the draw. This is the transition from lamellar to microfibrillar structure. For even higher extensions, the crystallites might fully unfold, leading to a complete alignment of the polymer chains. On the other hand, the amorphous chains are also oriented in the direction of elongation, and partly elongated in the final fiber.

A similar phenomenon arises when drawing TPEs, either amorphous ones or semi-crystalline ones. For TPEs, elasticity results from the ability of the chains in the soft phase to extend, so, as a direct consequence of chains alignment and elongation, the final fiber can loose in elasticity and exhibit a higher Young's Modulus than the bulk polymer. The degree of chain elongation and alignment depends on the stress during the draw process, which is governed directly by the draw temperature and the capstan speed. Then, one must especially find a balance for the draw temperature: if the temperature is too high, the polymer is not viscous enough and the structure of the preform is not maintained; if the temperature is too low, the draw stress is too high, leading to excessive chain elongation and loss of elasticity.

This also means that one can use the draw process to tune the mechanical properties of the final fibers. By varying the draw stress, we could purposefully control the percentage of chain alignment and elongation. Chain alignment can be seen as an artificial increase in the degree of crystallinity of the soft phase. Hence the drawn fiber can be considered as a composite material with three components: the hard phase, the amorphous soft phase and a share of crystallized soft phase, organized as depicted in figure 2-1. Using the classic rule of mixtures to calculate the Young's Modulus of a composite material, and neglecting the Young's Modulus of the soft amorphous phase ($E_a$) one gets:

$$E_{fiber} = \frac{\beta E_c}{1 - \alpha + \alpha\beta\frac{E_c}{E_H}} \tag{2.1}$$

where $\alpha$ is the ratio of hard phase, $\beta$ is the ratio of soft phase that has crystallized, $E_H$ is the Young's Modulus of the hard phase and $E_c$ is the Young's Modulus of the crystallized soft phase.

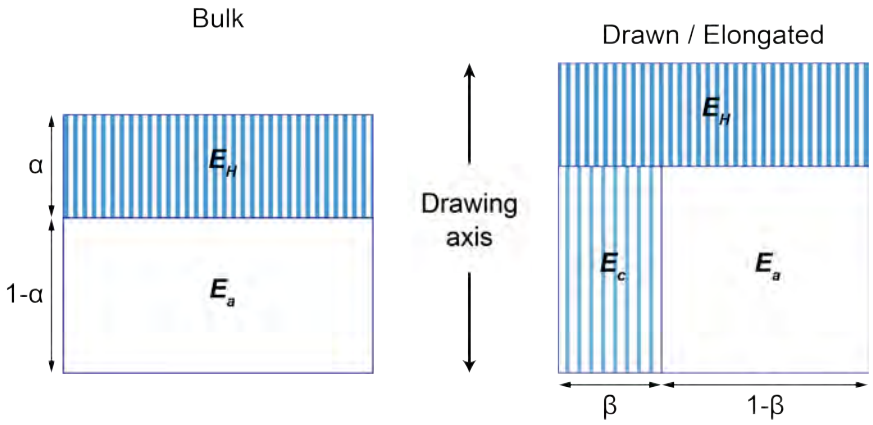


Figure 2-1: Modeling of a TPE fiber as a composite material. $\alpha$: fraction of hard phase. $\beta$: fraction of soft phase that has crystallized.

In their work, Qu and al. [30] report a visible alignment of the hard polystyrene phase when drawing SEBS at 145°C versus 220°C. However they did not measure the Young's Modulus of the different fibers. Here, we investigated the effect of the draw stress on COCe fibers by varying the temperature of the draw. Results are presented in figure 2-2a. At low temperature, the drawing process generates so much chain

alignment that it becomes closer to a solid tensile deformation than to a viscous flow, as can be seen on figure 2-2b by comparing the loss of transparency due to chains alignment, on images of fibers drawn at 240°C, drawn at 240°C and elongated up to 300%, or drawn at 115°C.

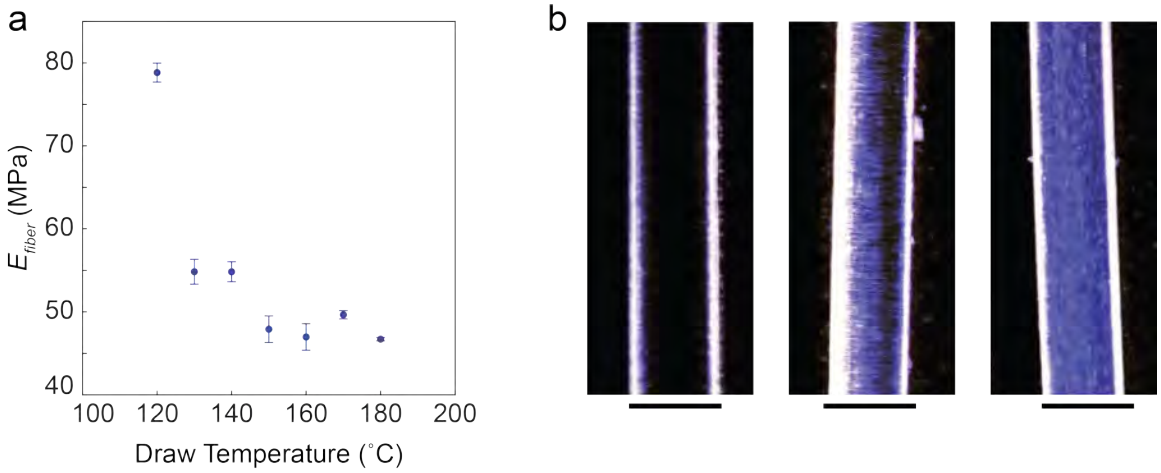


Figure 2-2: (**a**) Young's Modulus of COCe fibers depending on the draw temperature (Test performed with DMA Q800) (**b**) Optical microscope images of fibers. Left: drawn at 240°C. Middle: drawn at 240°C and elongated by 300%. Right: drawn at 115°C. (Scale bars 700$\mu$m)

## 2.3 Elastic optical fibers

### 2.3.1 Background

A new and exciting area of application for functional fibers and fabrics is medical implants. In particular, progress in biochemistry and genetics gives us new tools, such as optogenetics [34], to interrogate neural pathways and study their behavior and transformations in case of a malfunction. Optogenetics requires custom neural implants that can carry light, deep within the tissues, in particular in the brain and spinal cord. Such implants have seen various recent developments in terms of functionalities, performances, and ability to access deeper tissues [35] A main challenge remains their long-term use, which often results in failure of the implant, that loses one or all of its functionalities [36]. A reduced mismatch between the mechanical properties

of the implant and of the tissues has been shown to reduce the risk of mechanical failure of the implant, the damage to the surrounding tissues and the foreign body response by which the body rejects the implant [35]. Thermally drawn fibers have been demonstrated as neural implants in the brain [20] as well as in the spinal cord [37]. Polymer optical fibers exhibit a low flexural modulus compared to traditional glass fibers and offer a little invasive geometry, which makes them good candidates for neural implants. However, traditional fiber materials such as PC or PMMA still exhibit Young's Moduli order of magnitudes higher than biological tissues (GPa vs kPa) and these fiber cannot elongate to accommodate tissue movements.

A few examples of soft and stretchable optical fibers have been demonstrated, using elastomers [38, 39, 40] or hydrogels [41]. These are mostly proposed as strain sensors, either using the strain-dependence of optical loss [39, 40], or by integrating photonic structures [38], whose wavelength-dependence will vary with strain. However, their fabrication processes usually require a large number of steps for the production of a short length of fiber. One example of thermally drawn optical fibers is referenced in the literature using SEBS as a core material [30]. Optical waveguides made out of TPEs present an obvious challenge: to have a good optical transmission, a material should be as homogeneous as possible. TPEs are intrinsically composed of two phases. That is why TPEs will exhibit an optical loss even higher than other polymers: Rayleigh scattering on the blocks of the hard phase will add to usual molecular absorption. This is especially problematic when small cross-sections are required. In the case of thermal drawing, molecular alignment can also increase the birefringence of the fibers.

### 2.3.2 Results

We developed a stretchable optical fiber that can be used for biological applications requiring to deliver light in the body. Elasticity and size are more constraining requirements than optical transmission, knowing that the fiber will have to carry light along about 20cm only. However, the transmission should be good enough so that the power required for enough light to go through the fiber remains reasonable and

does not damage the fiber through heating. We also want the total internal reflection to be efficient enough so that no light is scattered by other elements that could be incorporated in the outer part of the fiber (for example electrodes).

We managed to thermally draw a high elasticity, step-index optical waveguide. The core of the fiber is made out of ECOC ($n$ =1.53) and the cladding is SEBS ($n$ =1.43). These two polymers present various properties that make them suitable for an elastic optical fiber:

- They are both thermally drawable TPEs, with similar draw temperatures.
- They have a relatively high optical index contrast.
- They have similar chemical functional groups, which should provide a good adhesion between the core and the cladding.

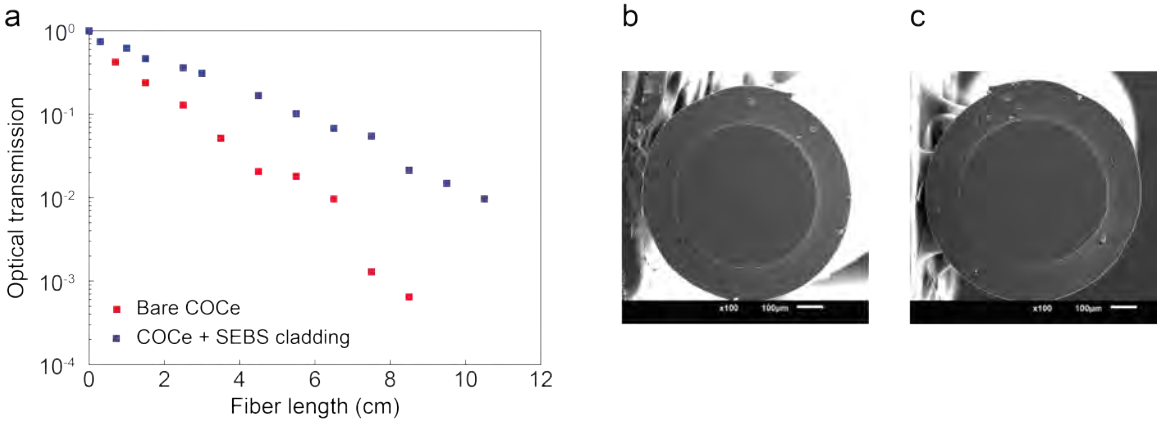


Figure 2-3: (**a**) Measurement of the decibel loss of a 350$\mu$m COCe fiber with or without an SEBS cladding (**b**,**c**) SEM images of the cross-section of the cladded fiber used in (a), before (b) and after (c) 900 cycles at 20% strain

The fiber was drawn at 220°C and we were able to reduce its diameter down to 200$\mu$m, which is less than half what is reported in literature [30]. Characterization of a non-optimized fiber gave a decibel loss of 1.87DB/cm with a 350$\mu$m core, for $\lambda$ =473nm (Figure 2-3a). By comparison, a 350$\mu$m ECOC fiber without cladding showed a decibel loss of 3.53 DB/cm. Better optical losses are reported in literature but we believe that our fiber can easily be optimized to decrease this loss, at least

by eliminating impurities due to processing. We also performed cyclic stretching on this fiber. As we see in figure 2-3b, there is no sign of delamination after 900 cycles at 20% strain.

## 2.4 Discussion and next steps

In this chapter, we studied the use of TPEs in thermal drawing. By going back to the fundamentals of rubber elasticity, we unveiled the morphological changes imposed upon the polymeric chains by an extensional flow, and their impact on fiber elasticity. We demonstrated the use of two TPES, SEBS and COCe, as cladding materials for elastic fibers. Similar to non-elastic claddings, they enable various cross-sectional shapes and are compatible with a variety of active materials. In particular, their combined use in a core-cladding structure yields a high elasticity optical fiber, which is a promising candidate for neural implants for optogenetics.

TPEs are still pretty new in fiber drawing and several topics could benefit from further development. For instance, future studies could involve:

- Expansion of the range of drawable elastomers beyond SEBS and COCe. In particular, Thermoplastic Polyurethanes are being actively researched and used in processes such as extrusion. They exhibit a wide range of mechanical and optical properties, which could open new doors in thermally drawn fibers.

- Leverage of the control of fibers mechanical properties, through drawing stress, for structural applications. The mechanical properties of a fiber impact directly those of a fabric. One could imagine drawing a fiber with a gradient in Young's Modulus along its length. This would yield a gradient in the fabric mechanical properties, which is of particular use for structural applications such as textile-reinforced composites, or textile exoskeletons.

- Control of fibers optical properties through thermal drawing. By modifying chains alignment, one could impact the optical scattering and birefringence of the fibers.

# Chapter 3

# Elastic electrodes for textile applications

## 3.1 Motivation

Electrical conductors are ubiquitous in devices and they are necessary for almost any application. They serve as power lines, antennas, to transport data... sometimes the conductor is the device itself such as in resistive heating or sensing [42, 43], or capacitive sensing [44]. The context of functional fabrics imposes substantial constraints on the choice and fabrication of electrodes in fibers.

#### High conductivity

Textile fibers range from tens to hundreds of meters in length (a simple knitted sock can require around 400m of yarn). It means that the chosen conductive material has to be processed on a large scale, and be able to carry electric signal over such distances with minimal loss. In addition, the fiber form sets limits on the cross-sectional dimensions of the device. Most often, an electrode is only one component among many, and devices require multiple electrodes. The cross-section of the conductor needs to be small enough, that the whole structure fits into a single fiber. In our work, we aim for fibers whose cross-section remains below 1mm, to be able to inte-

grate them seamlessly into fabrics along with medium size yarn. The combination of large length and narrow cross-section requires the material of choice to have a very high conductivity, to ensure proper transmission of current and avoid excessive Joule heating. Hence we aim for metal conductivity, which is on the order of $10^7$S/m.

**Mechanical properties**

As explained in section 1.1.2, a fiber undergoes numerous mechanical constraints, both during fabrication and usage of a fabric. As a result, the electrodes have to sustain these deformations without loss of functionality or even decrease in performance. Overall the electro-mechanical requirements for in-fiber conductors are:

- High elasticity: no change in conductivity over the range of elongations applied to the fiber, in particular the large strains imposed by processes such as knitting.
- Long cycling life: no change in conductivity over the lifetime of the fabric, within the range of elongations associated with daily use (usually $\leq$15%). In this work we evaluate cycling life by requiring 10 000 cycles between 10% and 15% of elongation (which correspond to roughly 10 cycles a day for 3 years).
- Low Young's Modulus and low bending stiffness.

In addition, one notes that the conductive material needs to be properly encapsulated in the fiber structure, so that the final fabric can be washed without risk of degradation or shorting of the electrodes.

Electrodes with high elasticity and high conductivity appear as an essential building block for functional textile fibers. In section 3.2, we review the different approaches that exist to make such electrodes and in section 3.3 we evaluate the compatibility of these different methods with thermal drawing.

## 3.2 Elastic electrodes

Multiple approaches have emerged to address the challenge of combining elasticity and conductivity, especially in 3-dimensional or planar configurations. We classify theses

approaches in two main types depending on the strategy used to yield elasticity: material based and structure based approaches.

### 3.2.1 Material elasticity

Material based approaches rely on engineering the material itself to be an electrical conductor and have a low Young's modulus and large reversible strain at the same time. These materials are also referred to as intrinsically stretchable conductors [45]. They can be divided between three main classes of materials.

#### Conductive polymers

Conductive polymers are organic polymers that can conduct electricity thanks to conjugated bonds. Their structures usually consists of alternating single and double bonds along the polymer backbone or aromatic rings. Common ones include polyacetylene, polypyrrole, polyaniline and PEDOT:PSS [46]. PEDOT:PSS is by far the most widely used due to its transparency in the visible range and high conductivity, especially with the addition of dopant ($10^4 - 10^5$S/m) [46, 47]. In addition to being easily processable in aqueous solution, PEDOT:PSS provides a good flexibility. However, it fails at strains below 10% and has a Young's Modulus in the order of gigapascals. Many studies have attempted to improve its mechanical properties through blending it with soft polymers or plasticizing it. Although these solutions allow to reach up to 200% strain without failure, they entail an important loss in conductivity compared to the doped polymer ($10^3 - 10^4$S/m) [45, 47, 48].

#### Polymer nanocomposites

Stretchable and conductive polymer nanocomposites consist of an elastomeric matrix containing a conductive filler. Many reviews exist on this widely studied topic, either in the general field of stretchable electronics [45] or focusing on a more specific range of applications such as healthcare [49, 50]. PDMS, a thermoset silicone, is the most common matrix material. Thermoplastic options include TPUs and SEBS. Hydrogels

are also explored, especially when a lower Young's Modulus is needed. Fillers come in different form factors (nanoparticles, nanowires, nanoflakes) and are either metals (Silver, Gold) or carbon compounds (carbon nanotubes, graphene...). The concentration of filler needs to be above the percolation threshold, so that the particles create continuous conductive pathways along the whole material. These composites are very easy to process and yield high elasticity ($> 100\%$). Conductivity ranges between $10^3$ and $10^5$S/m, and increases with the concentration of filler. However, increasing the filler concentration quickly increases the Young's Modulus of the composite [51]. In addition, the conductivity in the direction of elongation tends to decrease strongly under strain, as the distance between particles increases [49].

#### Liquid metals

Gallium and liquid-metal alloys based on gallium (e.g. eutectic gallium-indium: EGaIn), that are liquid at room temperature, are widely used to create stretchable interconnects [52]. Although a liquid metal is not elastic by itself (it is a viscous fluid), it can easily be encapsulated within elastomers such as PDMS [53] or SEBS [54], or used as a liquid filler within a porous elastomeric scaffold [55]. The resulting electrodes demonstrate very high elasticity ($> 1000\%$) and conductivity ($10^6$S/m). One should note that, if upon elongation the cross-sectional area of a channel containing liquid metal decreases significantly, then its resistivity will increase similarly. Additionally, gallium-based alloys develop an oxide layer on their surface, which can lead to a decrease of conductivity with cyclic loading.

### 3.2.2 Structural elasticity

#### Principle

Structure-based approaches to create elastic conductors exploit bending deformation to generate large elongation of a structure while maintaining minimal strain in the material itself. If we consider a beam undergoing pure bending (see figure 3-1a), the

axial strain at a given point in the beam is:

$$\varepsilon = \frac{y}{\rho} \tag{3.1}$$

where $y$ is the distance between this point and the neutral axis of the beam, and $\rho$ is the radius of curvature. The maximum strain inside the beam will then be given by the radius of the beam divided by the radius of curvature, so by making thinner structures, one can maintain low levels of material strain during bending.

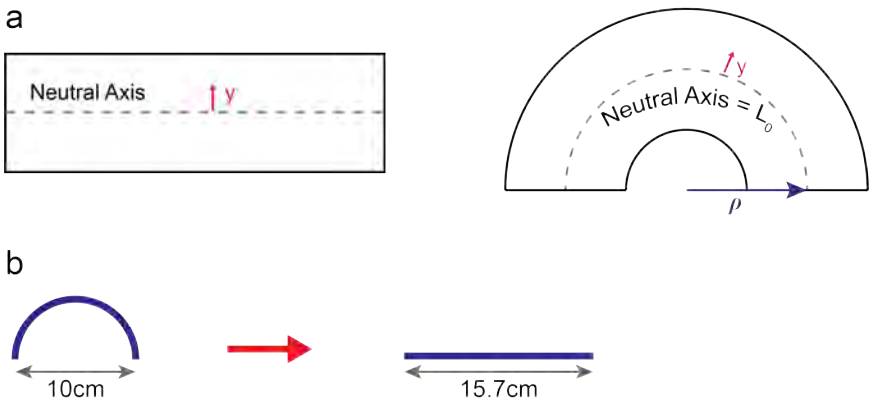


Figure 3-1: Bending and structural elasticity (**a**) Beam under pure bending. (**b**) Example of structural elasticity: the arc length of the wire remains constant, while the structure elongates from 10cm to 15.7 cm.

Let us illustrate the use of bending to provide structure-based elasticity with a very simple example (Figure 3-1b). We consider a 10$\mu$m diameter wire that forms a half circle of radius 0.5cm. This structure is 1cm long. When the wire is fully straightened, it is about 1.57cm long. If we calculate the bending strain inside the wire we find that, while elongating the structure by 57%, we have generated at most 0.2% of local strain in the material.

### Applications

By creating thin and highly curved metallic traces, one can leverage structure-based elasticity to build conductive pathways that exhibit metal conductivity ($10^7$S/m) and sustain large deformations. This concept has been extensively explored in the rich literature around stretchable electronics [56, 57]. Metal conductors in shape of

serpentines or horseshoes [58, 59, 60], helices [61, 62, 63], or wrinkled films [64, 65, 66] are attached to, or embedded in an elastomeric matrix. Upon stretching, the metal deforms in bending mode, allowing for tens of percent of reversible strain without impairing its conductivity. This powerful approach yields noticeable results. For example, Pan et al. report serpentine interconnects on a 7$\mu$m Ecoflex substrate that sustain 25000 cycles of 120% elongation without the formation of microcracks. Numerous studies explore the relationship between the geometry and the mechanical properties of these conductors, analyzing the effects of shape, trace thickness, polymer encapsulation... [58, 67, 68] Generally, the metal trace is either directly patterned on the host polymer into their final shape or they are patterned onto a pre-stretched elastomer and forced to buckle into a given shape upon relaxation [61, 68]. In both cases though, the process relies on photolithography so the size of the final device is limited to the size of a silicon wafer.

## 3.3 Electrodes and thermal drawing

As a basic requirement for most devices, conductive materials have long been thermally drawn into functional fibers. Four types of materials are found: solders, polymer composites, solid metal wires and liquid metals. In this section we detail the use of these materials in thermal drawing and the possibility to use them in elastic fibers.

### 3.3.1 Traditional electrodes

#### Solders

Solders refer to metals and metal alloys that have a low melting point (usually $<$ 200°C). Tin [20], Bismuth Tin [69] or Indium [26] are examples of solders that have been widely used in thermally drawn fibers. In the preform, the solder is encapsulated within a channel between other materials. During the draw, it melts and flows, and the shape of the electrode is maintained by the stress in the materials surrounding it. Drawing solders is challenging though, for two main reasons. First, the metal is more

dense than the polymers surrounding it. Hence it tends to fall to the bottom section of the fiber, creating a bulge and leaving the top part of the channel empty. Second, as a viscous fluid, it is susceptible to capillary instability. High temperature and small channel size are favorable to capillary break up, which results in small metal spheres in the final fiber. This phenomenon can be attained on purpose for some applications [70], but in general in precludes the fabrication of long and thin solder electrodes.

### Polymer composites

Carbon-loaded thermoplastic polymers, similar to the composites described in section 3.2.1, are a versatile, easy to process, type of drawable conductive materials. They permit to build electrodes with custom geometries, in particular thin conductive sheets which cannot be obtained with solders. This makes them widely used as charge collectors, for example in capacitive or piezoelectric fibers [71, 23]. Conductive Polycarbonate (CPC) and conductive Polyethylene (CPE) are the two composites regularly used in thermally drawn fibers. If they constitute good options for electronic transport across the cross section of a fiber, their conductivity after drawing (1-10S/m) is too low to properly conduct electricity along very long fibers. Hence they are usually used in concert with metal electrodes, which delivers excellent conductivity across two length scales: the microscale of the cross section and the meter scale of the fiber length.

### Metal wires

Rein et al. [24] demonstrated thermal drawing of a solid metal wire for the first time in 2018, in a process called convergence. In this process the preform is designed with a hollow channel and, during the draw, a solid metal wire is fed through that channel. The size of the channel is calculated so that, after cross-sectional reduction, its diameter is equal to, or slightly smaller than the diameter of the wire. Hence after the necking zone, the cladding material clamps onto the wire and pulls it, providing the driver for wire feeding. This powerful technique has since been used extensively due to its reliable results, ease of implementation and versatility. Indeed, any material

that comes in a wire form factor and remains solid at draw temperature can be drawn using convergence including metals, semiconductors, carbon nanotube yarns, or even functional fibers, in a fiber mise en abyme [72].

#### Liquid metals

By filling a channel in the preform with liquid metal and drawing at a high enough stress to enforce a good maintain of the cross section, Gallium, Gallium-Indium and Gallium-Indium-Tin liquid electrodes have been created in fibers [30, 73]. They demonstrate high conductivity ($10^6$S/m) and promising mechanical properties. Because they are only used in the context of elastic fibers, we will discuss their performances more in the next section.

### 3.3.2 Which materials for in-fiber elastic electrodes?

As discussed in section 3.1, in-fiber electrodes for textile applications should show a combination of high conductivity, high elasticity and low Young's Modulus. Obviously, one can see from section 3.2 that there is no perfect material. Here is the rationale that guided our approach to solving this problem.

Conductive polymers and elastomer nanocomposites have low conductivities. Furthermore, conductive polymers such as PEDOT:PSS are thermoset, which put them out of the question. Composites are appealing due to their ease of processing. Still, in addition to their relatively low bulk conductivity, one has to take into account the level of elongation that occurs during the draw and can result in added loss of conductivity. Zhang et al. demonstrated thermally drawn stretchable electrodes made with SEBS loaded with carbon black [74]. In their work, they leverage the change in resistance of the electrodes upon fiber elongation to make a resistive strain sensor. As our goal is to make electrodes whose resistance will remain constant upon elastic deformation, we focus on different approaches.

Liquid metals are very promising, yielding very soft fibers, with low Young's Modulus (no increase in modulus compared to a pure elastomer fiber) and hundreds of

percent of elasticity [30, 73], but they present practical challenges. Establishing electrical contacts, either with a device within a fiber or with a circuit at the tip of the fiber, is a very tedious process. There is an important risk of leakage, especially at these points, which in practice leads to short-circuits. Leakage could also have dramatic consequences in applications such as medical implants. In addition, changes in the channel size due to fiber stretching or lateral pressure results in changes in resistance [73].

Solders were ruled out due to the complexity to draw them and their lower conductivity compared to metals that can be drawn using convergence. Consequently, we decided to focus our study on solid wires, and to leverage structural elasticity within fibers to combine high elasticity with the conductivity of metals such as copper, silver and tungsten.

Notwithstanding, in the framework of a one-dimensional fiber device, the use of structural elasticity is paradoxical: large-scale fiber making processes (extrusion, melt-spinning, thermal drawing, etc.), are invariably associated with high elongation and alignment in the axial direction of the fiber. A solid metal wire would inevitably emerge straight from the draw process due to the extensional flow. This leads to an extension-curve paradox, as the high extension needed to make the fiber precludes curved shapes in the final product.

In the next two chapters, we lift this limitation and explore two approaches to build meandering and helical metal electrodes in thermally drawn fibers. In chapter 4, we mechanically decouple the metal wire and the elastomeric cladding during convergence to enable in-fiber buckling. In chapter 5 we use axial twisting of the fiber to create a helical pathway for the metal while keeping the whole fiber straight.

# Chapter 4

# In-fiber buckled electrodes

## 4.1 Fiber fabrication

### 4.1.1 Principle

This approach harnesses a buckling instability induced post draw to create a wavy path for a metal wire, that is contained in a hollow channel internal to the elastomer fiber. The preform is made of COCe or SEBS and has a rectangular cross section and a hollow rectangular channel with a 5 to 1 ratio. The fiber is drawn while feeding a free-standing copper wire with a diameter of 50 $\mu$m into the preform's thin rectangular channel, using the convergence method. However, instead of making the channel small enough that it collapses on the wire, we design it to be, in the final fiber, a thin rectangular channel in which the wire freestanding ( Figure 4-1a).

In such a fiber, if the cladding is stretched around the wire and subsequently relaxed, the compressive load on the electrode due to the relaxation of the elastic strain in the cladding will force the electrode to buckle inside the channel. One should notice that the boundary conditions at the ends of the fibers need to be different during stretching and relaxation. During the elongation of the cladding, the wire needs to be able to slide with respect to the polymer. On the contrary, during the cladding relaxation, it is important that the ends of the wire and of the cladding be clamped together, so that the compressive load is fully transferred from the elastomer

to the metal. This process can be done on a large scale using multiple sets of rollers as depicted in figure 4-1a (details in section 4.1.2), or manually / in an tensile tester for shorter length of fibers (details in section 4.2.1).

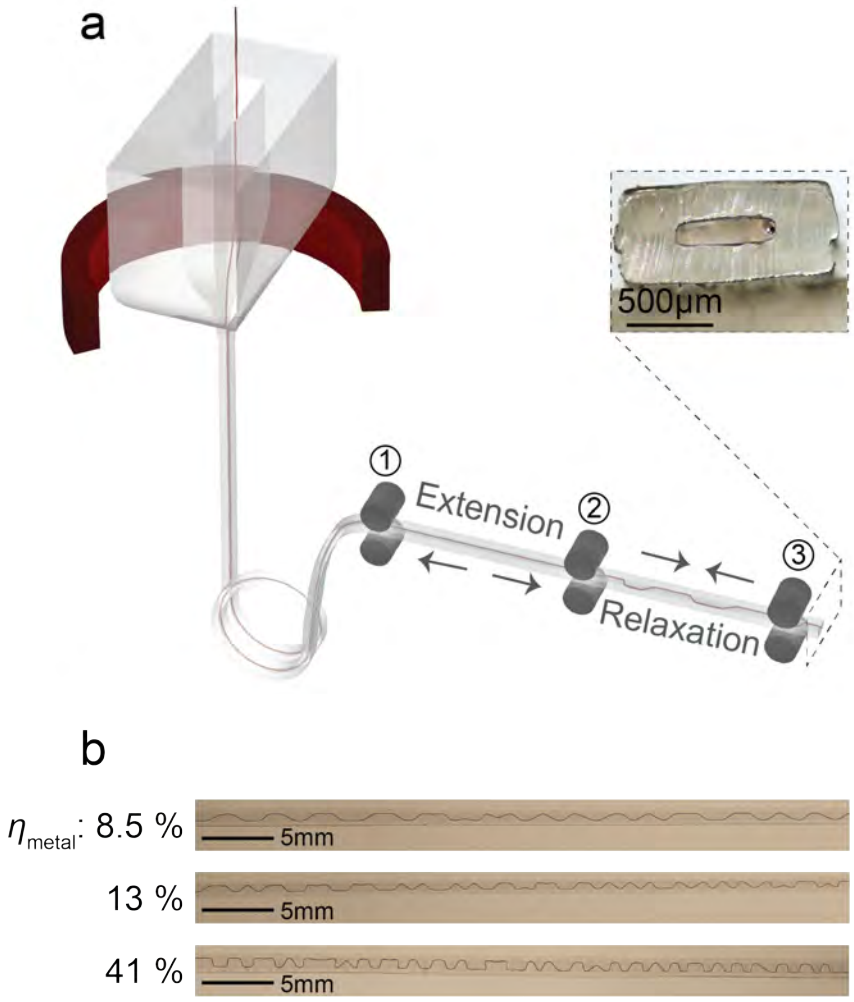


Figure 4-1: (**a**) Fabrication of the buckled electrodes. Inset: a cross-section of the COCe fiber containing a 50$\mu$m copper wire within an open slot. (**b**) Different COCe fibers with buckled copper electrodes.

This method leads to a metal trace length, $L_{metal}$, that is longer than the fiber length, $L_f$, yielding an excess metal length of,

$$\eta_{metal} = \frac{L_{metal} - L_f}{L_f} \tag{4.1}$$

Figure 4-1b illustrates the buckled electrode shapes for different $\eta_{metal}$, which

were measured optically by calculating the electrode arc length in COCe fibers. As desired, our technique produces meandering electrodes in thermally drawn fibers, and the number and curvature of each buckle varies with $\eta_{metal}$. More than 50 meters of continuous fiber with buckled electrodes were produced, and $\eta_{metal}$ up to 95% was achieved. Some buckling could be achieved directly during the draw, without post-processing. This point is discussed in appendix A. Because it would only yield small values of $\eta_{metal}$, we focus on post-draw buckling.

### 4.1.2 Large scale apparatus

Buckling can be induced continuously in lengths of fiber by using three sets of rollers as depicted in figure 4-2. Roller 1 has a speed V1 and holds the cladding of the fiber without preventing the wire from slipping inside the channel. In practice, this is achieved by making the surface of the roller sticky, covering it with double-sided tape. When the buckling is performed in the continuity of the draw, this roller is also responsible for drawing the preform into a fiber (Figure 4-2a). Roller 2 rotates at a speed V2 higher than V1 and pulls together the cladding and the wire. The cladding is stretched by a ratio of V2/V1 while additional length of wire is pulled into the cladding through Roller 1. Roller 3 rotates at V1, allowing the cladding to relax back to its original length. As the electrode is pinched with the cladding by Roller 2 and 3, the relaxation creates a compression force on the wire, leading it to buckle. When the buckling is done in the continuity of the draw, the wire is pulled in from the top of the draw, and arbitrarily long fibers can be made. A similar buckling setup can also be applied to batches of pre-drawn fiber, which we demonstrate in figure 4-2b. Long sections of fibers are fed through the rollers and the wire is pulled from the end section of the fiber. The section of the fiber that has no wire left is then cut off.

With this method, we were able to induce buckling in 20m of a COCe fiber containing a 50$\mu$m copper wire. In this set up, the speed parameters used are: V1= 1.58m/min and V2= 1.71m/min. Rollers are commonly used in textile processing and offer scalability as well as throughput.

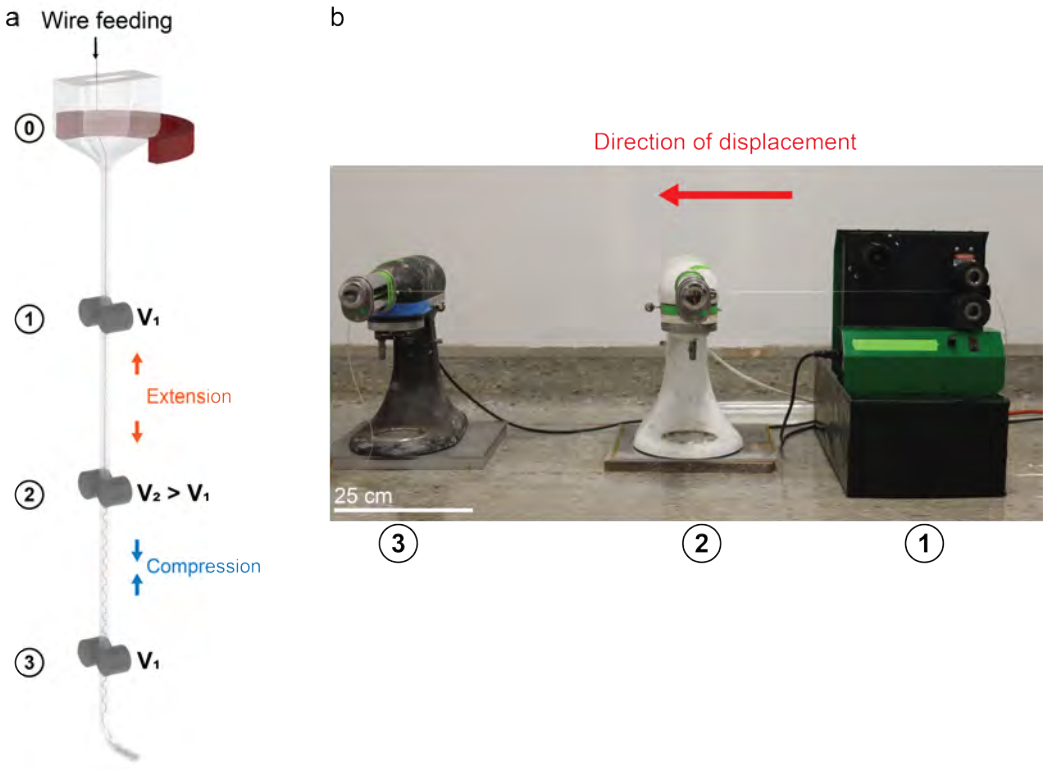


Figure 4-2: (**a**) Design of a continuous buckling set up in the continuity of the draw. 0: Fiber drawing furnace. 1: Roller 1, at speed V1. The roller allows for the wire to slide inside the channel. 2: Roller 2, speed V2. The roller clamps the cladding and the wire together. 3: Roller 3, speed V1. The roller clamps the cladding and the wire together. (**b**) Continuous buckling apparatus separate from the draw (Same legend as (a)).

## 4.2 General electro-mechanical behavior

### 4.2.1 Controlled buckling set up

Although the buckled shape can be created directly in line with the draw process (section 4.1.2), for the purpose of this mechanistic study, we decouple the buckling process from the draw. COCe fibers are first produced with linear electrodes free-standing in thin rectangular channels, and then the electrodes are buckled in a tensile tester to measure force and displacement as depicted in Figure 4-3.

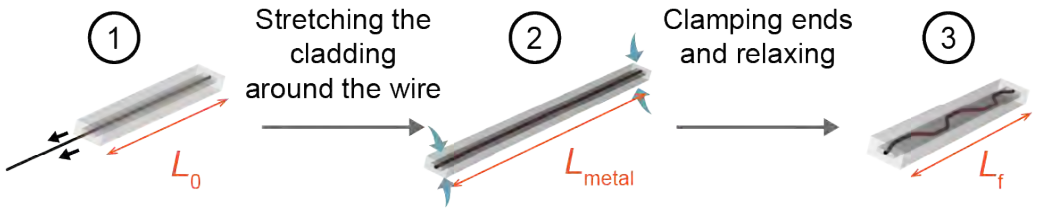


Figure 4-3: Buckling of the electrode outside of the draw process

The cladding with an initial length $L_0$, is stretched around an additional length of electrode to a length $L_{metal}$, yielding a cladding strain:

$$\varepsilon_{clad} = \frac{L_{metal} - L_0}{L_0} \tag{4.2}$$

The ends of the cladding and the wire are then clamped together, and the system is brought back to zero load under controlled speed and displacement.

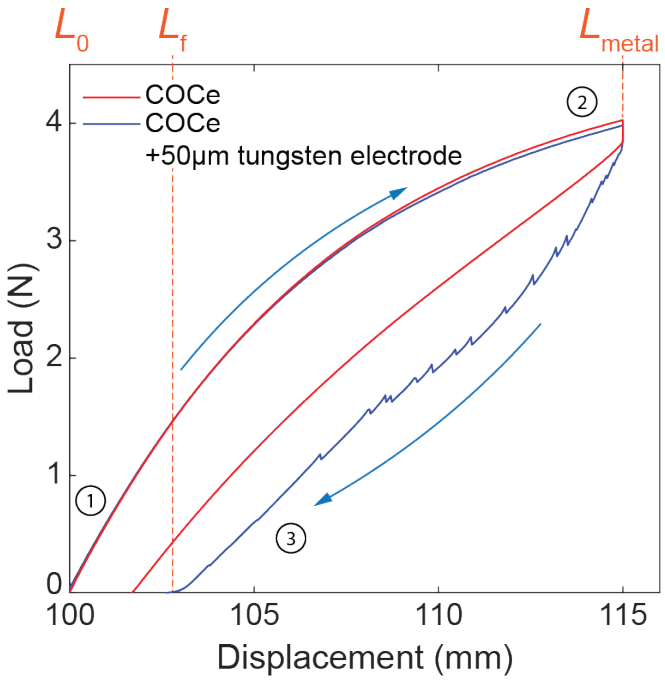


Figure 4-4: Load and displacement during the buckling process. Comparison with and without electrode for the same fiber cross-section. The significant lengths of the fiber are marked.

Figure 4-4 displays the force and displacement measured during this buckling cycle for a 10cm COCe fiber, with or without a 50$\mu$m tungsten electrode. The final length of the fiber, $L_f$, is longer than $L_0$, leading to the excess length of metal in the final

structure $\eta_{metal}$, as defined by equation 4.1, which is lower than $\varepsilon_{clad}$. This is, in part, due to the incomplete recovery of the polymer itself, as observed for COCe in the absence of an electrode (figure 4-4). Additionally, during the relaxation stage (3), the compression and buckling of the electrode gives rise to a reaction force that opposes the recovery force in the polymer. The equilibrium between the recovery force of the elastomer and the buckling forces determine the final length of the fiber, leading to $L_f$ larger than $L_0$.

From there we understand that the recovery force of the elastomer plays a key role in determining $\eta_{metal}$. For a given elastomer, this force increases with the cross-sectional area of the cladding and with the pre-strain of the cladding $\varepsilon_{clad}$. We find experimentally that, for a given fiber geometry, $\eta_{metal}$ depends linearly on $\varepsilon_{clad}$ up to 50% strain in COCe (Figure 4-5).

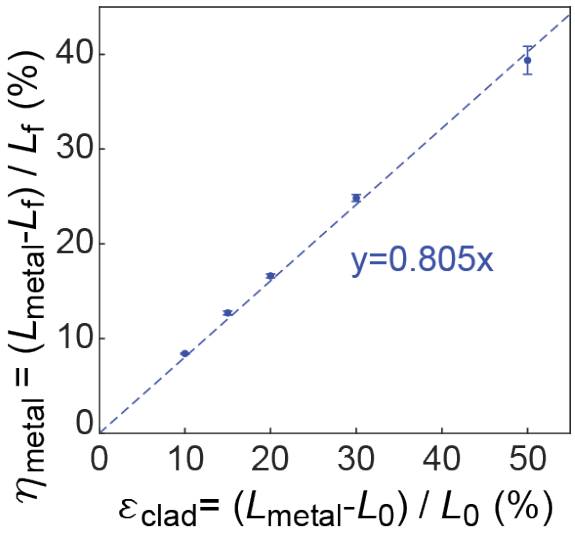


Figure 4-5: $\eta_{metal}$ depending on the strain of the cladding ($\varepsilon_{clad}$), for a given geometry. COCe - 25$\mu$m tungsten (n=5).

### 4.2.2 Tensile properties

A simple tensile test of fibers with a buckled electrode brings valuable mechanistic information. The stress-strain curve demonstrates a J-shaped behavior [57] (Figure 4-6a): the electrode is at first "mechanically invisible" and the fiber exhibits the same tensile properties as a pure elastomer fiber. After the metallic buckles have unfolded

in the channel, an inflection point is visible on the curve and the stress increases drastically. Here, the tensile properties of the metal dominate and we can see the yield and plastic deformation of the electrode, until it breaks. In figure 4-6b, the stress-strain curves for three COCe-copper electrode fibers, that have different cross-sections and $\eta_{metal}$, confirm that $\eta_{metal}$ controls the point where the curve diverges from the behavior of the cladding material. At $\eta_{metal}$, the wavy electrode becomes straight and the metal switches from bending to tensile deformation. Hence, $\eta_{metal}$ defines the extent of elasticity in these fibers.

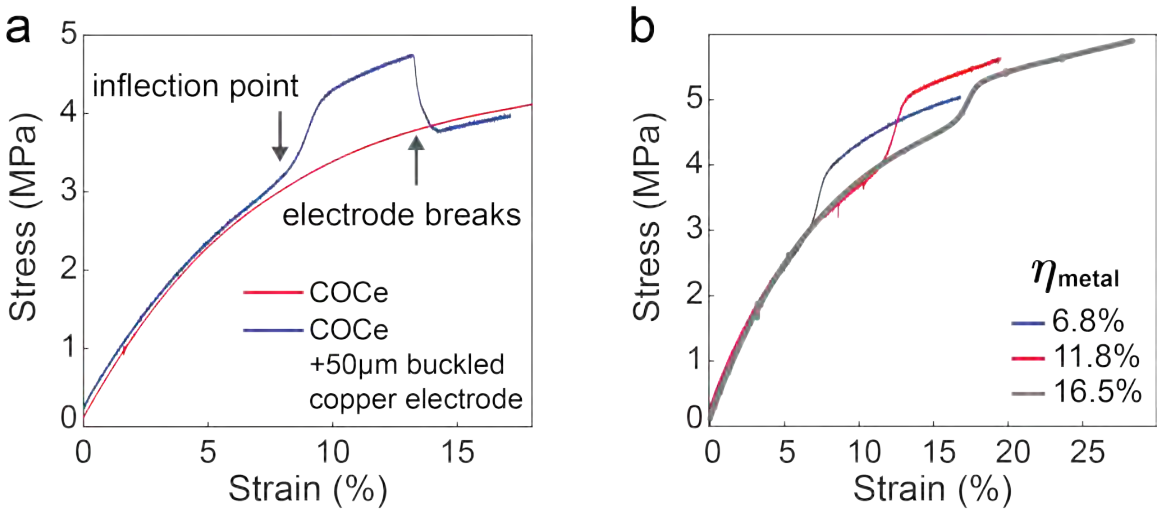


Figure 4-6: (**a**) Stress-strain curve of a COCe fiber with (blue) and without (red) a buckled copper electrode ($\eta_{metal}$ = 7.9%). (**b**) Tensile test of three fibers. COCe - 50$\mu$m copper - various cross-sections and various $\eta_{metal}$.

The tensile behavior of the fibers then depends on the cladding material and $\eta_{metal}$. The properties in the elastic range are identical to the cladding ones, especially the Young's Modulus of the fiber, and $\eta_{metal}$ determines the limit of elastic deformation.

### 4.2.3 Electrical properties

Through mechanical characterization, we identified the point where the electrodes undergo severe plastic deformation. We are now interested in studying the conductivity of the electrodes in the range of elastic deformation of the fibers.

At rest, the fibers containing buckled copper electrodes exhibit an average resis-

tivity of $1.87 \cdot 10^{-8} \pm 0.39 \cdot 10^{-8}$ Ω.m (n=7), which increases slightly with $\eta_{metal}$, due to the increased trace length of the electrode.

We applied tensile elongation on the fibers while simultaneously recording the tensile load and the resistance of the electrode. We found that the resistance increases when the tensile strain reaches $\eta_{metal}$, upon the change in the deformation mode, from bending to tensile deformation (Figure 4-7a). Prior to this transition, the resistance varies by less than 0.1%.

To confirm this observation, we applied strain cycles of increasing amplitude to the fibers and measure the resistance between the cycles (Figure 4-7b). No hysteresis was observed below $\eta_{metal}$, which confirms that $\eta_{metal}$ marks the yield point of the electrode, hence the yield point of the fiber.

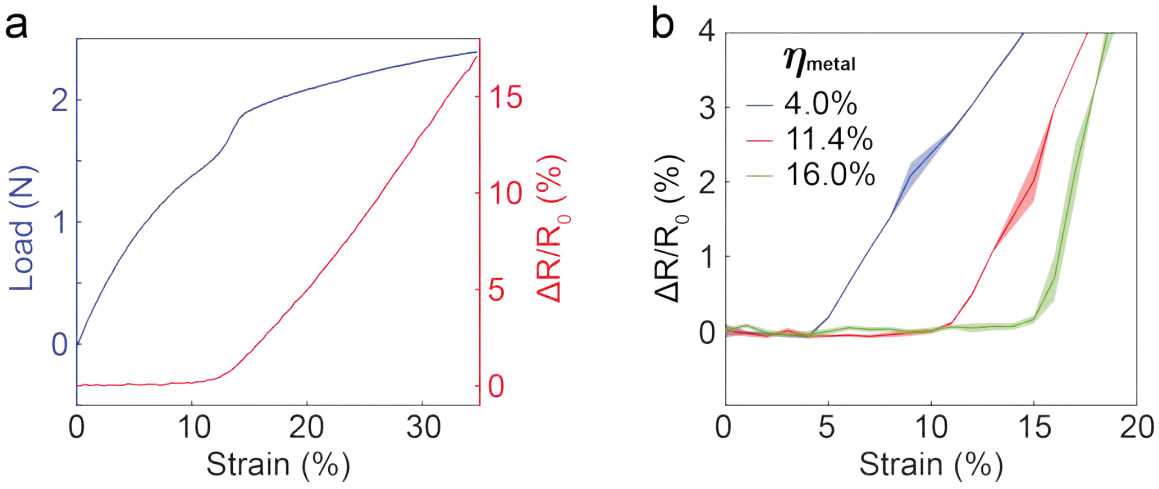


Figure 4-7: (**a**) Simultaneous measurement of force and change in resistance during tensile deformation of a COCe fiber with a 50 $\mu$m buckled copper electrode ($\eta_{metal}$ = 12.9%). (**b**) Change in resistance of the electrode after stretching cycles of increasing amplitude. COCe fiber with a 50 $\mu$m buckled copper electrode. The amplitude of the cycles is increased by 1% steps.

Our high level characterization shows that we managed to fabricate in-fiber electrodes that exhibit constant, high conductivity over a wide range of elastic deformation. As $\eta_{metal}$ dictates the limit of elasticity, we now want to understand more precisely how different material and geometric parameters influence its value. In section 4.2.1, we enlightened the effect of the recovery force, and more particularly of $\varepsilon_{clad}$, in the

final equilibrium that controls $\eta_{metal}$. In the next section, we present an analytical mechanical model designed to capture how different parameters alter the load required to buckle the wire.

## 4.3 Constrained buckling model

### 4.3.1 Identification of constrained buckling

In figure 4-4, during the relaxation of the fiber with an electrode, jumps in force correspond to the formation of new buckles. These are characteristic of the planar buckling of a beam with lateral constraints [75, 76, 77]. These jumps in force are more pronounced in fibers containing higher modulus tungsten electrodes, but are also observed in copper electrodes (see figure 4-8).

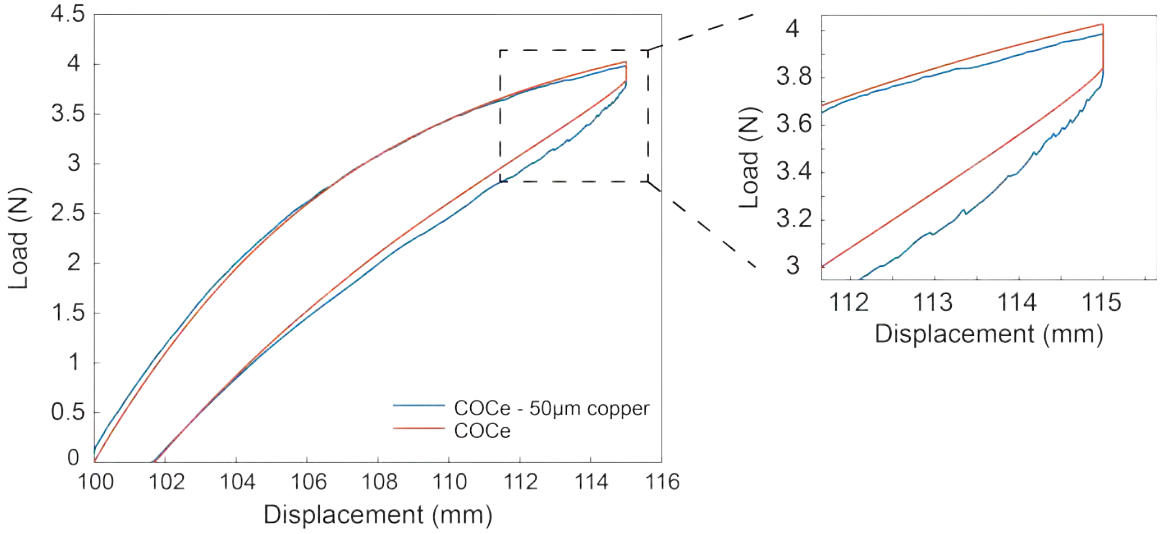


Figure 4-8: Load and displacement during the buckling process. Comparison of COCe fibers with (blue) and without (red) a 50$\mu$m copper electrode of the same cross-section. With copper electrodes, the jumps in force in the relaxation stage are still visible but much smaller.

So, for thin enough channels (thickness $<$ 4$\times$wire diameter), we analyze the relaxation and buckling stage as a planar, constrained buckling problem. High-speed videos support this choice by revealing essential mechanistic information. Captions of the videos are shown in figure 4-9. First, the buckles form in successive steps, as

described extensively in literature around constrained buckling [75, 76, 77, 78]. Upon increasing compressive strain, a straight wire buckles into the first mode. The buckle grows, touches the opposite wall and creates a contact point. A contact zone then develops as the load increases, until the axial load and the length of the line contact meet the buckling criterion for a clamped bar. A new bifurcation point is reached and the contact zone snaps into a new buckle.

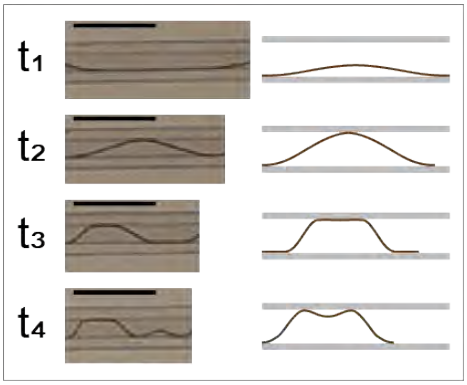


Figure 4-9: Step-by-step buckling: section of a fiber at different stages of the buckling process. Cations from high speed video. COCe - 50$\mu$m copper (scale bars: 2mm). The step-by-step buckling is compared to the theoretical shape on the right.

Second, the videos show the non-unicity of solution to the constrained buckling problem. For a given compressive strain and geometry, the exact shape and load that develop cannot be predicted due to degenerate energy states (non-unique solutions), mechanical imperfections, and surface interactions between the wire and the walls [75, 79, 80]. Although due to this indeterminacy, the exact shape of the metal wire cannot be quantitatively predicted, literature shows that it is still possible to bound the range of solutions when neglecting friction. A qualitative analysis is then possible.

We use an adapt an analytical model developed by Chai [75] to study the effect of the bending stiffness of the wire, width of the channel, and length of the fiber on $\eta_{metal}$. Chai's analysis considers the classic step-by-step buckling scenario.

### 4.3.2 Assumptions of the model

The main hypotheses of the model are:

- Nonlinear geometric deformation (large deformation)
- Linear material's deformation (hookean elasticity)
- Quasi-static analysis
- Clamped extremities of the wire
- Planar displacement of the wire
- No friction between the wire and the walls
- Lateral walls are rigid and fixed
- No plastic deformation of the wire

Although the last three hypotheses do not match with our system, they appear as reasonable simplifications to gain qualitative insights, for the following reasons:

1. Given that the wire and the cladding are clamped together at the end of the fiber, we use as a first approximation that the friction forces are negligible compared to the axial force applied to the wire.
2. Although the walls are made of a soft polymer, we did not observe a significant deformation of the walls upon buckling. We consider the COCe cladding as rigid walls. SEBS has a much lower Young's Modulus than COCe and the effect on buckling is mentioned briefly in section 4.4.4.
3. In practice, even for relatively small compression strains (5%), the wire starts buckling plastically, due to plastic bending. One possible way to account for plastic deformation is to use the tangent modulus theory. The system would be the same but the modulus of the wire would start decreasing as buckling goes on. Because we chose not to consider plastic deformation, our model cannot quantitatively predict the behavior of the electrode. However, we find that it stills captures qualitative features of our system and gives good insights on the influence of the different parameters. In section 4.3.5, we show the match of our model with experimental results for the load applied to the wire.

### 4.3.3 Derivation

The large deformation analysis presented by Chai defines three geometric variables for one buckle (figure 4-10): $c$ is the length of the line contact, $L$ is the arc length

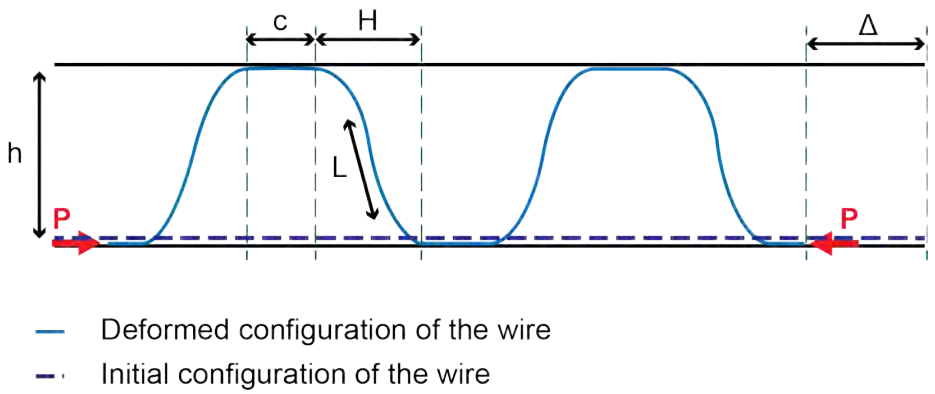


Figure 4-10: Definition of the variables $c$, $H$, $L$, $h$, $P$ and $\Delta$ for the analytical model

of the bent portion of the wire, and $H$ is the projected length of the bent portion of the wire. The other unknown variables in our case are the number of buckles $n$, and the axial force $P$ applied at the ends of the wire. In our adaptation of the model, we solve for the load $P$ and control for the end displacement $\Delta$, which is the opposite of what is done by Chai. The known parameters are the distance $h$ between the walls, the total length of the wire $L_{metal}$, the Young's Modulus of the wire $E$, and the area moment of inertia of the wire $I = \pi \cdot r^4/4$, with $r$ the radius of the wire.

In the large deformation analysis, we get from mechanical equilibrium:

$$\frac{k \cdot H}{2}(1 + (\frac{h}{H})^2)^{3/4} = 2 \cdot [2 \cdot \mathbf{E}(\frac{\pi}{2}, \frac{\alpha}{2}) - \mathbf{F}(\frac{\pi}{2}, \frac{\alpha}{2})] \tag{4.3}$$

$$\frac{k \cdot L}{2}(1 + (\frac{h}{H})^2)^{1/4} = 2 \cdot \mathbf{F}(\frac{\pi}{2}, \frac{\alpha}{2}) \tag{4.4}$$

where $k = P/(E \cdot I)$, $\alpha = \arctan(h/H)$ and $\mathbf{F}$ and $\mathbf{E}$ are the elliptic integrals of the first and second kind respectively.

Considering the arc length of the wire we can write:

$$2n \cdot (c + L) = L_{metal} \tag{4.5}$$

Finally, taking into account the axial compression of the wire, the end shortening $\Delta$

of the column is given by:

$$\Delta = 2n \cdot (L - H + \frac{cP}{E\pi r^2} + \frac{PH}{E\pi r^2} \cdot (1 + (\frac{h}{H})^2)) \tag{4.6}$$

We now have a system of 4 equations with 5 unknowns: $P$,$H$,$L$,$c$ and $n$. The system can be solved when fixing one variable.

### 4.3.4 Solving algorithm

We use an iterative solving process. Starting at very small $\Delta$, we fix $n = 1$ and solve the system for $P$, $H$,$L$, and $c$. We then look at the stability of our system against buckling.

If $P > \frac{4\pi^2 EI}{c^2}$ , then the straight section is not stable against buckling. We increase $n$ by 1 and solve the system again. We solve iteratively until we reach the value of $n$ for which the straight section of the wire is stable. We can then increase $\Delta$ incrementally and repeat the process. This allows us to determine the shape of the wire and the buckling load for increasing end displacement $\Delta$.

As mentioned in section 4.3.1, constrained buckling entails indeterminacy due to degenerated energy states. For a given number of buckles, the energy of the system does not change if one buckle slides horizontally along the channel without deforming. However, it will change the length of the straight segments that surround it, hence their tendency to buckle and jump toward the $n + 1$ state. We bound the possible range of solutions to this problem by solving it for the two limit cases. The condition $P > \frac{4\pi^2 EI}{c^2}$ , assumes that all of the straight sections have the same length $c$. This is one of the two limit cases, leading to the least number of buckles. The opposite limit case considers that all the buckles are next to each other and there is only one long straight section, which leads to the largest number of buckles. To solve for this case, we replace the equation for buckling stability with $P > \frac{4\pi^2 EI}{(2nc)^2}$. These two extreme configurations are depicted in figure 4-11.

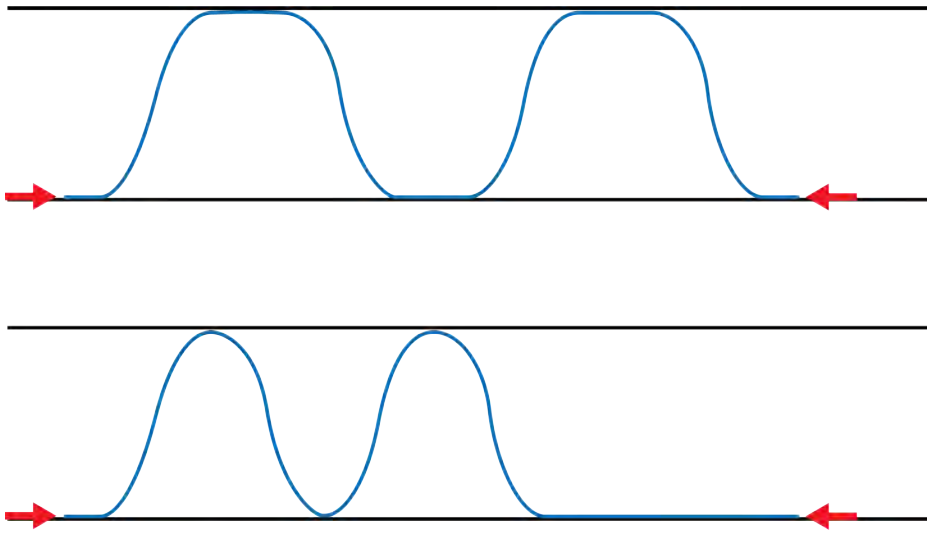

Figure 4-11: Degenerate states for a buckled electrode. The two configurations have the same bending energy. Top: symmetric state, with minimal length for the straight segments leading to a lower number of buckles. Bottom: collapsed state, with all the straight segments combined in one, leading to a higher number of buckles.

### 4.3.5 Quantitative fit

To assess the validity of this model, we calculate the bounding values of the load $P$ applied to the wire for geometric and material parameters that match our experimental data ($r = 25\mu$m, $E = 110$MPa, $h = 560\mu$m). Experimentally, we deduce the value of the load from the difference in the relaxation force between a fiber with an electrode and a fiber without an electrode during a buckling cycle (Figure 4-12). The compressive strain is deduced from the displacement in the relaxation stage. We find that for small strains, our model quantitatively captures the behavior of our system. However, the experimental results depart from the modelled behavior at about 2.5% compression. A collapse of the load indicates plastic deformation of the wire.

Despite its limitations, the model shows a good fit for small deformations, and a good ability to predict the qualitative influence of the different parameters in our system, as shown in the next section.

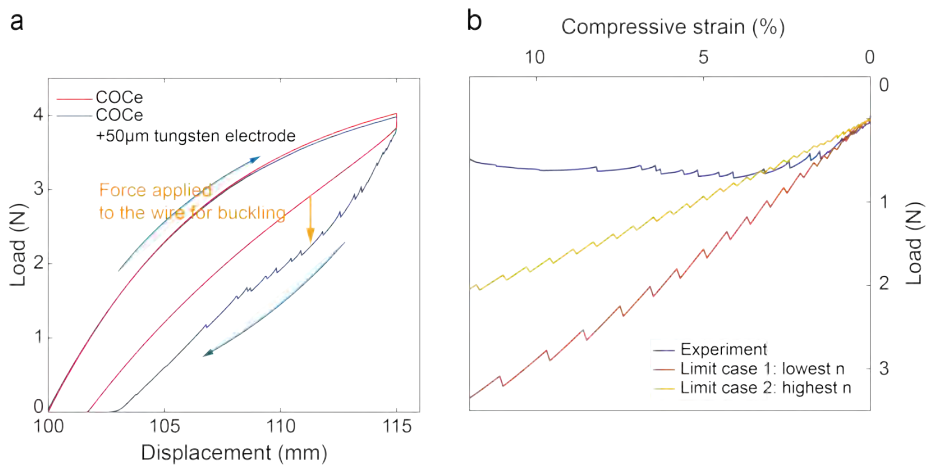


Figure 4-12: Matching of the model with experimental data. (**a**) Load versus displacement measured during a buckling cycle of COCe fibers with and without 50$\mu$m tungsten electrodes. The difference in the load during the relaxation phase is the load effectively used to buckle the wire. (**b**) Load applied to the wire during compression. The orange and yellow curves correspond to the highest and lowest load calculated with the analytical model. The experiment departs from the model around 2.5% of compressive strain due to plastic buckling.

## 4.4 Effect of geometric and material parameters on $\eta_{metal}$

### 4.4.1 Wire bending stiffness

For a given compressive strain, the buckling load calculated using our model depends linearly on the wire bending stiffness (also called flexural rigidity, see figure 4-13a). Therefore, the value of $\eta_{metal}$ should decrease as the metal wire becomes stiffer.

Experimentally, altering the diameter of the wire to change its stiffness would change the effective size of the gap. To compare the effects of the bending stiffness without altering the fiber geometry, we employ 50$\mu$m electrodes of copper (Young's modulus, $E_{Cu}$ =110GPa) and tungsten ($E_W$ =400GPa) in fibers with identical cross-sections. As predicted, figure 4-13b indicates that the tungsten electrode yields a lower $\eta_{metal}$ that depends linearly on $\varepsilon_{clad}$.

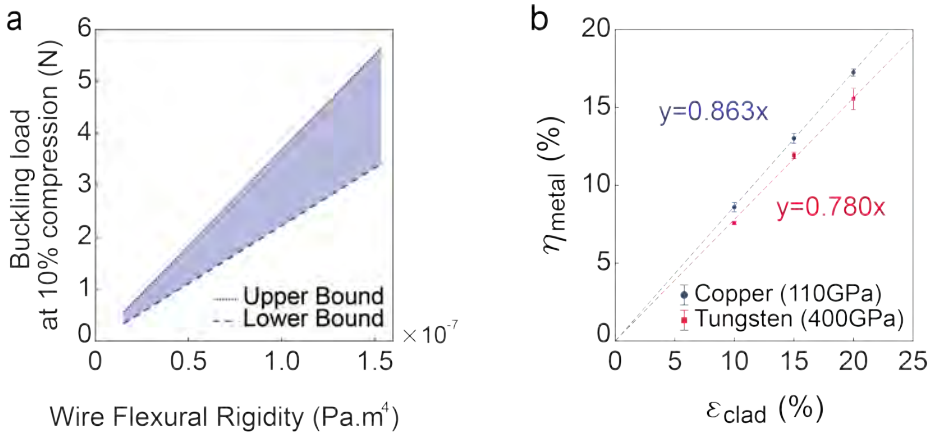


Figure 4-13: Effect of wire bending stiffness (**a**) Calculated effect of the flexural rigidity of the wire on the buckling load for 10% compression. The shaded area indicates the range of solutions. (**b**) Effect of the Young's Modulus of the electrode on $\eta_{metal}$. COCe - 50$\mu$m copper compared to COCe - 50$\mu$m tungsten (n=5).

### 4.4.2 Channel size

Our model predicts that the buckling force depends on the gap size, $h$ following a decreasing power law. Figure 4-14a displays the trend calculated for a 50$\mu$m copper wire at 10% and 20% compression: the gap size will have little influence on $\eta_{metal}$ for large gaps, and a strong impact when the gap becomes small.

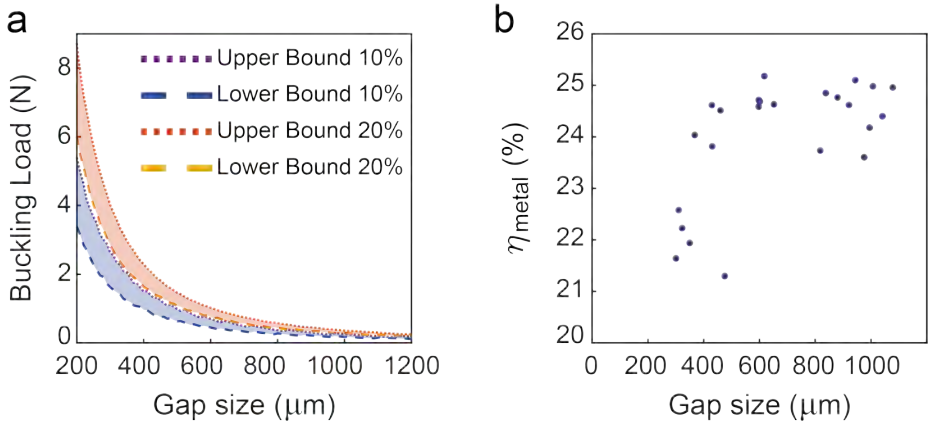


Figure 4-14: Effect of channel size (**a**) Calculated effect of the size of the gap on the buckling load for a 50$\mu$m copper wire at 10% and 20% compression. (**b**) Experimental values of $\eta_{metal}$ depending on the gap size $h$, for a COCe fiber with a 50$\mu$m copper wire; $\varepsilon_{clad}$ =30%

Experimentally, the variation in $\eta_{metal}$ with $h$ is more evident for high $\varepsilon_{clad}$. For $\varepsilon_{clad}$ =30%, we observe a constant $\eta_{metal}$ of 25% for channels larger than 500$\mu$m.

This value then decreases from 25% to 21% for gap sizes decreasing from 500$\mu$m to 300$\mu$m (Figure 4-14b).

Importantly, while the model does predict an increase in buckling load as the channel decreases, it does not fully account for other effects that tend to mitigate the practical consequences on the buckling load such as plastic deformation of the wire. Hence, in figure 4-14b, while significantly reducing channel dimension (by 40%), we observed a rather modest decline in the final elasticity (by 16%). This demonstrates that the scaling of elasticity and channel size is not as onerous as one would think.

### 4.4.3 Fiber length

The model additionally predicts that the total length of the wire does not influence the buckling force, for a given compressive strain, for wires longer than 10 cm (Figure 4-15). This is understandable when one remembers that the buckling load scales as $1/L^2$. Thus the impact of length quickly decreases. Ultimately it means that, for fibers of different length undergoing the same pre-strain $\varepsilon_{clad}$, there is little difference in the load required to buckle the wire. Accordingly, our experiments showed no significant change in $\eta_{metal}$ for different fiber lengths.

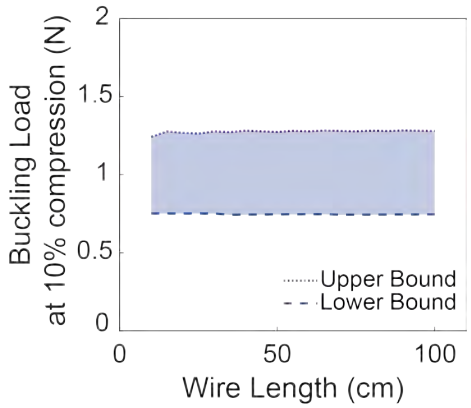


Figure 4-15: Limits of the buckling load calculated for a 50$\mu$m copper wire at 10% compressive strain, depending on the length of the electrode. The variations are negligible for a fiber longer than 10cm.

### 4.4.4 Cladding material

Different cladding materials manifest in different recovery forces, hence different values for $\eta_{metal}$. In figure 4-16 we compare two cladding materials: COCe and SEBS. Although COCe has a higher Young's Modulus, which means a higher recovery force, it also has a much lower recovery strain. Consequently, $\eta_{metal}$ is higher for SEBS fibers. Figure 4-16a shows the recovered strain, $(L_{max} - L_f)/(L_0)$, versus imposed strain. $(L_{max} - L_0)/(L_0)$, after the buckling cycle, for SEBS and COCe fibers with and without an electrode and with a 50$\mu$m electrode. Although the recovery strain of the SEBS fibers is higher in both cases, the difference in recovery strains between the fibers with and without the electrode is also larger for SEBS (difference in the slope of the linear trend). With a lower Young's Modulus, the effect of the wire is more pronounced.

In addition, for $\varepsilon_{clad} > 20\%$, the recovery of the SEBS fiber with an electrode strongly departs from linearity: as the lateral force from the wire onto the cladding increases, the cladding loses its straight configuration and starts to deform laterally during the relaxation stage. This global buckling of the fiber occurs at lower strains for stiffer electrodes and is explored in section 4.6.3. Figure 4-16b shows the deformed shape of a SEBS fiber with a 50$\mu$m tungsten electrode after a buckling cycle with $\varepsilon_{clad} = 10\%$.

Furthermore, Jiao et al. [77] previously showed that, in the case of flexible walls, the formation of a new buckle is delayed, leading to a lower number of buckles with a higher curvature. Figure 4-16c illustrates this by comparing the buckled shape of a copper electrode in COCe and SEBS claddings for the same $\eta_{metal} = 41\%$. In SEBS, fewer buckles appear and they deform as far as looping back on themselves. The stiffer COCe walls promote a larger number of buckles with a lower curvature. the modulus of the cladding material then impacts the curvature of the buckles, which may affect the lifetime of the electrode, as discussed in section 4.5.1.

Additionally, one should be aware that, because the tensile behavior in the elastic range is identical to that of the fiber without electrode, the cladding material directly

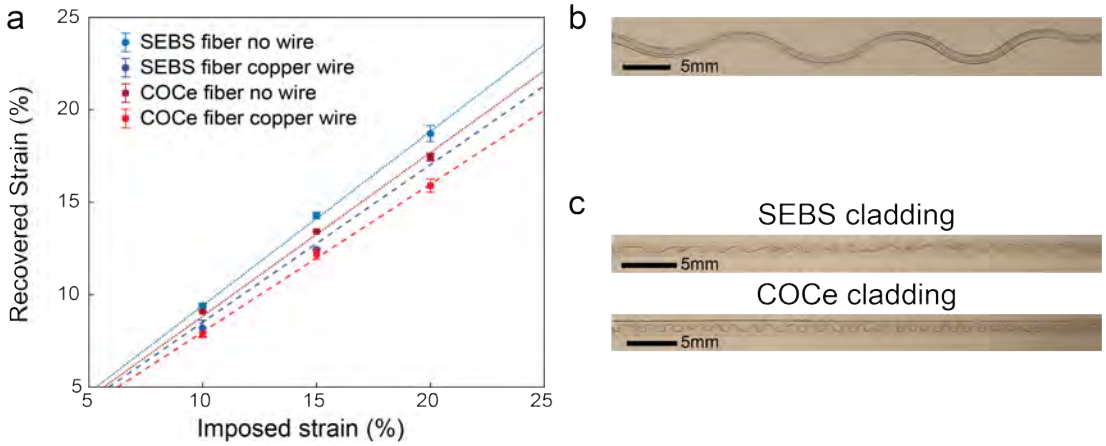


Figure 4-16: Effect of cladding material. (**a**) Recovered strain versus imposed strain for SEBS and COCe fibers without and with 50$\mu$m copper electrodes, respectively (n=5). The cross-sections of the fibers are identical. The slopes of the linear trends are 0.9412 (SEBS no wire), 0.8516 (SEBS copper wire), 0.8844 (COCe no wire), 0.7989 (COCe copper wire). (**b**) Lateral deformation of the cladding for an SEBS fiber with a 50$\mu$m tungsten electrode. Imposed strain is 10% (scale bar: 5mm). (**c**) The effect of the cladding material on the shape of the buckled electrode. SEBS and COCe fibers with 50$\mu$m copper electrodes ($\eta_{metal} = 41\%$). The cross-sectional areas are identical (scale bar: 5mm).

determines the Young's Modulus of a fiber.

## 4.5 Fatigue life

### 4.5.1 Curvature and fatigue life

The buckling parameters do not only alter $\eta_{metal}$ but also the shape of the electrode, which in turn influences its performance. When a fiber is elongated beyond $\eta_{metal}$, the wire quickly undergoes global plastic deformation under tensile loading. However, localized plastic deformation can also appear under bending, especially close to the surface of the wire, where bending strains are larger. Consequently, too high a bending curvature leads to plastic deformation while the electrode straightens. If this plastic deformation is not significant enough to visibly affect the conductivity of the electrodes, it still has noticeable effects, namely on its fatigue life. It is then important to consider the shape of the electrodes to evaluate their lifetime.

### 4.5.2 Calculation of wire curvature

Our model does not give the exact shape of the electrode after constrained buckling. However, just like for the buckling load, it is possible to calculate the lower and upper limit of the maximum value of curvature along the buckled wire. This does not take into account the effect of deformable walls described in section 4.4.4, but we can still calculate qualitative effects. Figure 4-17a shows that, for a given fiber geometry, the maximum curvature increases linearly with $\eta_{metal}$. It means that, for large $\eta_{metal}$, the fatigue life of the electrode might be lessened at strains that are close to the elasticity limit. Similarly, increasing the Young's Modulus of the wire or decreasing the gap size will increase the curvature at constant $\eta_{metal}$. However, for a given fiber cross-section and a given compressive strain, the total length of the wire does not influence the curvature when the fiber is longer than 10cm.

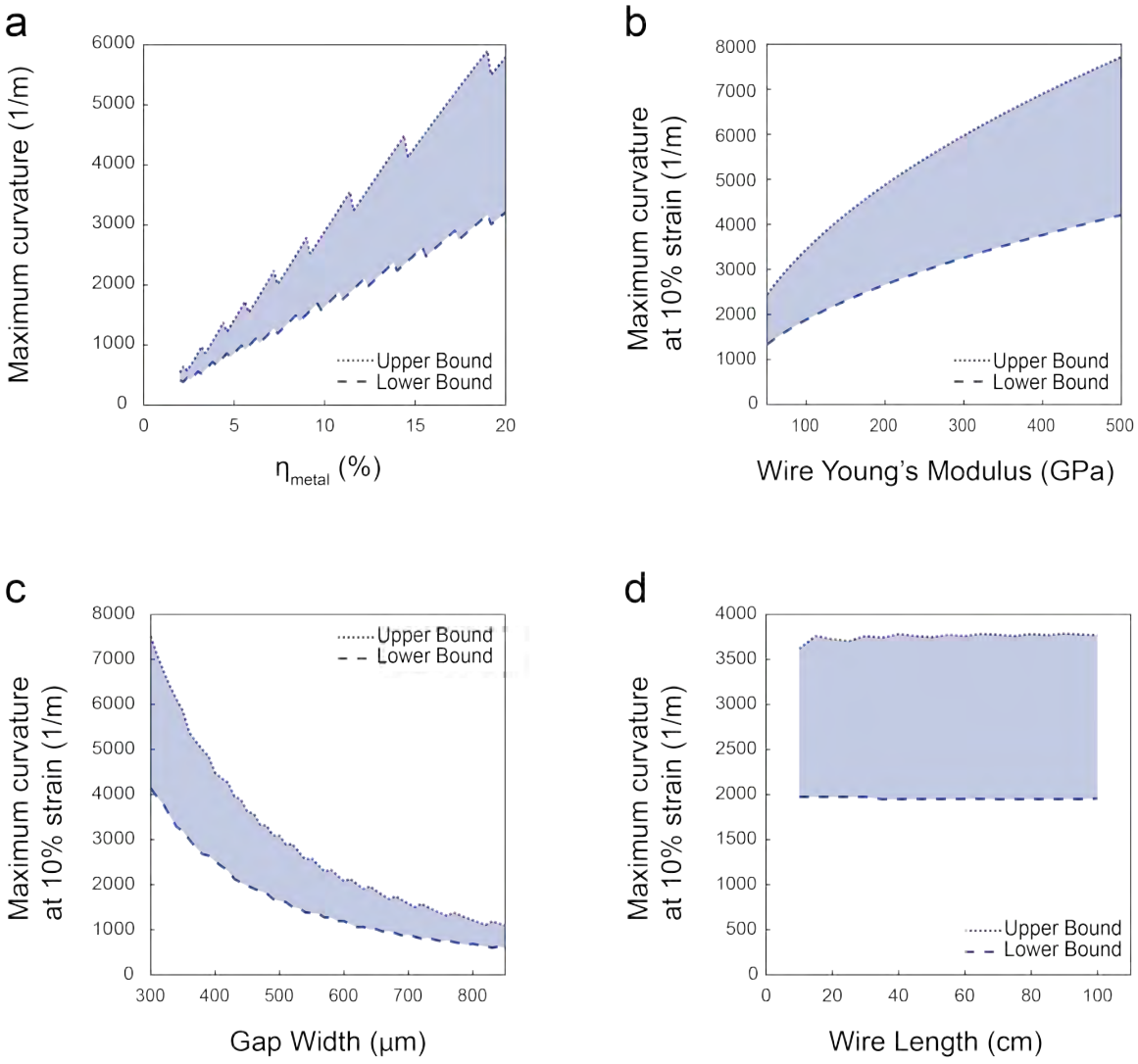


Figure 4-17: Change in maximum curvature of the buckled electrode depending on: (**a**) the compressive strain, i.e. $\eta_{metal}$ ($L_{metal} = 5$cm, $h = 500\mu$m, $E = 110$GPa) (**b**) the wire Young's Modulus $E$ ($\eta_{metal} = 10\%$, $L_{metal} = 10$cm, $h = 500\mu$m) (c) the size of the channel $h$ ($\eta_{metal} = 10\%$, $L_{metal} = 10$cm, $E = 110$GPa) (d) the total length of the wire $L_{metal}$ ($\eta_{metal} = 10\%$, $h = 500\mu$m, $E = 110$GPa)

### 4.5.3 Cycling test

Our measurements, presented in figure 4-18, illustrate the effect of curvature on the electrode lifetime, highlighting two main points.

For a given geometry, the lifetime of a fiber decreases when the cycling strain gets closer to $\eta_{metal}$ due to plastic deformation in bending. For example, in figure 4-18a-b,

we see that with two identical fibers with $\eta_{metal}$ = 25%, 10 000 cycles at 10% strain do not generate any change in resistance, while under 15% strain the electrode fails after 2 300 cycles.

For a given $\eta_{metal}$ and a given cycling strain, higher curvature leads to a shorter lifetime. Experimentally, we increase the curvature of the electrode by reducing the width of the channel. Photographs of the fibers were taken using a Canon EOS 90D camera and a 50mm compact macro lens. A MATLAB script was written to measure the arc length and to calculate the curvature along the length of the electrode from the photographs. Here, we observe that a curvature of the buckled electrode exceeding 2 $mm^{-1}$ drastically reduces the number of the sustained cycles (Figure 4-18c-d).

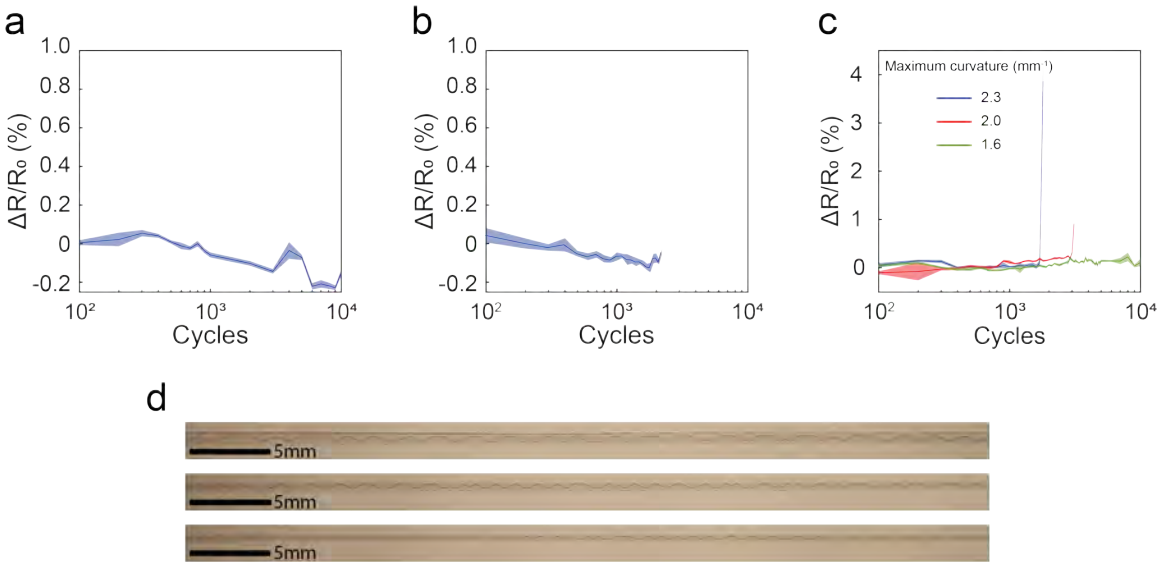


Figure 4-18: Change in resistance of the fibers upon cyclic stretching: (**a**) COCe fiber - 50$\mu$m copper buckled electrode ($\eta_{metal}$ = 25%; imposed strain= 10%). (b) COCe fiber - 50$\mu$m copper buckled electrode ($\eta_{metal}$ = 25%; imposed strain=15% ). Break occurs after 2300 cycles. (**c**) Effect of the electrode curvature on its lifetime. COCe fibers - 50$\mu$m copper buckled electrode ($\eta_{metal}$ = 7.7%; imposed strain= 5%). Breaks occur after 1800 and 3100 cycles, respectively. The maximum curvatures are reported. (**d**) Pictures of the fibers used in c.

Despite the variability arising from the geometry of the electrode, we note that our buckled electrodes can sustain thousands of stretching cycles. This point will be discussed more in section 4.6.2.

## 4.6 Limitations

This sections will discuss the limitations of our buckled electrode approach, and possible developments to overcome, circumvent or minimize them.

### 4.6.1 Electrode footprint

A rightful criticism of our approach could point at the dimensional footprint of an electrode. If the electrode itself is small ($\sim 50\mu$m), the channel that contains it holds a significant part of the fiber cross-section. This could render designs with multiple electrodes difficult to realize and could prevent going towards increasing device density.

We see several ways to work around this difficulty:

- To reduce the channel area while maintaining elasticity one can leverage a few approaches: for example, pre-strain the cladding to a higher value and still achieve the same elasticity now in a smaller channel. Alternatively, one can reduce the channel size and at the same time use a smaller wire. This is the beauty of a multi-parameter system, that there are many knobs to turn.
- Since the buckling event occurs primarily in a plane, one can reduce further the channel height and, in doing so, allow for multiple channels to exist side by side in the fiber cross section. To demonstrate this approach a fiber with 4 channels was fabricated. The details of this fiber is shown in figure 4-19a-d.
- The channels are not limited to a single conductor. We have demonstrated experimentally that up to four insulated electrodes can be buckled concurrently in a single channel. One can in principle increase the number of wires beyond that. This approach is illustrated in figure 4-19e, and also allows us to connect LEDs in parallel in the fiber, as shown in chapter 7. Our experiments show that the buckled twin wires maintain their insulation over usage.
- Alternatively, buckling can be enforced in cylindrical channels. This 3-dimensional buckling allows to reach high elasticity while maintaining a lower curvature than the 2D approach. We make use of this technique in section 7.3 but we have not

systematically studied it.

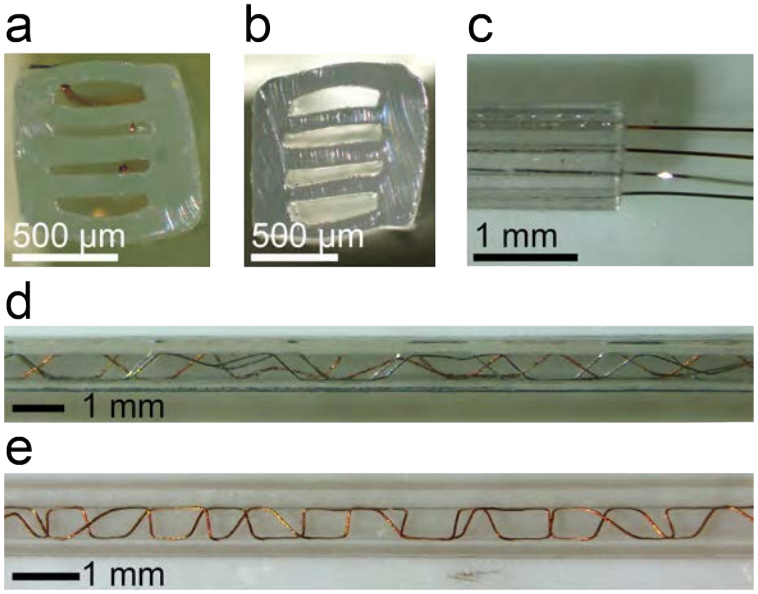


Figure 4-19: (**a,b**) Cross-sections of COCe (a) and SEBS (b) fibers with four stacked electrode channels. (**c**) Side view of an SEBS fiber with 50$\mu$m copper electrodes coming out of the four stacked channels. (**d**) Top view of an SEBS fiber with four 50$\mu$m buckled copper electrodes in stacked channels. (**e**) Top view of a COCe fibers with two insulated 50$\mu$m buckled copper electrodes in a single channel.

### 4.6.2 Fatigue life

Fatigue life is an important aspect of fabric performances, especially when considering garments that are used repeatedly. In section 4.5 we pointed out that, although our electrodes can have high elasticity, their lifetime decreases in the upper range of elastic deformation. It is useful to put the results into context: in wearables, high yarn strains ($\geq$ 10%) are experienced when donning and doffing the garment. Then 2000 cycles at 15% strain correspond to a lifetime of 5.5 years for a garment worn every other day. Thus we believe that the cycling performances of our electrodes are fitted for the targeted applications.

### 4.6.3 Limit of the buckling regime

When the load required to buckle the electrode becomes too high, local buckling is no longer energetically favorable, and we instead observe a global buckling of the whole fiber (Figure 4-20).

This phenomenon has been studied in depth for stiff thin films bonded to pre-stretched elastomeric substrates [68, 81, 82]. A detailed analysis is beyond the scope of this work, but it is interesting to consider the different contributions to the mechanical energy of our system. In a first approximation, one can consider two terms in the total potential energy: the stretching energy of the elastomeric cladding and the bending energy of the buckling wire. Assuming uniaxial stress, the stretching energy of the cladding is given by:

$$U_{stretch} = \frac{1}{2} E_{clad} A_{clad} L_0 \cdot (\varepsilon_{clad} - \varepsilon_\Delta)^2 \tag{4.7}$$

where $L_0$ is the initial length of the cladding, $E_{clad}$ is the Young's modulus of the cladding, $A_{clad}$ is the cross-sectional area of the cladding, and $\varepsilon_\Delta$ is the relaxed cladding strain.

The bending energy of the electrode is much more complicated to evaluate. Assuming pure planar bending, and using the small deformation analysis developed by Chai [75], one can obtain, the following approximation for the bending energy:

$$U_{bend} = \frac{1}{2} nh\sqrt{PEI} \tag{4.8}$$

with $n$, $h$, $P$, $E$ and $I$ defined earlier. During the polymer relaxation, for a given $\varepsilon_\Delta$, that leads to a particular buckled configuration of the wire, the total energy varies such that:

$$U_{total} = \frac{1}{2} E_{clad} A_{clad} L_0 \cdot (\varepsilon_{clad} - \varepsilon_\Delta)^2 + \frac{1}{2} nh\sqrt{PEI} \tag{4.9}$$

Knowing that $P$ depends on $n$, $h$, $E$, $I$ and $\varepsilon_\Delta$, one can appreciate the complexity of the problem. Depending on the value of the different parameters, an energy minimum along $\varepsilon_\Delta > 0$ may not exist. In this case, the buckling of the electrode

is not favorable and we observe a global collapse of the fiber. We also observed experimentally that, sometimes, the buckling of the wire starts normally, and beyond a certain compression strain, the whole fiber undergoes a buckling instability. Then the globally buckled shape corresponds to the mode of the wire at the onset of instability (Figure 4-20 left). This scenario happens in conditions similar to the ones leading to no buckling at all: soft cladding (SEBS), small $h$ ($\leq 200\mu$m), large $\varepsilon_\Delta$ ($\geq 30\%$) and stiff wire ($50\mu$m tungsten and stiffer).

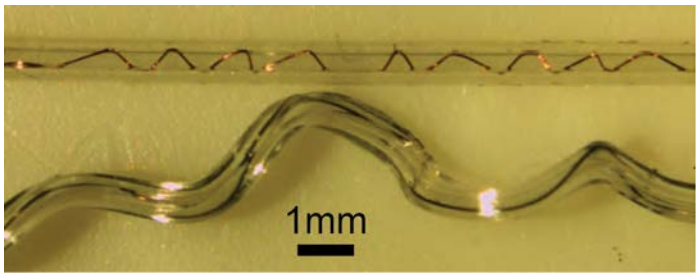


Figure 4-20: Example of the limit of buckling. Top: $40\mu$m copper wire in a $500\mu$m gap in COCe. $\varepsilon_{clad} = 30\%$. Local buckling of the wire is energetically favorable. Bottom: $50\mu$m tungsten wire in a $200\mu$m gap in SEBS. $\varepsilon_{clad} = 50\%$. Local buckling of the wire is not energetically favorable and the whole fiber deforms in global buckling.

## 4.7 Discussion

In this chapter, we established a method to fabricate curved metal electrodes in elastic fibers through buckling. We explained how these fibers could be produced at scale and showed a proof-of-concept apparatus. We then studied the properties of our fibers and found that up to strains equal to the excess metal length $\eta_{metal}$:

- The electrical conductivity of the electrode remains constant.
- The mechanical properties of the fibers are identical to those of an elastomeric fiber without electrode.

$\eta_{metal}$ is the key characteristics of these fibers. Another critical feature of these fibers is the maximum curvature of the electrode, which will impact its lifetime.

An analytical model, further confirmed through experimentation, allowed us to explore in detail this multi-parameter system. In figure 4-21 and 4-22, we summarize the influence of the different geometric and material parameter on $\eta_{metal}$ and on the maximum electrode curvature. A given functionality and use case for a fiber will entail specific constraints in terms of required mechanical properties and cross-sectional geometry. By playing on all these parameters independently, one can avoid extreme cases where buckling of the wire would not be energetically favorable, and design a fiber that fulfill the necessary requirements.

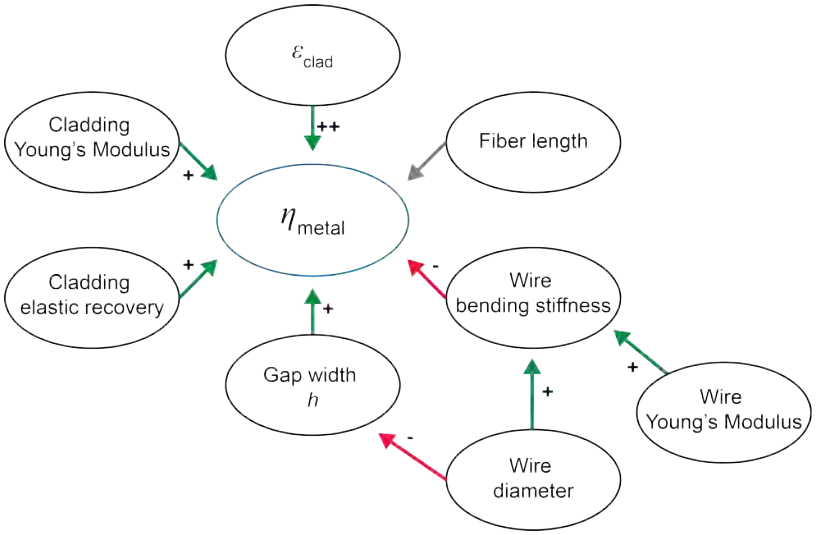


Figure 4-21: Summary of the influence of different parameters on $\eta_{metal}$. A green arrow with a "+" indicates a positive correlation. A red arrow with a "-" indicates a negative correlation

Chapters 6 and 7 will revolve around this method to weave and knit conductive fibers, and enable functional fibers by connecting micro-devices via buckled electrodes. The published version of this work can be found at [32].

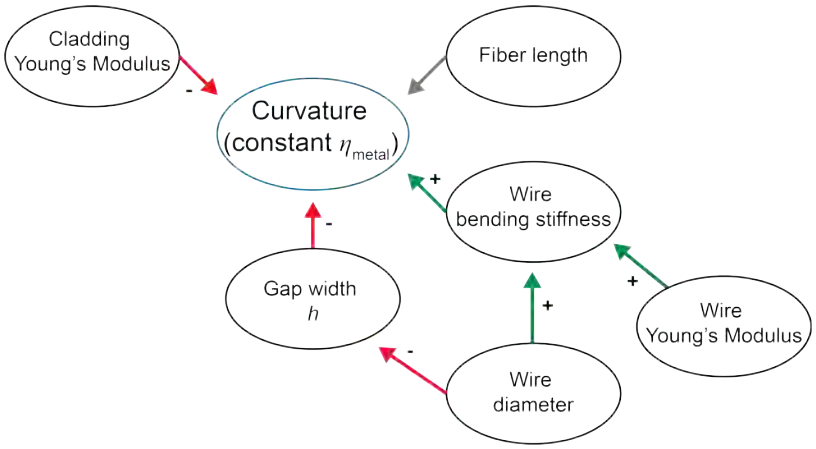


Figure 4-22: Summary of the influence of different parameters on the electrode curvature, for a fixed value for $\eta_{metal}$. A green arrow with a "+" indicates a positive correlation. A red arrow with a "-" indicates a negative correlation

# Chapter 5

# In-fiber helical electrodes

## 5.1 Fiber fabrication

### 5.1.1 Principle

In this second approach, the cladding and the metal wire are deformed simultaneously to create a helical electrode geometry. Helical carbon black-elastomer composite electrodes in thermally drawn fibers have been fabricated by Zhang et al. [74] by rotating the preform during the draw. This approach, and our reasons for choosing a different one, are discussed in appendix B. Here, a solid metal wire was drawn into an elastomeric cladding to produce a fiber with an off-centered straight electrode. The fiber was then twisted and annealed at 20 $^{o}$C below the polymer melting point. This process is illustrated in figure 5-1a. The stress accumulation in the cladding during twisting relaxes during annealing, creating a helical electrode within a linear cladding. Excessive twisting can result in a torsional instability, which causes the fiber to lose its linearity [83, 84]. However, successive small steps of twisting and annealing can help mitigate this issue. This post-draw treatment of the fiber can be performed at scale, as described in section 5.1.2. The different geometric parameters of the helix are related by:

$$L_{metal} = 2\pi \frac{L_f}{p} \sqrt{r_h^2 + \frac{p^2}{4\pi^2}} \tag{5.1}$$

$L_{metal}$ is the arc length of the helix, $L_f$ is the length of the fiber, equal to the pitch of the helix times the number of turns. $p$ is the pitch and $r_h$ is the radius of the helix. Here, the excess metal length in helical electrode fibers becomes:

$$\eta_{metal} = \sqrt{1 + (\frac{2\pi r_h}{p})^2} - 1 \tag{5.2}$$

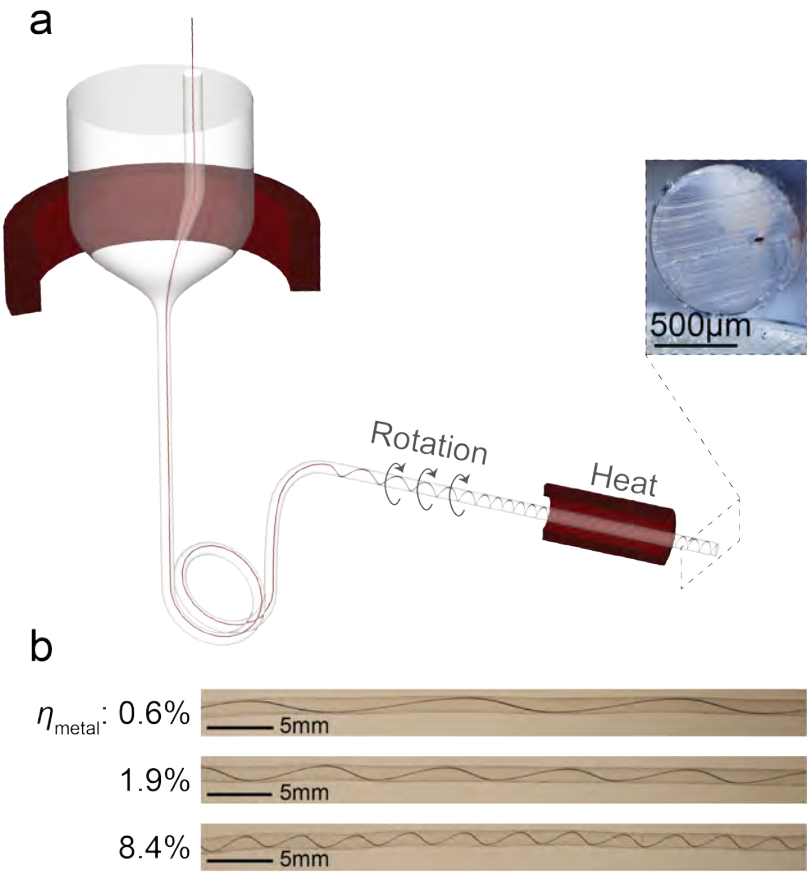


Figure 5-1: (**a**) Fabrication of the helical electrodes. Inset: a cross-section of the COCe fiber containing a 50$\mu$m copper wire. (**b**) Different COCe fibers with helical 50$\mu$m copper electrodes.

Figure 5-1b displays copper helical electrodes with various values of $\eta_{metal}$ within COCe fibers. Fibers more than 5 meters long, integrating a continuous helical electrode, with a pitch down to 3 mm were produced. $\eta_{metal}$ up to 13% was achieved.

### 5.1.2 Large scale apparatus

We designed a large scale twist-and-anneal line process, inspired by traditional textile yarn manufacturing techniques. Twisting is a routine process in yarn manufacturing as most yarns are composed of multiple strands twisted together. A common twisting set up comprises a false-twisting device followed by a real twister [85, 86]. A false-twisting device inserts a twist in the middle of a yarn, so that the sections upstream and downstream of the device are twisted in opposite directions. As a result, the yarn has no net twist after travelling through the device. A real twister acts at the end of the yarn and introduces a permanent twist. Texturing is another common step in yarn manufacturing [87]. A yarn made of straight strands goes through an annealing furnace and a false-twisting device. The furnace introduces a permanent deformation in the strands so that, when they untwist after the false twisting device, the final yarn is crimped. To fabricate helical electrodes, we designed a set up that is a combination of the texturing and the twisting processes, depicted in figure 5-2a. The fiber first travels through an annealing furnace and a false-twisting device to imprint the twisting deformation. For the false-twisting device, we chose a rotating pin. The pin rotates around its own axis allowing the fiber to travel, and around the fiber's axis to twist it. After the pin, a real twister is added to counter the reverse twisting. In our design, we chose a ring spinning device, which is used both for twisting and pulling the fiber. Such a setup can be mounted in the continuity of the draw, leading to scalable manufacturing of the helical electrode fibers. To validate our design, we fabricated a simplified apparatus including the key elements (Figure 5-2b-c). Our experimental setup consists of an annealing furnace and a rotating pin between two sets of rollers. Although the fiber undergoes reverse twisting downstream of the pin, this twist is not permanent, contrary to the twist upstream of the pin, and it relaxes after the second set of rollers due to the cladding's elasticity. As a result, the wire within the resulting fiber exhibits the amount of twist imposed upstream of the rotating pin. The setup can be used both for batch processing, where the fiber does not move during annealing, or for continuous processing, where the fiber is continuously slowly

pulled, twisted, and annealed, just like in the texturing process. The final elasticity of the fiber is controlled by its geometric and materials characteristics. In the batch process, the pitch of the helix is given by the number of turns of the pin divided by the distance between the first roller and the pin. In the continuous process, the pitch is equal to the twisting speed of the pin (turns/min) divided by the pulling speed of the rollers (m/min). Using our batch process, we produced 5 meters of continuous helical 50$\mu$m copper electrodes within the COCe fiber. In our experiment, the pin speed was set to 10 turns/min and the roller speed was set to 25cm/min.

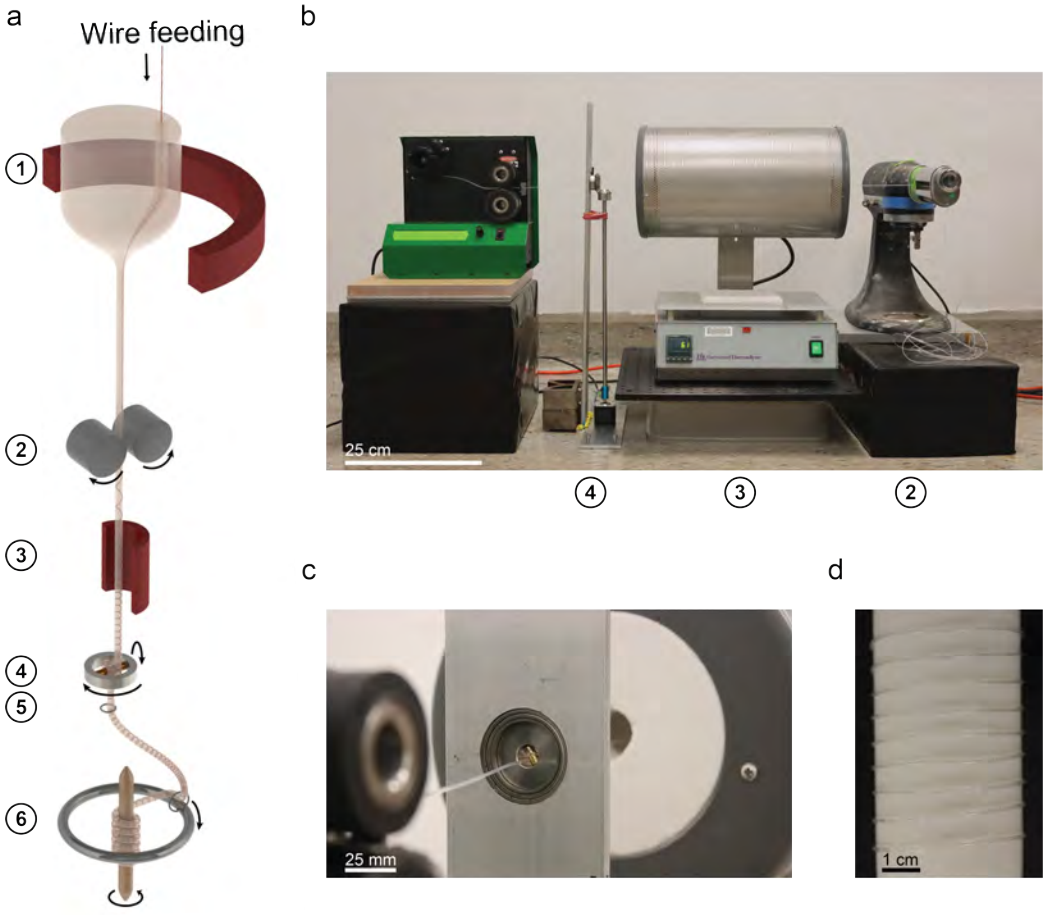


Figure 5-2: (**a**) Design of a large scale set up to fabricate helical electrodes in the continuity of the draw. 1: Fiber drawing furnace. 2: Drawing rollers. 3: Annealing furnace. 4. False-twisting device: rotating pin. 5: Guiding ring. 6. Ring spinning. (**b**) Experimental twist-and-anneal apparatus (same legend as (a)). (**c**) Experimental false-twisting device. (**d**) Spool of 2m of continuous fiber with a 50$\mu$m helical copper electrode.

## 5.2 Insights into the deformation mechanism

In fibers with helical electrodes, because the wire cannot slip relative to the polymer, we foresee that the tensile behavior will not be easily captured by a simple parameter such as $\eta_{metal}$. Thus we will approach this problem differently from the buckled electrodes. We start by presenting some mechanistic clues that will then help us understand the mechanical behavior of the fibers.

### 5.2.1 Geometrical behavior of a helix and a rod of elastomer

To evaluate the performances of a helical structure inside a stretchable cladding, we first made a "back-of-an-envelope" model, to identify its key features.

Let us consider a helical metal wire wrapped around a rubber rod. When free-standing, the maximum structural elongation of the metal wire is $\eta_{metal}$, when the helix becomes straight. However, the helix is a closed geometry, and here contains a cylindrical volume of solid elastomer. When a helix straightens, the volume inside the spires decreases towards zero. Here this is made impossible by the presence of the elastomer inside, so elongation up to $\eta_{metal}$ cannot be achieved.

To get a better idea of how this change in contained volume impacts elasticity, we look at the change in radius of a helix versus a polymer rod upon elongation (when they are separate). Both have the same initial radius. We assume that:

1. The arc length of the helix, $L_{metal}$, is constant (no material elongation, pure bending deformation).
2. The helix deforms as a longer helix with the same number of turns and a smaller radius.
3. The radius of the polymeric cylinder changes due to Poisson's effect.
4. The polymer is incompressible (Poisson's ratio $\nu = 0.5$). This is a reasonable approximation for elastomers.

All these assumptions are valid for small enough deformation.

Using the conservation of length for the helix we calculate the radius of the helix

depending on the applied strain $\varepsilon$:

$$r_{h,\varepsilon} = \sqrt{r_h^2 - \frac{p^2}{4\pi^2}((\frac{\varepsilon}{100}+1)^2 - 1)} \tag{5.3}$$

Poisson's law gives for the radius of the rod of elastomer:

$$r_{el,\varepsilon} = r_{el} \cdot (\frac{\varepsilon}{100}+1)^{-\nu} \tag{5.4}$$

where $\varepsilon$ is the elongation in %, $r_{el}$ is the initial radius of the elastomer cylinder. We note that $r_{el}$, $r_h$ and $p$ are the values in the initial configuration. The underscore $\varepsilon$ indicates values in the deformed configuration.

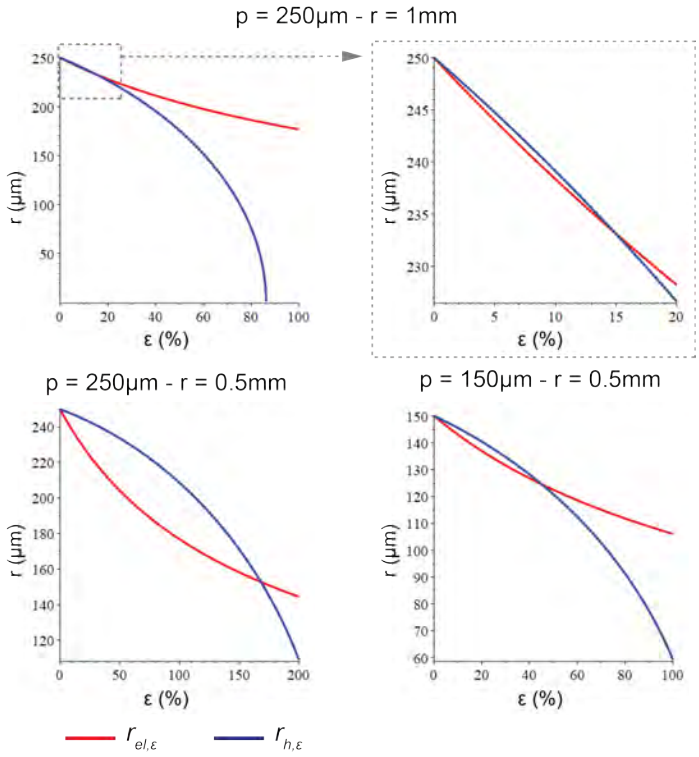


Figure 5-3: Evolution of the radii of a polymer cylinder and a helix.

The evolution of the two radii with elongation is represented in figure 5-3. We can see that the radius of the helix decays much faster than the polymer's. Hence the volume of the cylinder inscribed in the helix quickly decreases. In the case of the fiber, this volume is filled with the elastomer, and the helix is compressing the polymer as it

deforms, with a compressive strain that increases with the relative change in radius of the helix. Because the elastomer is roughly incompressible, a compressive shear strain will quickly build up inside the metal wire, which can lead to plastic deformation and failure. We find that the strain at which the two radii overlap depends mostly on the ratio $r_h/p$.

This very simplistic approach does not take into account the outer part of the cladding and the fact that there should be permanent contact and no slip between the metal and the polymer. However, it reveals two key points: the limitation of a closed geometry and the importance of the $r/p$ parameter.

### 5.2.2 Helical Auxetic Yarns (HAYs)

HAYs are a two-component yarns used to create textiles with auxetic properties [88, 89]. They comprise a low modulus, initially straight core fiber, helically wrapped by a smaller, higher modulus fiber. Upon tensile elongation, the width of the yarn increases, thanks to a helical deformation of the core. One could consider the fiber with helical electrode as a HAY made of a copper wire wrapped around an elastomeric core, encapsulated in an outer layer of the core material with thickness $t$ (Figure 5-4a). The similarity is emphasized when looking at the deformation of the fiber under tension tensile strain: just like a HAY, the radius of the wrap fiber (the metal helix) decreases, and the core deforms into a helical configuration to accommodate the inhomogeneous compression, as illustrated in figure 5-4b-d.

HAYs have been the topic of numerous studies that probe the effects of material and geometric parameters [90, 91, 92]. Among the geometrical parameters are the radii of the two fibers and the parameters of the wrapped helix. Studies show that, for given wrap and core materials, the main geometric parameter controlling the mechanical properties is the initial wrapping angle of the helix, or the angle between the helical wire and the cross section of the fiber. It is given by:

$$\alpha_0 = \arctan(\frac{p}{2\pi r_h}) \tag{5.5}$$

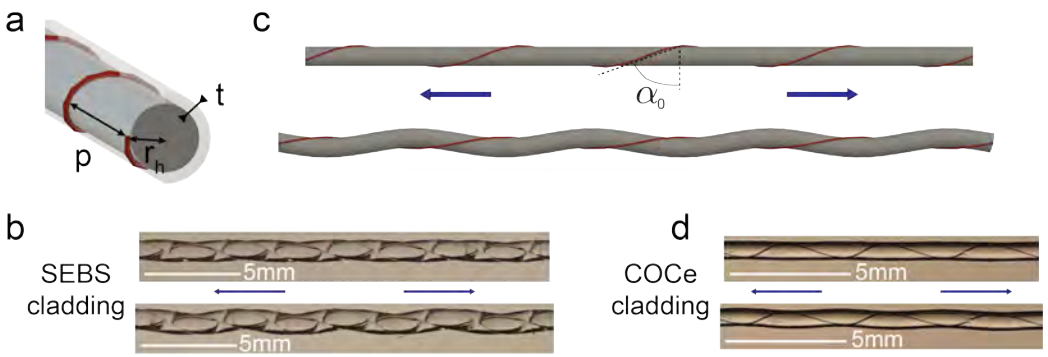


Figure 5-4: Comparison of the fibers with a Helical Auxetic Yarn. (**a**) Geometry of the fibers seen as a HAY encapsulated in a layer of cladding material. (**b**) Typical deformation of a HAY under tension. (**c**,**d**) Deformation of SEBS and COCe fibers under tension. Top: no strain. Bottom: 1.5% strain.

Here again, we find the importance of the ratio between $p$ and $r_h$.

Although the two model systems presented in this section are naive and fairly different from a fiber with helical electrodes, the observations made here will prove very helpful during the experimental mechanical study of the latter.

## 5.3 General electro-mechanical behavior

### 5.3.1 Tensile properties

Under tensile loading, the fibers exhibit two regimes of stress-strain behavior (Figure 5-5a). At small strains, the stress increases linearly, and is higher than that of the pure elastomeric fibers. Following a yield-like stress rollover, the stress increases with a lower slope, until the wire breaks. As expected, the strain at the inflection point is noticeably different from $\eta_{metal}$.

The stress-strain curves of different SEBS fibers with 50$\mu$m helical copper electrodes, presented in figure 5-5b, reveal that the geometry influences both the strain at the inflection point and the Young's modulus of the fiber. Applying strain cycles with increasing amplitudes to the fibers, we find that the inflection point corresponds to the onset of non-recoverable deformation, whereas a pure SEBS fiber shows full recovery for the same strains (Figure 5-5c). We identify this point as the yield strain

of the fiber, which corresponds to the plastic deformation of the metal wire.

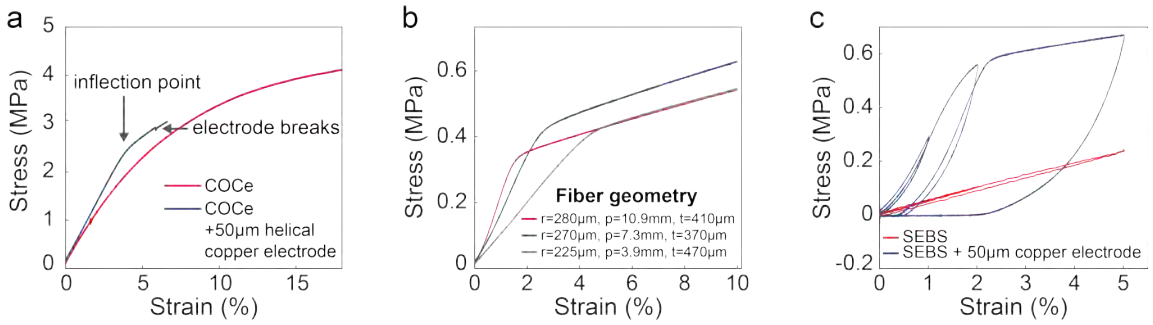


Figure 5-5: (**a**)) A stress-strain curve of the COCe fiber with (blue) and without (red) a helical copper electrode ($\eta_{metal} = 5\%$). (**b**) Tensile test for different fiber geometries. SEBS – 50$\mu$m helical copper electrode. (**c**) Stress versus strain for stretching cycles of increasing amplitudes, with and without a helical electrode.

We now want to determine how the geometry of the fiber determine its yield strain. Advised by our previous analysis, we find $\alpha_0$ to also be the key geometric parameter in our fibers. For a given wire and cladding material, $\alpha_0$ controls the yield strain linearly, in the range of parameters of the study, capturing the combined effects of $p$ and $r$, as shown in figure 5-6. For large $\alpha_0$, the radius of the helix decreases faster upon tensile strain, leading to a quicker yield. $\alpha_0$ does not take into account the thickness of the outer cladding, $t$, but in our experiments, $t$ shows no meaningful effect on the yield strain (Figure 5-6).

Our study shows that the fibers with helical electrodes exhibit a very clear elastic range of deformation and, for given materials, one can predict the elasticity limit of the fibers from the geometric parameters of the helix, specifically from the value of $\alpha_0$.

### 5.3.2 Electrical properties

Through mechanical characterization, we identified the point where the electrodes undergo severe plastic deformation. We are now interested in studying the conductivity of the electrodes in the range of elastic deformation of the fibers.

At rest, the fibers containing helical copper electrodes exhibit an average resistivity of $1.92 \cdot 10^{-8} \pm 0.35 \cdot 10^{-8}$ $\Omega$.m (n=7), which increases slightly with $\eta_{metal}$, due to the

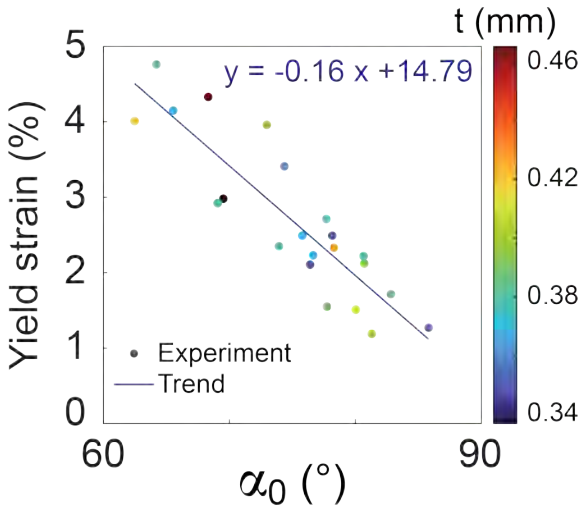


Figure 5-6: Yield strain of the fiber depending on the initial wrapping angle $\alpha_0$. SEBS - 50$\mu$m copper electrode. Color bar: thickness $t$ of the outer layer of cladding.

increased trace length of the electrode.

The electrical characterization is the same as for the buckled electrodes. We applied tensile elongation on the fibers while simultaneously recording the tensile load and the resistance of the electrode (Figure 5-7a). Up to the mechanically identified yield, the resistance varies by less than 0.3%. As expected, an increase in resistance coincides with the yield strain of the fiber, as the electrode deforms plastically.

To confirm this observation, we apply strain cycles of increasing amplitude to the fibers and measure the resistance between the cycles (Figure 5-7b). Hysteresis appears when the amplitude of the cycles exceeds the yield strain predicted by $\alpha_0$. This result corroborate the identification of the yield point and validates our ability to predict the yield strain of the fiber through a linear relationship with $\alpha_0$.

We presented in-fiber electrodes that exhibit constant, high conductivity over a controllable range of elastic deformation. As $\alpha_0$ captures the influence of the helix geometry on the limit of elasticity, we now want to understand more precisely the effect of materials choice on this limit, as well as the impact on the Young's modulus of the fiber.

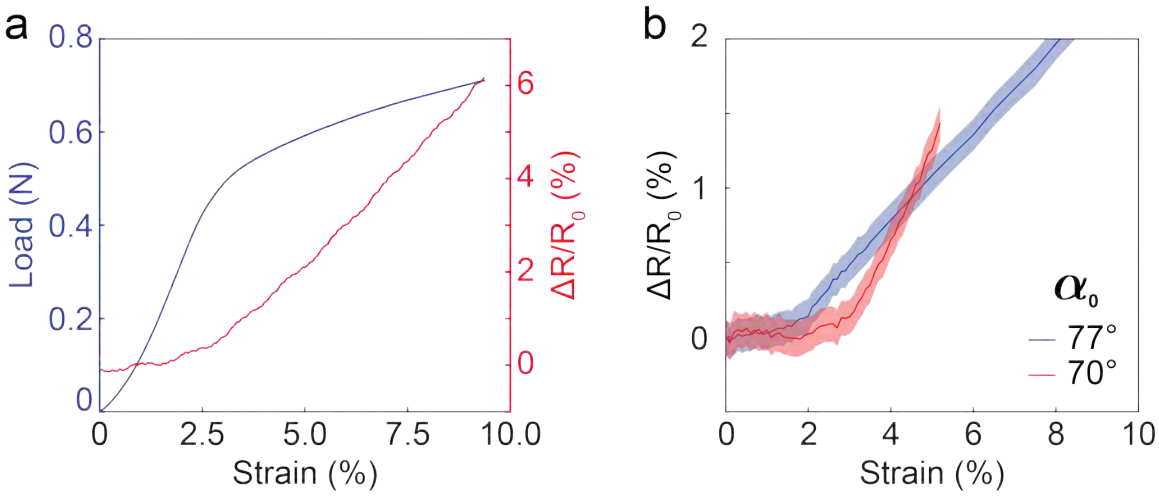


Figure 5-7: (**a**) Simultaneous measurement of force and change in resistance during tensile deformation of a SEBS fiber with a 50$\mu$m helical copper electrode ($\alpha_0$ = 80°). (**b**) Change in resistance of the electrode after stretching cycles of increasing amplitude. SEBS fibers with a 50$\mu$m helical copper electrode. Yield strains expected from the value of $\alpha_0$: 2.4% and 3.6%. The amplitude of the cycles is increased by 0.1% steps. The shaded area indicates the standard deviation of the mean

## 5.4 Control of the mechanical properties

### 5.4.1 Effect of the cladding material on the yield strain

When SEBS is replaced with a higher modulus elastomer such as COCe, the slope of the yield strain versus $\alpha_0$ curve decreases, leading to lower yield strains (Figure 5-8). This result could be expected as a material with higher modulus will be less prone to deforming under the compression from the wire, and stress in the electrode will build up faster.

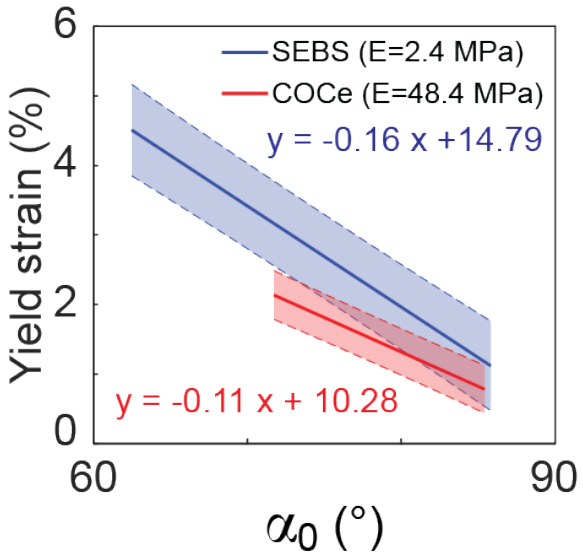


Figure 5-8: Effect of the cladding material on the yield strain of the fibers. All fibers contain a 50$\mu$m copper wire. The shaded area is the 75% confidence interval.

### 5.4.2 Control of the Young's modulus

Our experiments showed that the change in Young's modulus of the fiber could not be captured by $\alpha_0$ only. Therefore, we consider the fiber as a composite material made of a helix and a cladding loaded parallel to each other, and apply the rule of mixtures:

$$E_{composite} = \frac{E_{wire} \cdot A_{wire} + E_{cladding} \cdot A_{cladding}}{A_{fiber}} \tag{5.6}$$

where $E_{wire}$ and $E_{cladding}$ are the Young's moduli, and $A_{wire}$ and $A_{cladding}$ are the cross-sectional areas of the wire and the elastomer cladding, respectively. Here $E_{wire}$ is an effective modulus defining the force needed to extend the wire in its helical configuration, which is likely related to $\alpha_0$. Because the cross-sectional area is largely dominated by the cladding, we can approximate the composite modulus as:

$$E_{composite} = \frac{E_{wire} \cdot A_{wire}}{A_{fiber}} + E_{cladding} \tag{5.7}$$

A linear relationship between the fiber Young's modulus, $E_{composite}$, and $(\tan(\alpha_0) \cdot A_{wire}/A_{fiber})$ (Figure 5-9) corroborates that the rule of mixtures captures

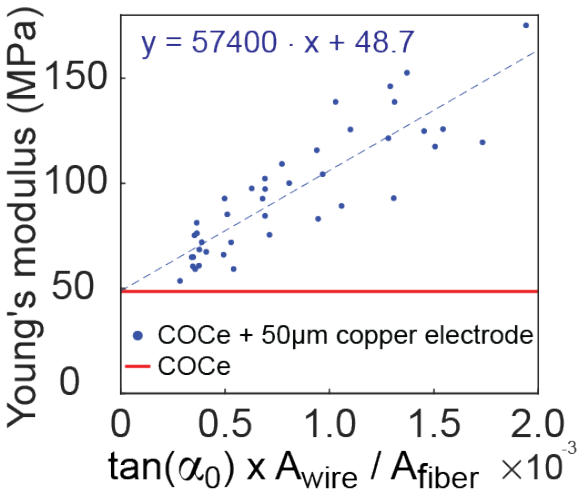


Figure 5-9: Adaptation of the rule of mixtures to the helical electrode fibers: Young's Modulus of COCe - 50$\mu$m copper fibers versus $(\tan(\alpha_0) \cdot A_{wire}/A_{fiber})$. Red line: measured Young's Modulus of COCe fibers without electrode (48.4 MPa, n=4).

the mechanical response of these fibers. By varying $\alpha_0$ and $A_{fiber}$ across samples, it was found that, as $(\tan(\alpha_0) \cdot A_{wire}/A_{fiber})$ approaches zero (which corresponds to cladding alone with no helical wire), the effective modulus of the fiber trends towards the Young's modulus of the pure elastomer fibers (48.4 MPa for drawn COCe fibers). A linear regression on the data in Figure 5-9 gives:

$$E_{fiber} = 57400 \cdot \tan(\alpha_0) \cdot A_{wire}/A_{fiber} + 48.7MPa \tag{5.8}$$

This analysis demonstrates that $\tan(\alpha_0) = \frac{p}{2\pi r_h}$ and the cladding material together dictate the equivalent Young's modulus of the helices embedded in the elastomer. By doing so, they directly dictate the Young's Modulus of the elastomer fiber with embedded helical electrodes, through the rule of mixture.

### 5.4.3 Increasing the yield strain

With the fibers described in the previous sections, we managed to go down to a 3mm pitch, reaching 5% elasticity. When trying to twist the fibers further, the electrode would break. Hence we engineered fibers with a hollow core within the wire helix in order to reach higher elasticity. The hollow core readily afforded smaller pitches,

and hence smaller wrapping angles, leading to yield strains up to 10%. With a fiber comprising a hollow core making up 25% of the fiber's volume, $p$ could be decreased to 1.7 mm, manifesting in $\alpha_0 = 49.6°$ and permitting strains >10% (Figure 5-10).

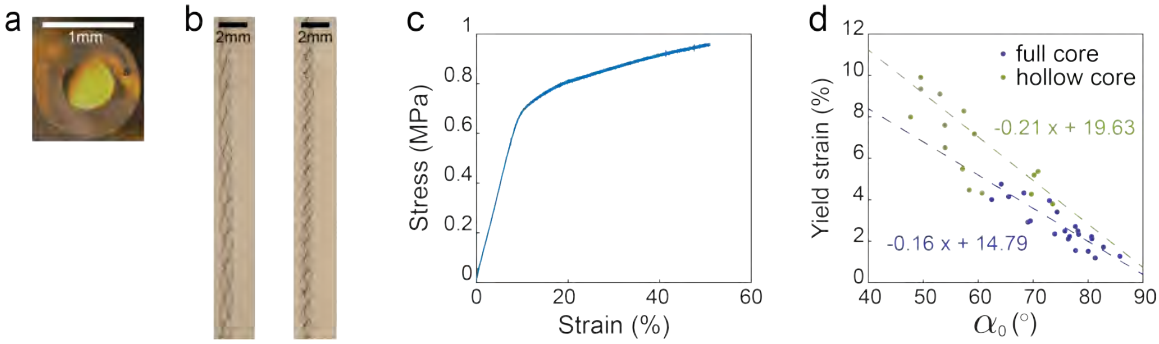


Figure 5-10: (**a**) A cross-sectional micrograph of a fiber with a 25% hollow core and a helical electrode. (**b**) Left: fiber with a full core and 3mm pitch. Right: fiber with a hollow core and 1.7mm pitch. (**c**) Stress-strain curve of a fiber with a 25% hollow core and a helical electrode. $\alpha_0 = 52.4°$. (**d**) Yield strain of fibers depending on the initial wrapping angle $\alpha_0$. Comparison of fibers with a full core to those with a 25% hollow core. Here, all fibers are composed of SEBS with a 50$\mu$m copper electrode.

Two interesting observations arose from these hollow core fibers. First, at such small pitches, the fibers coil and lose their straight configuration (figure 5-10b). However, as shown in figure 5-10c, the stress-strain behavior remains the same as for the straight fibers, featuring two distinct regimes of elastic and plastic deformation. Second, when measuring the yield strain of these fibers and plotting it against $\alpha_0$ (figure 5-10d), we find a different linear trend, resulting in higher yield strain for the same angle. We believe that the hollow core facilitates the compression of the elastomer inside the helix, thus delaying the build up of stress in the wire. Further experimentation and modelling are needed to understand this phenomenon.

## 5.5 Fatigue Life

Our experiments revealed excellent fatigue performances for the fibers with helical electrodes. For example, in figure 5-11, we demonstrate that a SEBS hollow core fiber, including a 50$\mu$m copper helical electrode with $\alpha_0 = 49.6°$, can sustain more than 10 000 cycles of 10% tensile strain with less than 0.2% change in resistance. Let

us notice that the expected yield strain for this fiber is 9.2%. However, figure 5-6 and figure 5-10d show that there is a rather significant error associated with the linear trends, which explains why this fiber could exhibit 10% elasticity. Remarkably, this result also illustrates the fact that the exceptional fatigue life remains unchanged over the whole range of elastic deformation. This is a significant difference with, and an advantage over the buckled electrodes: until the macroscopic yield of the fiber, there seems to be no localized bending plasticity.

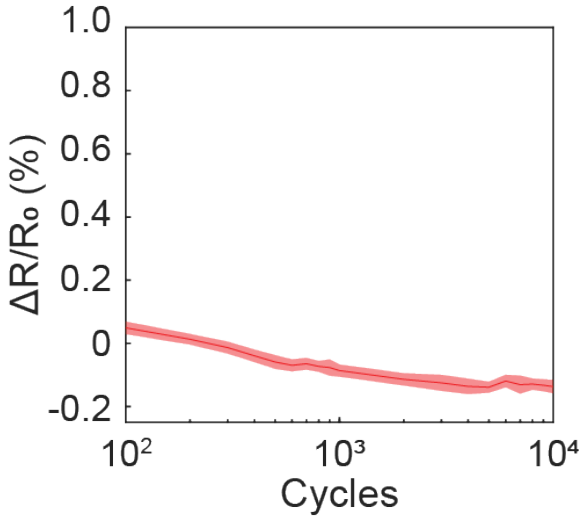


Figure 5-11: Change in resistance of the fibers upon cyclic stretching. SEBS - 50$\mu$m copper helical electrode - a 25% hollow core ($\alpha_0 = 49.6°$; expected yield strain = 9.3% imposed strain = 10%).

## 5.6 Discussion and next steps

In this chapter, we demonstrated a fabrication approach to produce helical metal electrodes in elastic thermally drawn fibers. Our twist and anneal technique is shown to be scalable through a proof-of-concept apparatus. Through theoretical and experimental insights, we found that the helix wrapping angle controls the maximum elasticity of the fibers. We also established a rule of mixture that captures the influence of the wrapping angle and the cladding modulus on the fiber Young's Modulus.

Many more aspects of the helical geometry should be studied, in order to expand the potential of this approach. For instance, future studies could involve:

- Finite Element Modelling of the fiber system, using a hyperelastic material model for the elastomer (such as the neo-hookean model) and an elastic-plastic material model for the wire. This could allow to study various deformation modes (tension, bending, twisting).

- Study of the effect of incorporating two or more wires in the fiber, with and without radial symmetry.

- Study of the effect of changing the wire diameter and Young's Modulus

- Development of a wrap and coat technique to experimentally reach even smaller pitches. A core of elastomer could be wrapped with the metal helix (for example using the set up described in section 6.2.5). The wrapped fiber could then be converged into a tubular cladding, using either the same or a different elastomer.

The published version of this work can be found at [32].

# Chapter 6

# Functional fibers in textile manufacturing processes

In the previous two chapters, we designed two types of elastic fibers encompassing high conductivity metal electrodes. In order to use them in functional fabrics, we want to verify that these fibers can undergo traditional textile manufacturing processes, namely weaving and knitting. Greater emphasis is placed on knitting, as this technique entails more mechanical constraints on the fibers, but is also more versatile in terms of fabric mechanical properties and achievable functionalities.

## 6.1 Weaving

### 6.1.1 Introduction to the weaving process

Woven fabrics are composed of two perpendicular sets of threads interlaced together: the warp and weft threads. Warp yarns are held taut in the lengthwise direction. Weft yarns are in the crosswise direction. These are also called filling yarns are they are added layer by layer during weaving. Warp and weft threads can be either individual sections of yarn, of made of one continuous thread looping back and forth.

Woven structures vary in the pattern of the interlacing, the number of yarns per inch and the ratio of warp to weft yarn [93]. The structure directly impacts the

texture, the aspect and the mechanical properties of the fabrics [94]. For instance, in plain weave, yarns at right angles pass alternately over and under each other (Figure 6-1a). Alternatively, in a satin weave, each filling yarn floats over four warps and interlaces with the fifth warp yarn, with a lateral shift between each weft yarn. This patterns give satin fabrics their well-known softness to touch.

Woven fabrics are widely used (32% of apparel fabrics [95]), and have existed for thousands of years. Weaving is done on a machine called a loom. Although looms have undergone significant technological improvements, especially since the Industrial Revolution, the basic mechanism remains the same, including three main steps (Figure 6-1b):

1. Shedding: raising selected warp yarns using one or more heedles, to form a shed.
2. Picking: passing a shuttle through the shed to insert the filling.
3. Beating up: pushing the filling yarn into place in the fabric, against the previous yarns.

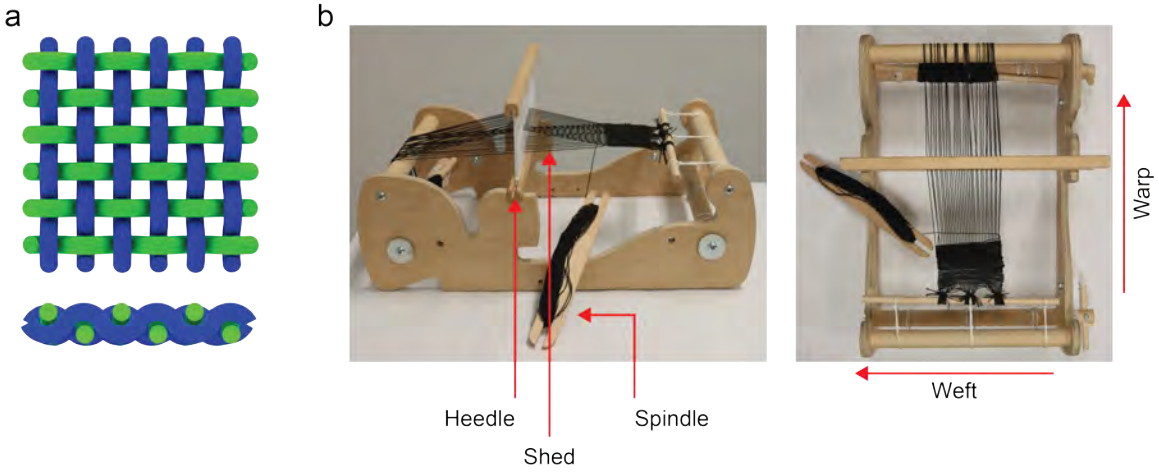


Figure 6-1: (**a**) Schematic of a plain weave fabric, top and side view. (**b**) Manual loom, side and top view.

Computers and electronics have allowed not only for faster production of woven fabrics, but also for more complex patterns, thanks to devices that control the position (raised or lowered) of the warp yarns, and for increased quality, thanks to the ability to separately and precisely control the tension in different yarns [93, 96, 97].

### 6.1.2 Mechanical constraints on yarns and fibers

Understanding the mechanical constraints that a yarn undergoes in a weave is key to designing weavable functional fibers. Studies of the weaving process have recently extended beyond the textile industry [97], into fields such as composite materials [13, 98] or soft robotics [99]. Although the complete description of the loads during weaving depends on the loom that is used, and is complex enough to be the object of a full study in itself, we summarize here the main aspects of it.

#### During weaving

A first set of loads is obviously applied during the weaving of the fabric itself. Warp and weft yarns play very different roles so it makes sense to look at them separately.

Warp: the warp must first withstand the primary **tension** [93, 97] that it is held with on the loom, as it is the basis for the fabric structure. In addition, every time the heedle is moved up or down during shedding, the tension in the warp yarns it holds increases, as they are held fixed at both ends and picked up vertically in the middle. Over the course of weaving a whole piece of fabric, this intermittent tension turns into **long-term cyclic loading** [100, 101].

Weft: there is no background tension on the weft yarn and the tension imparted by picking can easily be controlled and adapted to the type of yarn. Hence weft yarns are more often special-function yarns or fragile yarns [93].

For both the warp and weft yarn, two other types of constraints come into play. Because of the interlacing of threads, undergo high **bending**, with radii of curvatures on the order of the radius of the yarn [102] (figure 6-1a). Importantly, the degree of bending depends on the density of yarns and the weaving tension. In addition, during beat up, the different yarns slide against each other as they get packed. This can give rise to significant friction forces, depending of the yarns surface properties.

#### During fabric take-off

The fabric is taken off the tension of the loom usually at the end of the weaving process. Fundamentally, if the yarns were under tension, they were also experiencing some amount of strain. As a result, they will shrink after take-off [97, 103]. As the yarns crimp, an important question of yarn compatibility arises. Indeed, if some yarns shrink more than others, those that cannot shrink will create a prominence in the weave as they bend to accommodate the compression. We see here the importance of controlling tension during weaving to impose the same amount of relaxation. In particular, if a low modulus fiber is woven along a high modulus one, it is necessary to independently control the tension in each and lower the tension in the first one, to obtain the same final deformation. Still, the crimping due to shrinking of a weave can certainly be generated on purpose, to create structural effects.

### 6.1.3 Weaving of elastic functional fibers

As explained in the previous section, warp threads undergo numerous cycles of high tensile loading. Hence functional fibers are usually incorporated into fabrics as weft threads.

#### Non-elastic fibers

Several examples of non-elastic thermally drawn fibers, with PC or COC claddings, have been woven along with traditional materials such as cotton or polyester [24, 19]. When the tension during weaving is not properly monitored, dramatic failure can occur: when the fabrics shrinks, the fiber can undergo such compressive load that it buckles (Figure 6-2a-b). As a result, not only does it damages the fabric structure, but the fiber will also often deform plastically, and it can break of lose its functionality due to excessive bending. However, it is possible to control the tension well enough to allow for weaving. We noticed that, when the friction between the fiber and the yarns is low enough, the fiber can accommodate for the fabric shrinking by slipping against the other yarns and remaining straight, This results in loose loops of fibers

on the sides of the fabric (Figure 6-2c). Alternatively, functional fibers have been inserted within a double weave channel [18].


Figure 6-2: (**a**) Fabric deformation and (**b**) fiber buckling after weaving a PC fiber in a cotton fabric. (**c**) Loops of PC fibers at the end of a weave.

### Elastic fibers

Elastic fibers present the advantage that they can be woven under high tension, along with yarns that will have a large amount of shrinking after take-off. As an illustration of the benefit of our highly stretchable fibers, we wove them as weft thread, along with elastic yarn, to create plain weave elastic fabrics. The chosen yarn was a Latex/polyester blend yarn from Top Home, and we used a Cricket manual loom from Schacht Spindle. Images of the weaving process and of the final fabrics are displayed in figure 6-3. Weaving yarns with high elasticity is notoriously challenging, because of the amount of take-off shrinking. Both the fibers with buckled and helical electrodes shortened along with the elastic yarn, rather than protruding out of the fabric or even buckling akin to non-elastic fibers. In addition, we measured no change in the resistance of the electrodes before and after weaving. Hence our fibers can easily be woven into elastic fabrics and fully maintain their functionalities upon weaving.

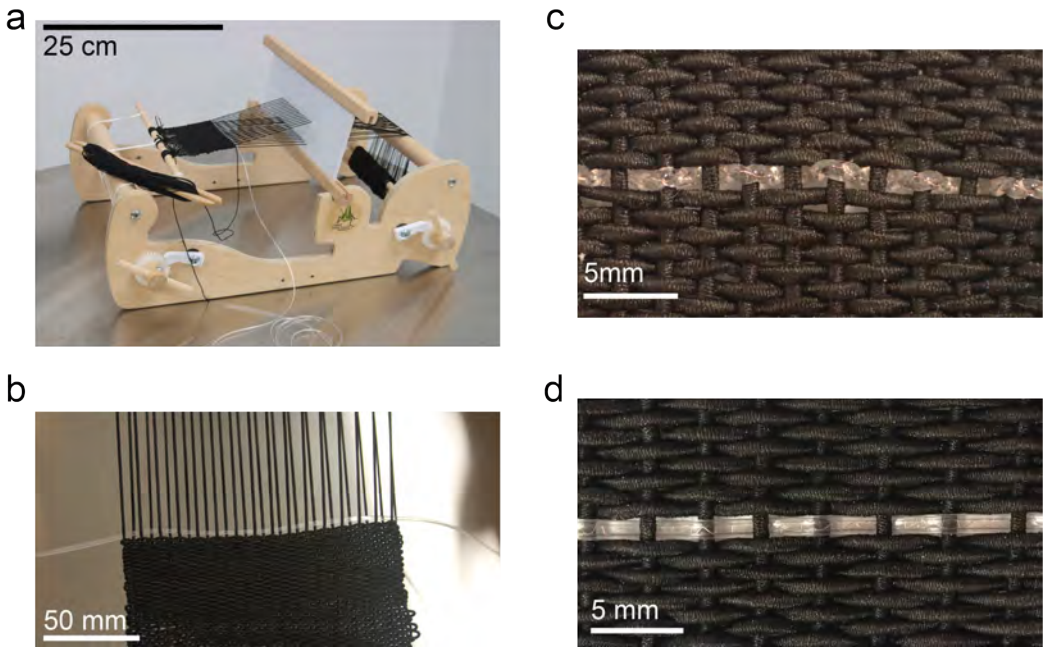


Figure 6-3: (**a-b**) Weaving of a fiber with a buckled electrode into an elastic fabric using a manual loom. (**c**) SEBS fiber with a helical copper electrode woven into an elastic fabric. (**d**) COCe fiber with a buckled copper electrode woven into an elastic fabric. The bulk yarn consists of an elastic blend of polyester and latex.

### 6.1.4 Elasticity arising from the fabric structure

Thanks to the curved path of the fibers in the weave, structural elasticity arising from the fabric itself is added to the elasticity of the fibers [94]. This phenomenon begets the shape of the J-shape load-strain curve of a woven fabric, when tensile loading is applied in the weft or warp direction. Figure 6-4a shows an example measurement, for tensile loading of a cotton plain weave in the warp direction. We can distinguish two regions of deformation: in the first region the crimped yarns straighten, in the second one tensile load is directly applied to the yarns so the force increases drastically. Chen et al. [12] have modelled this fabric-level structural elasticity by comparing the fabric strain to the yarn strain during tensile loading of the fabric. They show that for a plain weave for instance, the fabric can stretch by 30% with the yarns bearing only

5% strain. Moreover, woven fabrics can sustain large shear deformation, where the angle between warp and weft thread changes, with minimal material strain.

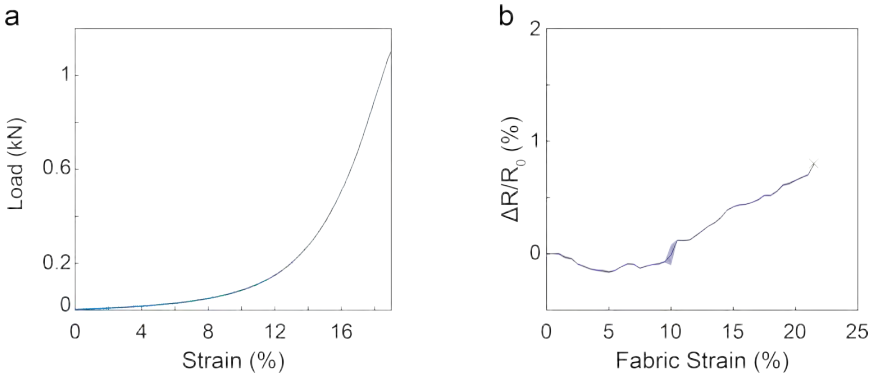


Figure 6-4: (**a**)Force versus strain for a plain weave cotton fabric, loaded in the warp direction. Note that, here, we report force instead of stress, because the area of a fabric is hard to define. (**b**) Change in resistance during tensile deformation of a SEBS fiber with a 50$\mu$m helical copper electrode ($\alpha_0 = 72°$), woven with elastic yarn into a plain weave structure. The last point on the graph (marked with an "x") represents loss of electrical contact.

This fabric elasticity is a valuable addition to the elasticity of our conductive fibers. One the one hand it widens the range of deformation that the fabric can endure, beyond that of the fiber itself. On the other hand, it can also serve as a buffer, and protect the integrity of the electrodes in case of exceptional strains. We demonstrated enhanced elasticity in elastic weaves containing fibers with buckled and helical electrodes, by measuring the electrode resistance during tensile testing in the direction of the conductive fiber (Figure 6-4b). A helical electrode with $\alpha_0 = 72°$, in a SEBS fiber inserted in the elastic weave, shows little change in resistance up to 10% fabric strain, while the predicted tensile yield of this fiber itself is $\sim 3\%$ according to our analysis in chapter 5.

### 6.1.5 Next steps

Our results from weaving elastic fibers with metal electrodes are an encouraging basis for further study (which is beyond the scope of this work). We demonstrated that the fibers sustain weaving in the weft direction, and that the woven structure grants enhanced elasticity. We think that future work should focus on two main aspects.

First, the fibers should be woven using and industrial loom, such as a Jacquard loom. This will require a more advanced study of the elongation of traditional yarns in the loom, to know the minimum required elasticity and the necessary weaving tension for a fiber woven along with these yarns. Weaving these fibers also as warp yarns would be an exciting challenge, and would allow designing more complex woven systems, leveraging the network structure of weft and warp.

Second, one should characterize how the addition of our fibers modifies the mechanical response of a weave. The size, modulus and density of the fibers are as many variables that expand the (already quite long) list of parameters that control a fabric properties (yarn size, spacing, material, weaving pattern,...). Both numerical and experimental study would bring precious insights for functional fabric design.

## 6.2 Knitting

### 6.2.1 Introduction to the knitting process

In knitted fabrics, a continuous length of yarn forms vertically intermeshed loops. Weft and warp directions (as defined in section 6.1.1) are also named course and wale direction. A course of knit refers to a horizontal row of adjacent loops. A wale of knit refers to a vertical column of interlaced loops , generally produced by the same needle in machine knitting (Figure 6-5).

Similar to weaving, there is a boundless variety of possible knitted structures, which will impact the texture, the aspect and the mechanical properties of the fabrics. Knits can notably be classified between two main types: weft or warp knits. In weft knitting, the path of the yarn is horizontal, along the course of the fabric, whereas, in warp knitting, the path of the yarn is along the wale of the fabric [96]. This work only focuses on weft knitting. Our goal is to understand the constraints acting on functional fibers while machine knitting, and to draw design principles to make these fibers compatible with knitting processes: we believe that the general principles derived in sections 6.2.5 and 6.2.6 are also valid for warp knitting.

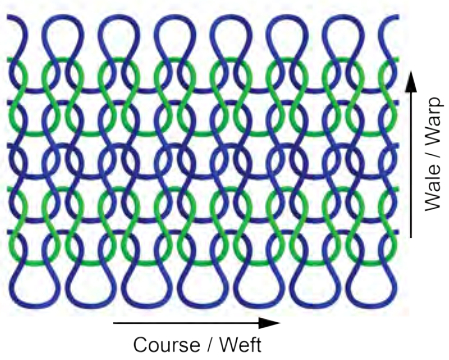


Figure 6-5: Example of a weft knitted fabric. Definition of course and wale directions.

Much more recent than weaves, knits have only been reported since the 11th century. Machine knitting didn't start until the Industrial Revolution. For any type of knitting machine, a hooked metal needle is the principal knitting element. Whether the needle is bearded or latched [104], and whether warp or weft knitting, the knitting action of a needle can be broken down into the same following steps, illustrated in figure 6-6:

1. The needle is in the rest position, with the previously formed loop ( "old" loop) held on its stem and covered by the hook.
2. The old loop is cleared from the needle hook by being pushed to a lower position on the needle stem.
3. The yarn is fed to the needle hook and formed into a "new" loop.
4. The hook is closed, enclosing the new loop and excluding the old loop, which remains on a lower position on the needle stem.
5. The new loop is drawn through the head of the old loop. Simultaneously the old loop slides off the closed hook of the needle and is cast-off.
6. The old loop now hangs from the feet of the fully formed new loop and the knitting cycle starts again

We hope that, at this point in the dissertation, the reader will notice a key feature of knits: **curvature**. So, by essence, knitted structures leverage structural elasticity into complex and rich mechanical properties, comprising but not restricted to high elasticity and anisotropy. In recent years, knitting, an old, "low-tech" discipline, has

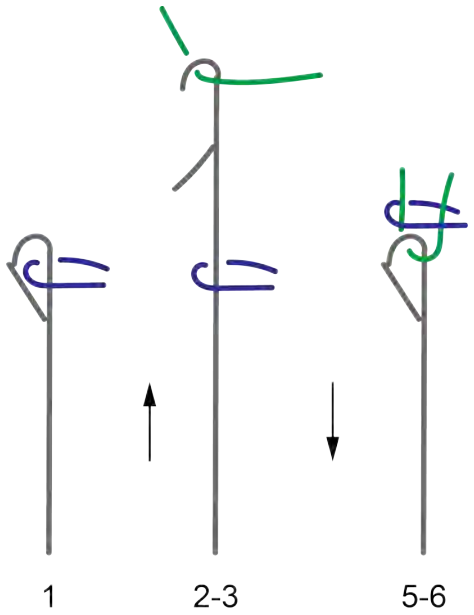


Figure 6-6: Formation of a stitch on a latched needle during weft knitting. Arrows indicate the movement of the needle. Numbers refer to the steps listed above. blue: old loop. green: new loop.

made a striking comeback into active research. Part of it derives from the surge of intelligent textiles, in particular in wearable electronics [3, 105, 106]. But the outstanding mechanical properties of knits, and the versatility of knitting also opened the door to various fields such as structural composites [107], stretchable electronics [57] or artificial muscles [99, 108]. However, one would notice that, when functional fibers are knitted, the fibers remain very simple, with at best two types of materials and simple architecture [57]. Knitting is a complex operation, and the fibers have to sustain various sets of loads and deformations across the steps listed above. Making multimaterial fibers that can survive this process is a real challenge. The constraints imposed on the yarns or fibers are even less well understood than in weaving [14, 109]. Hence most of our work in the next sections will consist in understanding them better, through experimentation, in order to make our fibers knittable.

### 6.2.2 Machine and settings

A single bed, Silver Reed SK280 knitting machine was used to make all samples. On the knitting machine, the yarn tension can be adjusted (not precisely, and not

monitored), in particular by setting the stitch size. As can be seen on figure 6-7, weights are attached to the bottom part of the fabric to hold the loops down on the needles and prevent the knitted fabric from coiling. They add tension to the old loop on the needle while knitting the new loop. They do play an important role, so it is necessary to record the weight (usually weight per needle) that was used as part of the knitting conditions.

Unless mentioned otherwise, the following knitting parameters were used:

- Stitch size 8 when knitting traditional yarns
- Stitch size 10 when knitting a conductive fiber
- Weights were removed when knitting a conductive fibers. Only two 10g weights were left at each extremity of the fabric, regardless of the number of needles used.

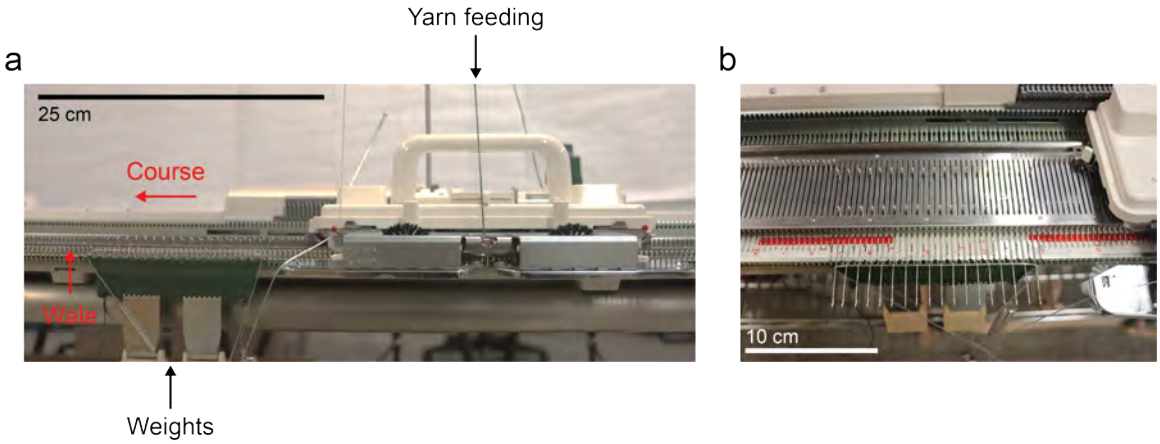


Figure 6-7: Knitting machine (**a**) Front view. (**b**) Top view. A COCe fiber is laid on the needles for knit-weaving.

The fibers were knitted along with three types of traditional yarns. For knit-weaving, a 100% wool yarn was used (JaggerSpun Maine Line 2/8 from Halcyon). For knitting, either a 100% cotton yarn (Pearl cotton 3/2 from Halcyon) or a 100% wool yarn was used (JaggerSpun Maine Line 3/8 from Halcyon).

### 6.2.3 Knit-weaving of fibers with buckled electrodes

In knit-weaving one yarn is knitted normally, creating the loops of the stitches, while a second yarn, here a fiber, is tucked into the stitches. For that, the fiber is laid down on the needle (Figure 6-8a). When the yarn feeder passes over them, it forms the loops of yarn while alternatively catching or leaving aside the fiber. The result is the same as if the fiber had been hand-sewn into the knitted fabric (Figure 6-8b).

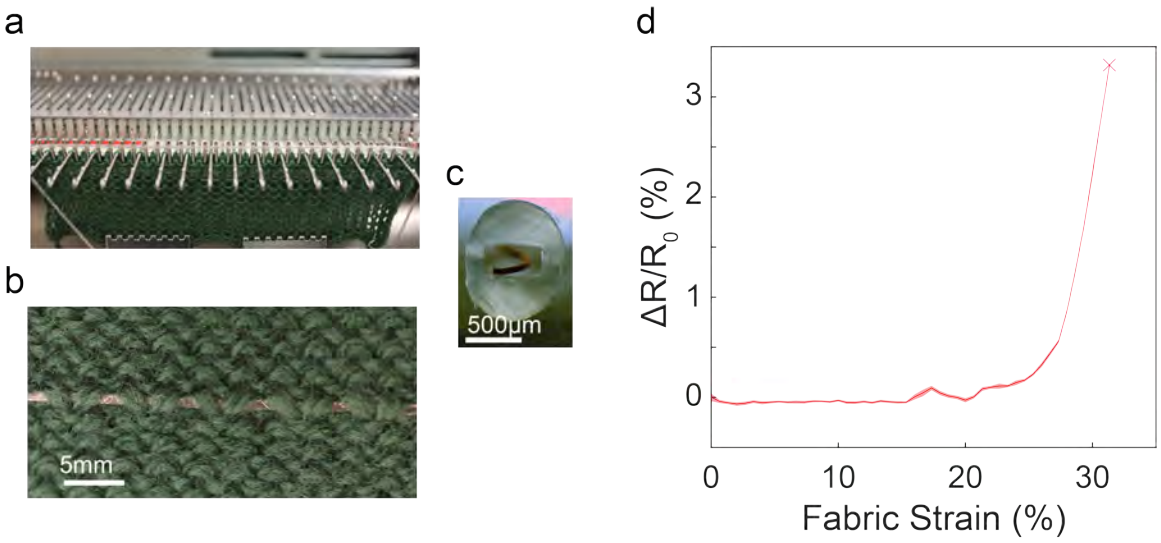


Figure 6-8: Knit-weaving. (**a**) Fiber laid on the needles for machine knitting. (**b**) COCe fiber with a 50$\mu$m buckled copper electrode ($\eta_{metal} = 25.1\%$) knit-woven with wool yarn into a knit. (**c**) Circular COCe fiber cross-section. (**d**) Change in resistance of the electrode during tensile deformation of the fabric pictured in (b). The last point on the graph (marked with an "x") represents loss of electrical contact.

The fibers with buckled electrodes were successfully knit-woven into a wool fabric. Here, the fibers were designed with a circular cladding cross-section around the rectangular channel, which made them easier to grab for the needles of the machine (Figure 6-8c). One can see from figure 6-8b that, in the knit-woven structure, the fiber remains straight. As a result, there is no enhancement of elasticity as found in the weave. Figure 6-8d shows the example of a buckled electrode fiber with $\eta_{metal} = 25.1\%$ in a knit. Upon elongation of the fabric along the course direction, i.e. the direction of the fiber, the resistance of the electrode is constant up to 25% fabric strain.

If knit-weaving enables facile incorporation of cylindrical stretchable functional

fibers into any knit, it is much less powerful than knitting the fiber itself. In particular, it loses the structural elasticity gained upon creating loops, which is one of the key advantages of knitting.

### 6.2.4 First attempts to knit fibers

The first, naive attempts to machine knit cylindrical fibers with buckled electrode had two outcomes: either the machine would jam, or the electrode would break in many points. This was true for any fiber diameter, and for any value of $\eta_{metal}$. Figure 6-9a shows the side picture of a fiber with $\eta_{metal} = 35\%$ after knitting. Even with such large elasticity we can see that the fiber broke in almost every stitch. We identified four characteristic of the fibers that could impact their knittability:

- Diameter - for reference, the hook of the knitting needle has a 1.6mm diameter
- Bending stiffness / Bendability
- Elasticity
- Surface properties

Here, by bendability, we refer to the bending angle that the fiber can undergo without any damage to the electrode.

We first eliminate what could be immediate and obvious causes of failure. First, we keep our fibers diameter below 1.25mm, as we notice that, above this diameter, the needles would not grab them properly. Small radius also avoid jamming of the knitting machine, but does not prevent electrodes from breaking.
Second, we test the bendability of the fibers as knitting imposes very high curvature on yarns. We find that the fibers can be fully folded (bending angle $\sim 180°$) without damaging the wire. This is a result of the mechanical decoupling between the cladding and the wire: even if the wire were to not be along the neutral axis of the fiber, it would experience very low strain because it bends independently from the cladding material.

We then compare the tensile behavior of our fibers and of the cotton yarn that they are knitted with (Figure 6-9b). We find that the elasticity of a fiber is much

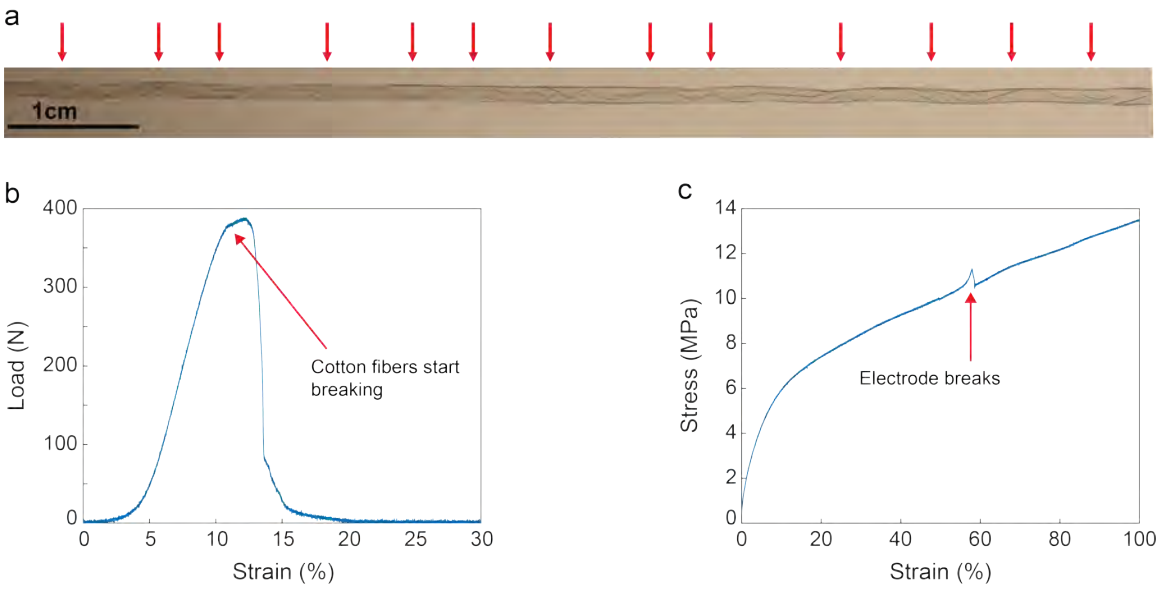


Figure 6-9: (**a**) Optical microscope picture of a COCe fiber with a 50$\mu$m buckled copper electrode ($\eta_{metal} = 35\%$). Red arrows mark the points where the electrode broke. (**b**)Tensile loading of the pearl cotton yarn used in knitting - again, load is reported instead of stress. (**c**) Tensile loading of a COCe fiber 50$\mu$m buckled copper electrode wrapped in polyester tex 35 ($\eta_{metal} = 61.1\%$).

larger than the strain to failure of a regular yarn used for knitting. Hence, if our fibers break during knitting, they must experience much larger strains than a regular yarn. To understand why, we come back to the mechanism of knitting described in section 6.2.1 and in figure 6-6. We notice that the yarn, or fiber, has to slide against the needle repeatedly. For example, between steps 1 and 2, the needle is pushed forward and the old loop has to slide against the needle stem, meanwhile opening the latch. We find slip to be a key requirement for knitting. When a loop has to slide along the stem of a needle, absence of slip would result in very large strains. In addition, slip is necessary to feed more length of fiber during the formation of a loop. If the fiber cannot move relative to the needle it will be stretched. As a result, we hypothesize that the main phenomenon that prevents knitting the fibers is the creation of fixation points between the fiber and the needles, generating excessive strains. We identify two types of mechanisms that can engender fixation points: friction and kinking. These two mechanisms are studied in the next two sections.

### 6.2.5 Friction

#### Friction Measurement

Measuring the friction coefficient of a yarn against a given material is a common procedure [110]. Figure 6-10a depicts the set up that we used. The yarn is wrapped around a cylinder of the material of interest (steel). One end of a yarn is loaded with a known tension $T_1$, usually by hanging a weight to that end. The other end is pulled (in our case using a capstan) at a constant speed $v_{capstan}$. A tension gauge measures the tension $T_2$ in the second strand of yarn. The coefficient of dynamic friction is given by:

$$\mu = \frac{1}{\gamma} \ln \frac{T_2}{T_1} \tag{6.1}$$

where $\gamma$ is the angle of contact between the rod and the yarn. $\mu$ varies depending on $v_{capstan}$, but here we are not interested in the specific value of $\mu$ but rather in comparing friction for different fibers and yarns. We use a 10g weight and a speed $v_{capstan} = 0.1$m/s. We used a steel rod with a diameter of 2.5cm, which is large enough to avoid kinking of the fiber.

When using our friction measurement set up with a round COCe fiber, we see an unexpected behavior: instead of measuring a constant tension $T_2$ that would let us calculate $\mu$, we see that the tension alternates between gradual increases and sharp drops (Figure 6-10b). This is typical of a stiction phenomenon, or stick-and-slip. When the fiber is not slipping, it is pulled by the capstan and elongates, hence the tension increases. Beyond a certain tension, the fiber suddenly jumps forward, and the tension drops. We understand that, during knitting, friction must generate fixation points between the fiber and the needles, which leads to strains beyond $\eta_{metal}$.

#### Surface treatment

Many options exist to reduce the friction between the fiber and the needle. We could for example coat the surface of the fiber with PTFE or oil, or modify its chemistry via plasma etching, functionalization... To make sure that the fibers would have similar surface properties as a yarn, we decide to use a similar material: we wrap

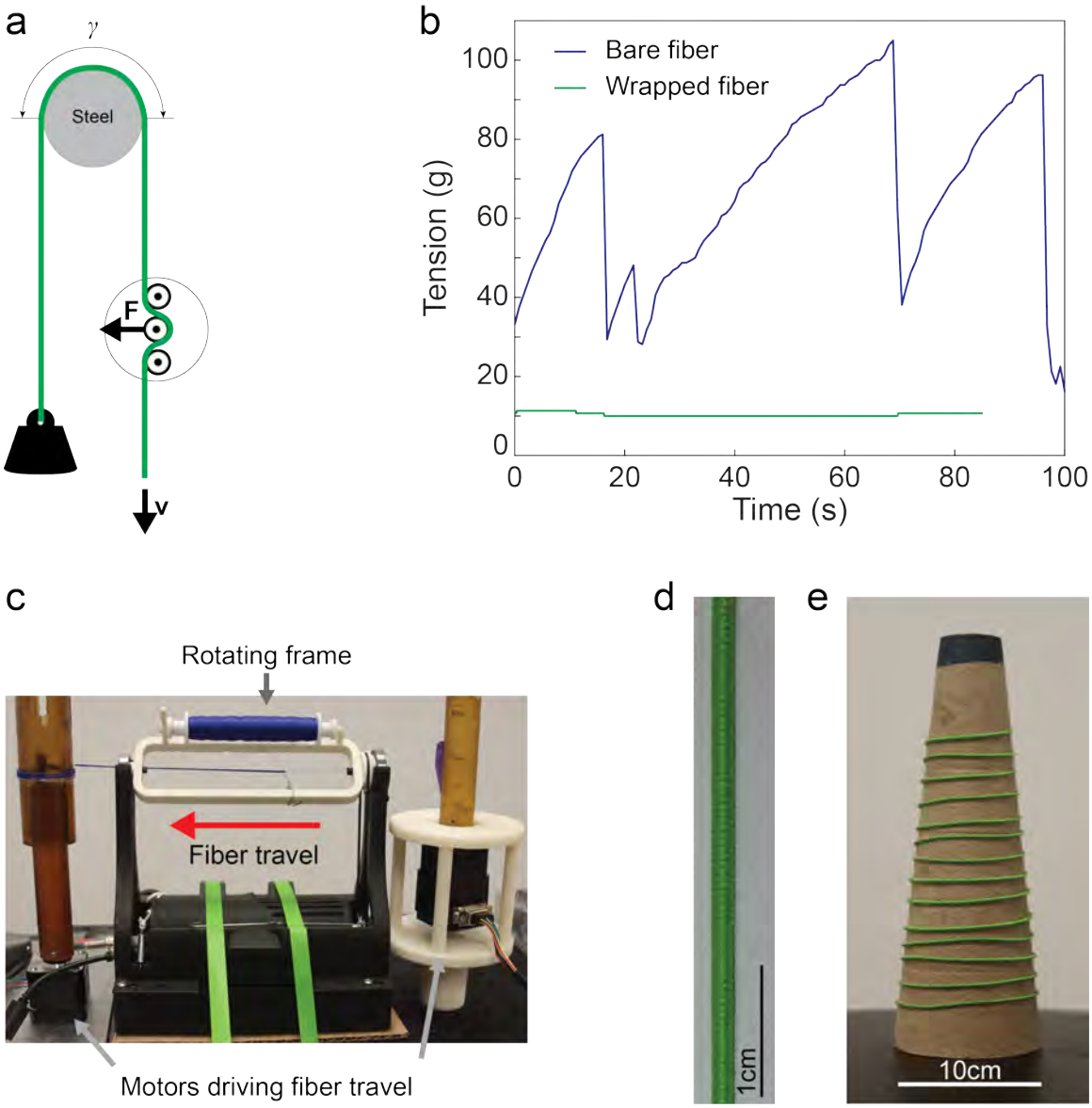


Figure 6-10: (**a**) Friction Measurement set up (**b**) Tension measured with the friction set up for a bare COCe fiber and the same fiber wrapped in tex 35 polyester. Weight: 10g. Speed: 0.1m/min (**c**) Fiber wrapping apparatus. (**d**,**e**) Pictures of the fibers wrapped in tex 35 polyester. (c) close up. (d) 2m on a knitting cone.

our fiber with a staple polyester thread. We fabricate a custom apparatus, showed in figure 6-10c, to make a tight and homogeneous wrap. Two motors (NEMA 17 stepper motors, LinEngineering) pull the fiber forward, with a constant travel speed, while a yarn spinner (EEW 6.0, Dreaming Robots) with a modified frame unspools and wraps the thread by rotating around the fiber. Using this set up, we were able to continuously cover meters of fibers in a tight and homogeneous wrap (Figure 6-

10d-e). Unless mentioned otherwise, the wrapping thread is a Gutermann Tera 100% polyester tex35 thread.

**Results**

We evaluate the surface properties of our wrapped fibers using the same friction measurement set up. Figure 6-10b compares the tension measured for a bare fiber and a wrapped fiber. We find that, with wrapping, the tension is drastically reduced and it remains constant: we eliminated stiction and reduced the friction between the fiber and the needles.

We tried to knit a selection of wrapped COCe fibers with various diameters and $\eta_{metal}$, along with cotton of wool yarn. Contrary to the bare fiber case, a fraction of the fibers remained conductive after knitting, showing the benefit of removing the fixation points due to friction. We now try to eliminate a second type of fixation points: these caused by kinking.

### 6.2.6 Kinking

Kinking is type of buckling instability, where the curvature of a bent member suddenly becomes discontinuous, creating a sharp angle. It is readily observed when bending a COCe fiber to an angle close to 180°.

In this section, we work with wrapped cylindrical COCe fibers that enclose a 40$\mu$m silver coated copper wire buckled in a circular channel. There are two main advantages to working with circular channels:

- When a wire buckles within a circular channel, it takes a helical shape [111, 112]. This three-dimensional buckling yields lower curvatures, which increases the lifetime of the electrodes (see section 4.5.1).
- A fiber with a circular channel has a radial symmetry. This simplifies our present analysis, as we will not worry about the specific direction of bending.

### Observation of the knitting mechanism

To get insights about kinking and its effects during knitting, we start by observing the shape of a fiber during the process. By measuring fibers resistance while knitting, we could see that, for more than 90% of the fibers that fail, the electrode broke during the first part of creating a stitch, when the hook of the needle pulls on the fiber to create a new loop, so we focus on this part of the knitting process. This is when the fiber has to be fed into the needles. To make our observations, we partially knit a row and unscrew the top part of the yarn feeder to be able to see the needles and the fiber. Two pictures in figure 6-11 compare the shape of the fiber at different stages of the needle movement, for a 0.7mm fiber and a 1.05mm fiber. We gather several important clues:

- The loops that are fully formed are kinked around their needle.
- For the larger fiber, kinking occurs at smaller displacement of the needle.
- The larger fiber bears a larger strain, which can be appreciated on the picture from the unravelling of the helical wrap.
- For all fibers, there seems to be more strain on the right side of the loop, which is the upstream side considering the knitting direction.

After repeated observations, we propose the simplified mechanism described in figure 6-12. Using the terminology described in the figure, if we focus on a specific loop, on the central needle, we see:

1. The central needle moves backwards, bending the fiber. Additional length of fiber is fed from the downstream side. The fiber is kinked around the upstream needle, creating a fixed point.
2. The fiber kinks around the central needle, creating a fixed point.
3. As the needle moves backwards, the upstream arm of the loop is stretched.
4. The fiber kinks around the downstream needle.
5. As the needle move backwards, both arms are stretched.

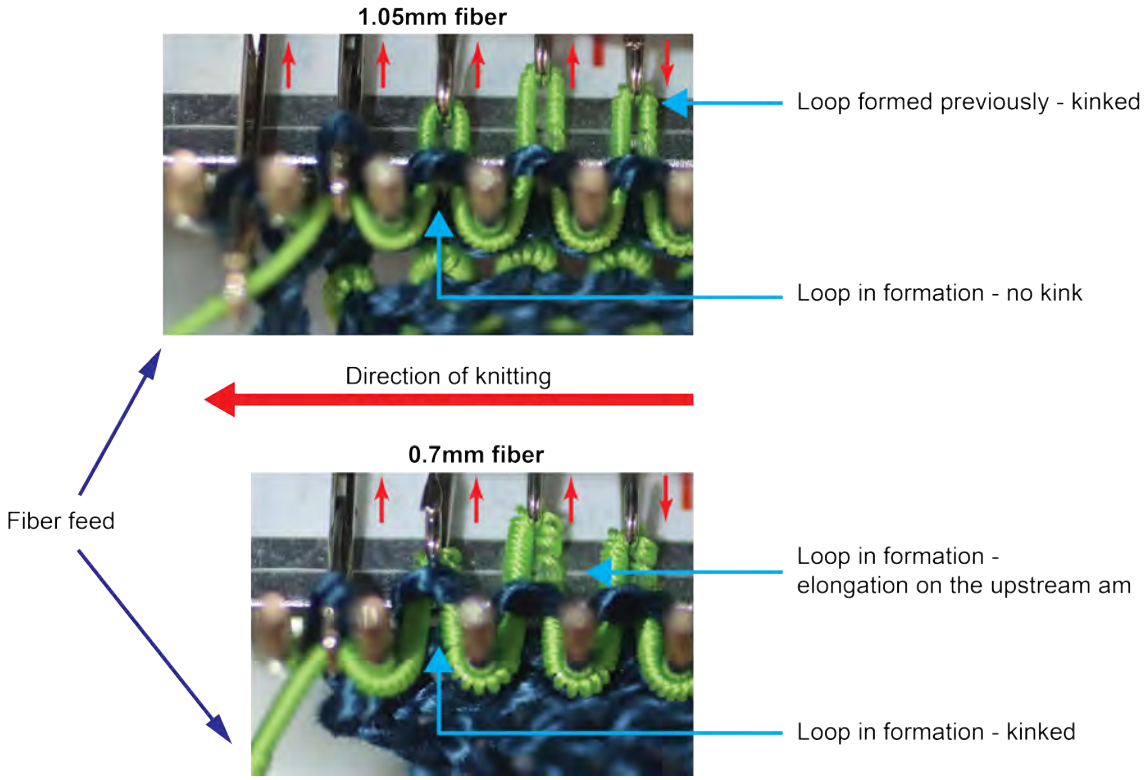


Figure 6-11: Observation of the knitting mechanism. Small red arrows indicate the movement of the needles.

If we know the displacement of the needle $\lambda_{kink}$ at which the fiber kinks, we can calculate the maximum strain imposed to the fiber. From the picture of figure 6-11 it seems like a reasonable approximation to say that the length of an arm of the loop is equal to the displacement of the needle. Hence we have for the strain:

$$\varepsilon_{knitting} = \frac{\lambda_{max}}{\lambda_{kink}} - 1 \tag{6.2}$$

with $\lambda_{max}$ the maximum displacement of the needle, equal to 8mm on this machine.

So, in order to knit our fibers without damaging the electrode, we need to delay kinking as much as possible, in order to increase $\lambda_{kink}$ and decrease the knitting strain.

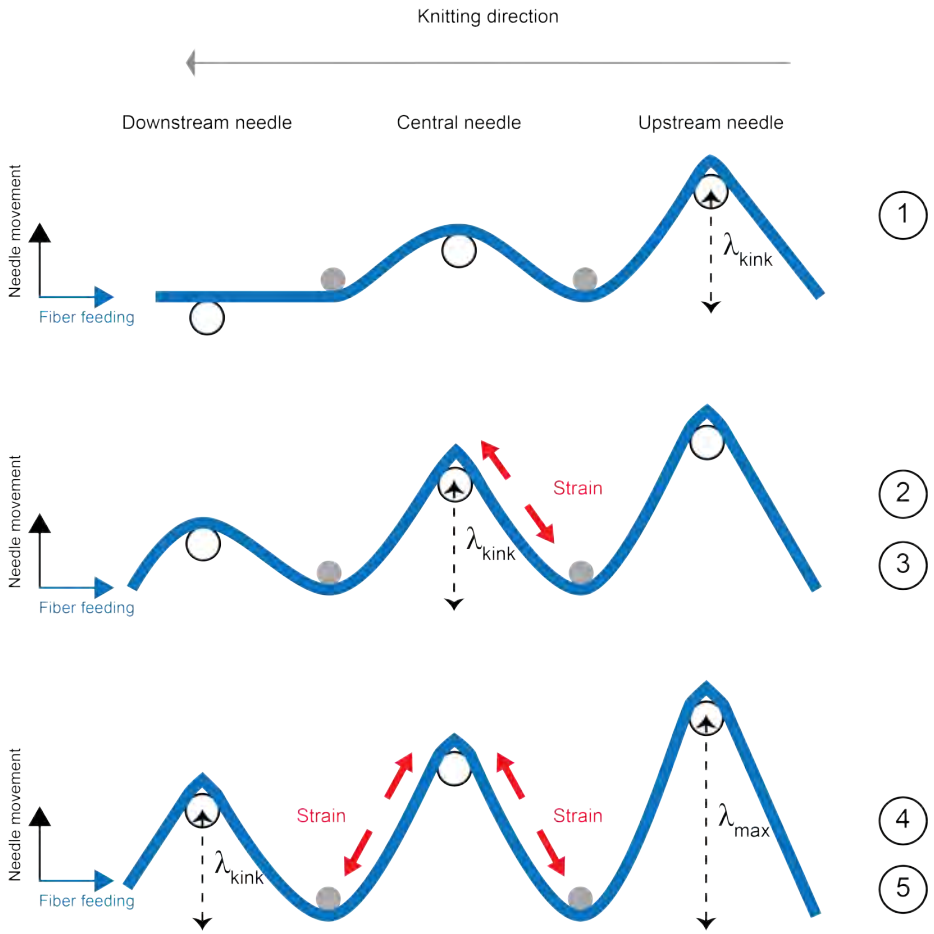


Figure 6-12: Simplified knitting mechanism. Note that we are focusing on the central loop so strains in the other loops are not labeled. Grey circles represent the poles between the needle. Figure not to scale.

### Kinking of a bent tube

Kinking of a thin tube under bending has been extensively studied. Brazier [113] first studied the ovalization of the cross-section of a thin cylinder under bending, called the Brazier effect. Many people then studied analytically and numerically how this ovalization practically reduces the bending stiffness of the tube and leads to buckling of the surface that is inside the bend [114, 115, 116, 117].

Here, we will rely on the analysis of Calladine in his book *Theory of shell structures* [118]. We will look at his derivation of kinking for an infinite tube under uniform bending and at how, in this case, the geometry of the tube (the fiber) affects the onset of kinking. We will then discuss the applicability of this model to our scenario,

and compare our experimental results with the trends found analytically.

Calladine first defines a flattening coefficient $\zeta$ as shown in figure 6-13. Taking $a$ as the initial radius of the tube, upon deformation, the radius in the vertical direction becomes

$$a_{defomed} = a \cdot (1 - \zeta) \tag{6.3}$$

Here we also define $\chi = t/a$ as the initial thickness to radius ratio of the tube (figure 6-13a). Using an energy method, Calladine calculates $\zeta$ depending on the curvature of the tube $\kappa$:

$$\zeta = (1 - \nu^2) \cdot \kappa^2 \cdot \frac{a^2}{\chi^2} \tag{6.4}$$

where $\nu$ is the Poisson's ratio of the material. Using the buckling stress of a tube under uniaxial compression, he finds that buckling, i.e. kinking, will always occur for the same value of $\zeta$ ($\zeta_{cr} \simeq 0.14$). Given equation 6.4, it means that:

- For a constant tube radius, a larger thickness to radius ratio leads to kinking at higher curvature ("later" kinking).
- For a constant thickness to radius ratio, a larger radius leads to kinking at lower curvature ("earlier" kinking).

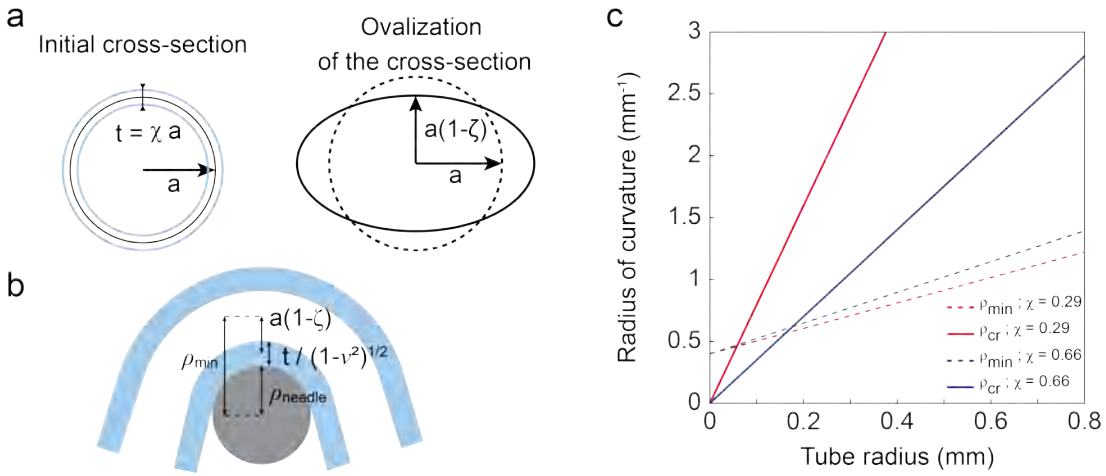


Figure 6-13: (**a**) Sketches of a fiber cross-section defining $\zeta$ and $\chi$. (**b**) Sketch of a fiber wrapped around the knitting needle, defining $\rho_{min}$. (**c**)Comparison of $\rho_{min}$ and $\rho_{cr}$ depending on $a$, for the two extreme experimental values of $\chi$. Beyond the crossing point, $\rho_{cr} > \rho_{min}$, so kinking occurs before the fiber wraps around the needle.

Now we need to verify if this model applies to our scenario. In our experiments, the range of the parameters $a$ and $\chi$ are $0.26mm < a < 0.55mm$ and $0.29 < \chi < 0.660$.

First we check if the long tube approximation holds in our case. Calladine defines a parameter $\Omega$ such that

$$\Omega^2 = \frac{L^2\chi}{a^2\sqrt{1-\nu^2}} \tag{6.5}$$

and he determines that the infinite tube approximation holds for $\Omega^2 > 3.5$. Let us make a conservative estimation by taking a minimum $L = 4$mm (distance between two poles of the machine), $\chi = 0.29$ and $a = 0.55$mm. We keep $\nu = 0.5$ as a good approximation for an elastomer. With these values, we obtain a minimal value of $\Omega^2 = 17.7$, showing that the long tube approximation holds. Further along his derivation, Calladine also assumes that $L/a > 3$, which is also true for our fibers.

Second, if the fiber bends to a radius of curvature smaller than some minimum radius, then the fiber is actually wrapped around the needle and the pure bending approximation cannot hold. According to figure 6-13b, the minimum radius of curvature will be:

$$\rho_{min} = \rho_{needle} + a(1 - \zeta_{cr} + \frac{\chi}{2\sqrt{1-\nu^2}}) \tag{6.6}$$

Using equation 6.4, we calculate the radius of curvature for kinking, $\rho_{cr} = \frac{1}{\kappa_{cr}}$, and we compare $\rho_{cr}$ and $\rho_{min}$. Figure 6-13c shows that, for our range of parameters $a$ and $\chi$, kinking should happen before the fibers wraps around the needle.

Third, we have to consider tension. Our fiber undergoes some tension, which contradicts the pure bending approximation. When tension cannot be neglected, it will have two conflicting effects. On the one hand, tension during bending tends to increase the curvature for a given needle displacement, which would lead to faster kinking. On the other hand, tension adds an extensional stress in the tube, which should delay kinking. We did not theoretically derive the effect of tension, but qualitatively appreciated it: the same fiber, which could be knitted successfully at minimal tension (controlled by the yarn feeder) would fail at higher tension. Hence we think that tension favors kinking or some other mechanism that leads to fixation points during knitting.

We ran a series of measurement to appreciate the effect of the fiber geometry on kinking. In order to remain as close as possible to a pure bending scenario, we let the fiber loose during knitting instead of having it through the whole yarn feeder, to approach zero tension. We prepared a batch of fibers with a constant $\chi = 0.46$ and various values of $a$. For each value of $a$ we prepared several samples with several values for $\eta_{metal}$. We then knitted all the samples and verified if the electrode was intact by measuring its resistance. The results of this experiment are presented in figure 6-14. We find that the minimum required elasticity for successful knitting, marked as a dashed line on the figure, varies linearly with $a$. It means that, according to equation 6.2, the displacement of the needle at which kinking occurs, $\lambda_{kink}$, is inversely proportional to $a$. Considering that the curvature of the fiber increases with the displacement of the needle, this result is consistent with our analytical prediction, that a smaller radius $a$ would delay kinking. At this stage, it would be useful to confirm this consistency by running the same set of measurements with a constant $a$ and various values for $\chi$.

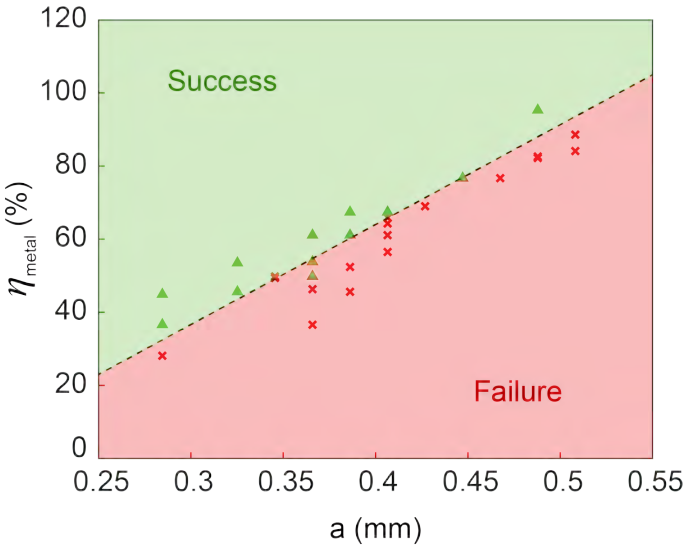


Figure 6-14: Outcome of knitting depending on fibers radius and elasticity

Having assessed that we can knit our functional fibers, we now take a look at the tensile properties of a fabric containing these.

### 6.2.7 Tensile properties of fabrics containing thermally drawn fibers

To evaluate the effect of the functional fibers on a fabric mechanical properties, we need to define a filling ratio quantifying the proportion of fibers in the fabric. As we are weft knitting, a fiber runs across a row of stitches, so we can define the filling factor as

$$\varphi = \frac{number\ of\ rows\ knitted\ with\ a\ fiber}{total\ number\ of\ rows} \tag{6.7}$$

We measure the response of various samples under tensile loading in the wale and course direction. The results are reported in figure 6-15 and 6-16. We note that, for tensile testing of fabric samples, if the same types of yarn and stitch are used, it is custom to not report stress, because the sample area is not well defined, but rather to report the force per stitch or row, depending on the direction of loading. We first observe that our samples present the same anisotropy as traditionally reported for weft knitted fabrics [119, 120]: for the same elongation, the force in the course direction is much lower than the force in the wale direction. However, a surprising result is that the effect of increasing $\varphi$ is opposite depending on the direction of loading. For walewise loading, increasing $\varphi$ leads to a decrease in the load, a "softer" fabric. For coursewise loading, an increase in $\varphi$ results in a higher load, a "stiffer" fabric.

This effect can be explain when looking at the mode of deformation of the stitches, under wale or course loading, a question which has been studied both theoretically [121, 122] and experimentally [123]. In a first stage of deformation, the yarn deforms almost exclusively in bending and, as the loops change shape, the contact points between two stitches move. Under wale loading, a jamming effect will quickly occur: the columns of stitches, or wales, become packed together as the fabric shrinks in the course direction. This phenomenon is visible in figure 6-15a, for a knit under 50% strain, while the same fabric with 50% elongation in the course direction shows no jamming of the rows. Jamming might eventually occur, but at much higher strains. Hence, in wale loading, the mode of deformation of the yarn quickly changes: as the

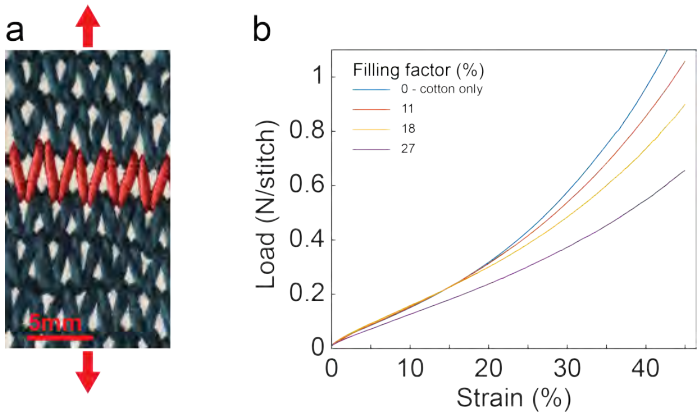


Figure 6-15: Wale loading of knitted fabrics. (**a**) Picture of a fabric under 50% tensile loading in the wale direction. (**b**) Change in the mechanical response of the fabric depending on the filling factor $\varphi$. The fiber is a COCe fiber ($a = 0.36$mm, $\chi = 0.46$) with 50$\mu$m copper wire. All samples were made of the same 100% cotton yarn.

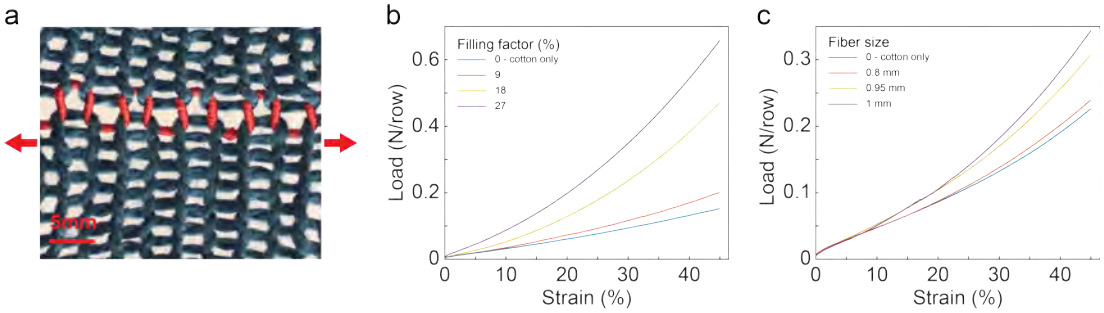


Figure 6-16: Course loading of knitted fabrics. (**a**) Picture of a fabric under 50% tensile loading in the course direction. (**b**) Change in the mechanical response of the fabric depending on the filling factor $\varphi$. The fiber is a COCe fiber ($a = 0.36$mm, $\chi = 0.46$) with 50$\mu$m copper wire.(**c**) Change in the mechanical response of the fabric depending on the radius $a$ of the fiber. The fibers are COCe fibers ($\chi = 0.46$) with 50$\mu$m copper wire. The different samples have the same filling ration $\varphi = 9\%$. All samples were made of the same 100% cotton yarn.

wales are packed, there is no possibility for yarn bending, and the yarn undergoes straight tensile loading. From figure 6-9, we know that the fiber has a much lower tensile modulus than the cotton yarn. However, because the yarn is a multifilament staple yarn, its bending stiffness is orders of magnitude lower than that of the fiber. Hence, this switch in deformation mode explains the opposite effect of $\varphi$ in course and wale loading. Furthermore, one can note from figure 6-15, that the effect of $\varphi$ starts to be noticeable around 15% strain. This lets us think that this is when jamming of the wales occurs.

Additionally, figure 6-16 lets us see that, for a given value of $\varphi$, increasing the fiber diameter yields a higher load. This is a coherent result, considering that the bending stiffness of a fiber scales as $a^4$.

### 6.2.8 Discussion and Next steps

In the previous sections we have:

- Identified fixation points as a failure mechanism for knitting fibers
- Identified friction and kinking as two possible mechanisms for the formation of fixation points
- Proposed a wrapping method to reduce friction
- Proposed a sequential mechanism describing how the fiber deforms, kinks and elongates during knitting
- Proposed an analytical model for kinking of a tubular fiber, which gives some design rules for the fiber geometry, and we have assessed the validity of the model.
- Evaluated the impact of incorporating functional fibers on the tensile properties of a knit.

In terms of design rules for fibers that can be knitted, and knitting conditions, we draw the following conclusions:

- The friction between the surface of the fiber and the needles/poles must be minimized, which can readily be done by wrapping the fiber with sewing thread.
- The knitting tension should be as low as possible
- Kinking of the fiber should be delayed as much as possible to avoid excessive strains. For tubular fibers, one can use two geometric knobs: increase the thickness-to-radius ratio of the fiber, or decrease the radius of the fiber.

Our understanding of the knitting process has allowed for the first ever successful knitting of thermally drawn functional fiber. More work could be done to prefect this understanding, in particular by studying other possible fixation points that we

did not focus on, for instance these that could form around the poles of the machine. Additionally, the study of kinking should be extended to fibers with different cross-sections, in particular fibers with a rectangular channel. Further down the road, our design principles could be applied to different types of knitting, such as double-bed knitting or warp knitting. This requires to understand the differences in mechanical constraints between different types of knitting, to modify the study accordingly. We believe that the principles derived here will still apply.

# Chapter 7

# Towards fabric systems

## 7.1 Integrating micro-devices into elastic fibers

To demonstrate the application of stretchable solid metal electrodes in a textile, we employed the buckled electrodes as interconnects for micro devices embedded within elastomer fibers. We start here with microscale light-emitting diodes ($\mu$LEDs) as a model. Micro devices were previously integrated within fibers by placing them into a channel within the preform and converging metal wires such that, during the draw, they cut through the polymer to connect to the pads of each device [24]. Here we pursue an alternative strategy to fabricate $\mu$LED-containing elastomer fibers.

### 7.1.1 Fiber fabrication

#### Devices connection

We first assemble a chain of $\mu$LEDs connected by a copper wire, and then converge this entire chain into a channel within the elastomer fiber during drawing. Green InGaN/ GaN LEDs (Genesis Photonics) were used as the micro-devices. To make the daisy chain in series, the LEDs were connected to a 40$\mu$m silver coated copper wire (Elektrisola 46 AWG) using solder paste (ChipQuick, Sn42/Bi57.6/Ag0.4).

By connecting the devices to two insulated wires, and buckling them into a single channel, the $\mu$LEDs can be mounted in parallel inside the fiber. To connect devices in

parallel, the $\mu$LEDs were connected to two 50$\mu$m enameled copper wires (Remington Industries 44SNSP 44 AWG Magnet Wire) using either silver epoxy (EpoTek H20E) or solder. During connection, the electrodes must first be scratched locally (here using a razor blade) to expose the copper. They are then laid down on the devices, with the exposed section of wire aligned with the connection pads, and a droplet of silver epoxy or solder is deposited to make the connection. With silver epoxy, the bond is then cured in an oven at 100°C overnight. With solder, we create the connection by approaching the hot tip of a soldering iron. Devices requiring as many as four electrodes were successfully connected and drawn into fibers.

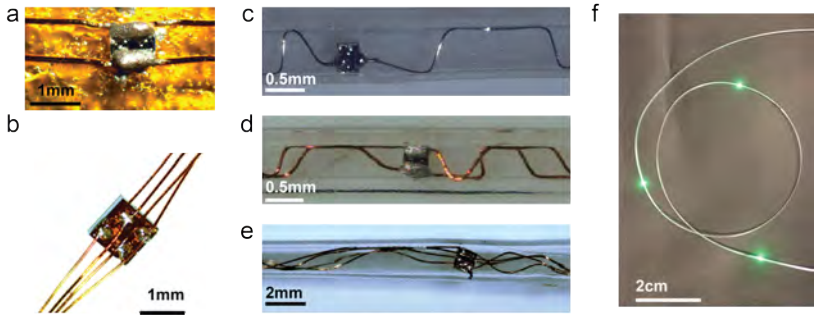


Figure 7-1: (**a**) $\mu$LED connected in parallel to two insulated 50$\mu$m copper wire using silver epoxy. (b) I2C temperature sensor connected to four 50$\mu$m enameled copper wire using solder. (c) COCe $\mu$LED-fiber showing a $\mu$LED connected in series and one buckled electrode ($\eta_{metal} = 20\%$). (d) COCe $\mu$LED-fiber with the $\mu$LED from (a) ($\eta_{metal} = 20\%$). (e) COCe fiber comprising the I2C sensor from (b) ($\eta_{metal} = 11\%$). In (c-e) the electrodes were buckled after the draw. (f) A photograph of a $\mu$LED-fiber with 3 devices connected in series.

### Fiber drawing

The daisy chain was then drawn in a simple COCe preform that has a rectangular channel, just like in chapter 4. Depending on the dimensions of the final channel containing the $\mu$LEDs in relation to the devices themselves, two regimes emerge for producing elastomer fibers.

If the final channel is smaller than the $\mu$LEDs, then each device becomes a pinning point between the wire and the cladding during the draw. As explained in appendix A, without these pinning points, the solid fiber is elongated in the bottom part of

the draw, below the furnace. This elongation is enough to yield some buckling when the fiber relaxes after the capstan. Here, after a $\mu$LED has been pinned, the strain in the cladding above it increases until a second $\mu$LED converges into the fiber, creates a fixed point, and prevents further elongation because of the straight copper wire connecting the two $\mu$LEDs. Figure 7-2a depicts this mechanism. Increasing the distance between the $\mu$LEDs then leads to higher cladding strains during the draw ($\varepsilon_{clad}$), and hence larger $\eta_{metal}$. Appendix A discusses the ways to increase the cladding strain during the draw. By drawing COCe at its lowest draw temperature (140°C, drawing at 3m/min), a 2% induced elasticity could be achieved in the final $\mu$LED-containing fibers (Figure 7-2b).

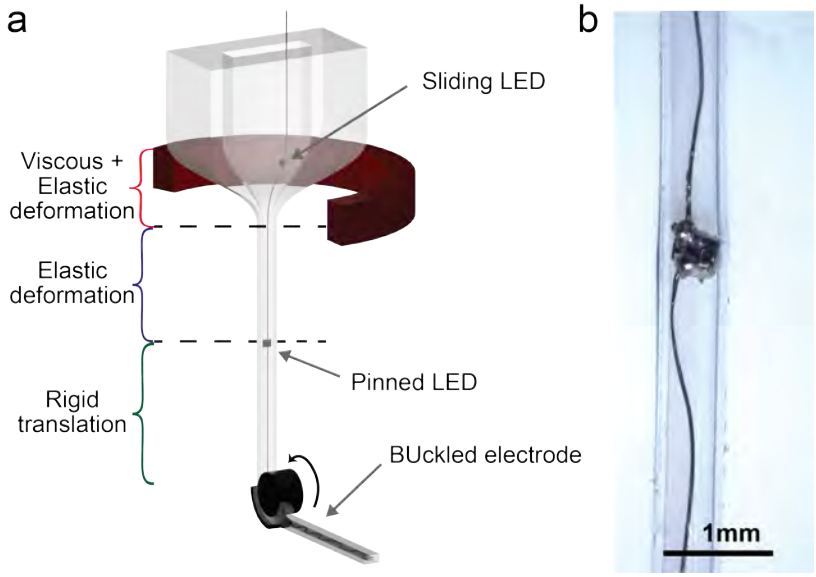


Figure 7-2: (**a**) Modes of deformation of the cladding along the draw, when a device is pinned. (**b**) $\mu$LED pinned in a COCe cladding. $\eta_{metal} = 2\%$ elasticity was built-in during the draw itself.

To reach larger strains, we explore a second regime, when the final dimensions of the channel are larger than the $\mu$LEDs, and the devices are able to slide with respect to the polymer cladding following the draw. This yields a higher strain in the cladding during the draw, but more importantly, additional buckling can be provoked after the draw. When the polymer is stretched, the devices can be pinned by heating and compressing the cladding to create fixed points during release. The electrodes connecting the $\mu$LEDs then buckle as described in chapter 4. We created $\mu$LED-fibers

capable of withstanding strains up to 20%.

### 7.1.2 Fiber testing

In these $\mu$LED-fibers tensile deformation does not influence optoelectronic performance, as revealed by their light current-voltage characteristics with and without strain in figure 7-3.

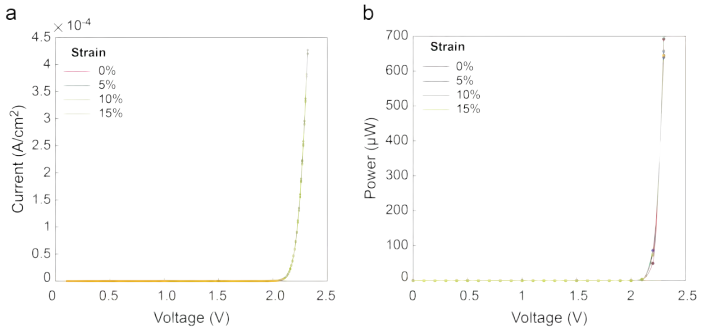


Figure 7-3: Light-Intensity-Voltage characterization of the $\mu$LED-fibers under different amount of axial strain. In-series $\mu$LED-fiber with a buckled 40$\mu$m silver-coated copper electrode, $\eta_{metal} = 19.4\%$. (**a**) Electrical current against voltage. (**b**) Optical power against voltage.

We incorporated these $\mu$LED-fibers into electronic textiles, first by sewing them into a finger of a knitted glove (Figure 7-4a). When the forefinger is bent, the fiber undergoes 10% of strain, and the $\mu$LEDs maintain their operation and electrical connectivity.

In addition, $\mu$LED-fibers with a circular cross-section were knit-woven into a cotton sleeve using our knitting machine (Figure 7-4b-c).The fibers showed no difference in performance before and after knit-weaving. Furthermore, they maintained their electrical connectivity under multiaxial stretching, bending and twisting of the fabric.

In this section, we presented a novel method to connect and draw micro-devices connected with buckled electrodes into fibers. In the next sections, we present two applications that leverage this process to design fabric systems.

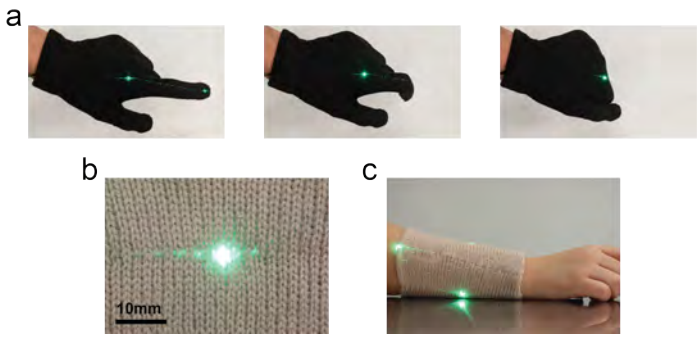


Figure 7-4: (**a**) $\mu$LED-fibers woven in a knitted glove: the bending of the forefinger leads to a tensile strain of about 10% in the fiber. (**b-c**) A $\mu$LED-fiber comprising four devices connected in parallel, knit-woven into a cotton sleeve.

## 7.2 Woven optical antenna for LiFi communication

### 7.2.1 Background

The term LiFi refers to high speed wireless communication between devices, through light. In LiFi, information is carried through the variations in amplitude of a light source, which could be in the infrared, visible or ultraviolet range. Communication through light not only enables faster data transmission than radio frequency communication (such as Wifi), but is also promising for areas that are susceptible to electromagnetic interference, such as aircraft cabins, hospitals or in the military. It is also appropriate for communication on a shorter distance, as light cannot penetrate through walls or similar object. As a result, LiFi is foreseen mostly for indoor use. In that context, emitters and receptors in a textile form would be of particular interest. They can easily cover large areas while being invisible parts of daily objects such as curtains, carpets, sofas...

### 7.2.2 Fiber-to-fiber communication

To make a fabric LiFi antenna, we used reverse-biased $\mu$LEDs in fibers as photodetectors, to receive high-speed data through light.

Fiber-to-fiber communication was first tested with two identical fibers containing green InGaN/GaN $\mu$LEDs (wavelength 525nm). Diodes in the emitting fiber were

driven with a voltage between 2.3-2.5V. The light-detecting fiber was connected to a custom circuit and the $\mu$LEDs were operated in reverse-bias (+2.5V from cathode to anode), allowing the semiconductor devices to be operated as photodiodes. The circuit comprised of a single-stage transimpedance amplifier with a high-pass filter, and the output of the circuit was connected to an oscilloscope.

It was found that the receiving fiber could detect sinusoidal modulations of light intensity at strains of up to 20%, with a measured responsivity of 125nA/W (Figure 7-5), thus confirming the possible use of our fibers for LiF applications.

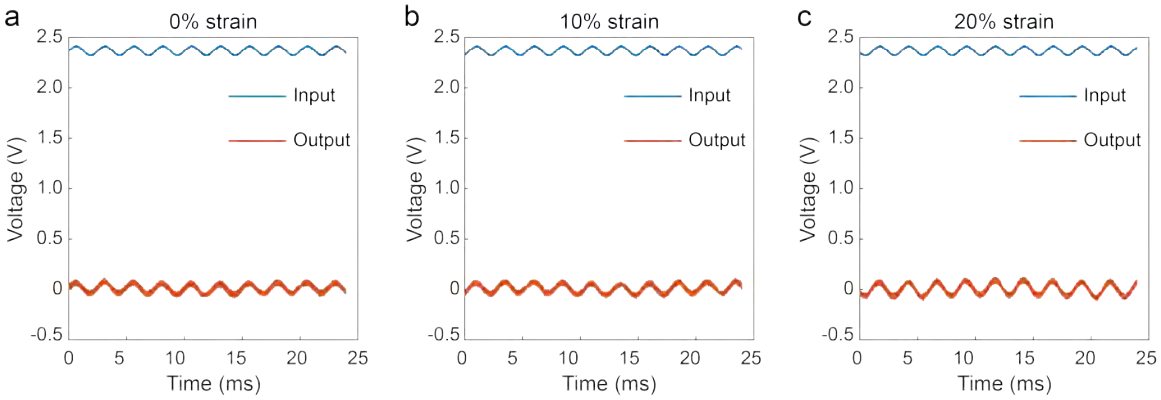


Figure 7-5: Transmission of a 400Hz sinusoidal wave between two $\mu$LED-fibers (not in fabric). The emitting diode is driven with a 2.4V voltage which is modulated by a sinusoidal signal of 100 mV in amplitude (Input in the figure). The receiving diode is reverse biased with 2.5V. The output in the figure is the voltage recorded after amplification and conversion of the photocurrent. (**a**) 0% strain (**b**) 10% strain (**c**) 20% strain

### 7.2.3 Weaving of a fabric antenna

By weaving the $\mu$LED-fibers into elastic fabrics, we design soft and stretchable optical antennas. Eight $\mu$LED-fiber strands with a total of 16 devices were woven into an omnidirectional football-shaped elastic optical antenna, shown in figure 7-6.

The football was woven as four independent oval pieces, using a plain weave pattern. Then the pieces were sewn together to create the football shape. The bulk of the weave was made of a latex/polyester blend yarn, like the one used in section 6.1.3. The fabric of the antenna can be stretched by 13%, by inflating a balloon inside

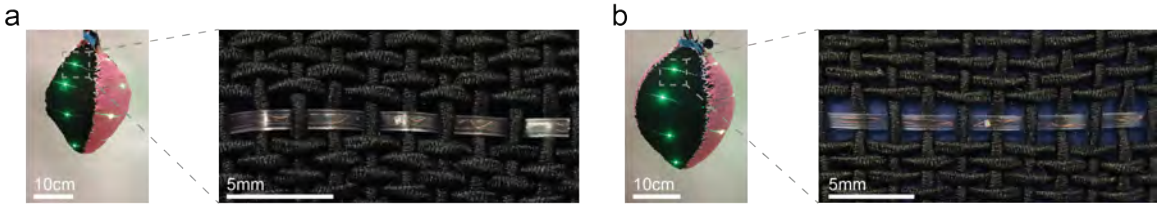


Figure 7-6: Photographs of a fabric football optical antenna in the relaxed (**a**) and inflated (radius increase by 13%) conditions (**b**)

the football, without disrupting the operation of the antenna (Figure 7-6 and 7-8). During the inflation, the fibers experience tensile strain and the insulated electrodes connecting the $\mu$LEDs straighten within their channels. Finally, the devices are regularly distributed around the three-dimensional surface of the football shape, to enable signal reception from various angles.

### 7.2.4 Characterization

As an example of LiFi data transmission, an acoustic signal is transmitted from a flashlight to the antenna. The testing set up is depicted in figure 7-7. The signal, received by a microphone, is used to modulate the light intensity of a flashlight. A piezoelectric microphone and an amplifying circuit were mounted at the back of the flashlight to pick up sound and modulate the light intensity with the resulting current. The $\mu$LEDs in the fabric antenna detect the variations in light intensity as deviations in a photocurrent, which is then converted into a voltage, using the same circuit as in section 7.2.2. The voltage is transmitted to a speaker and an oscilloscope.

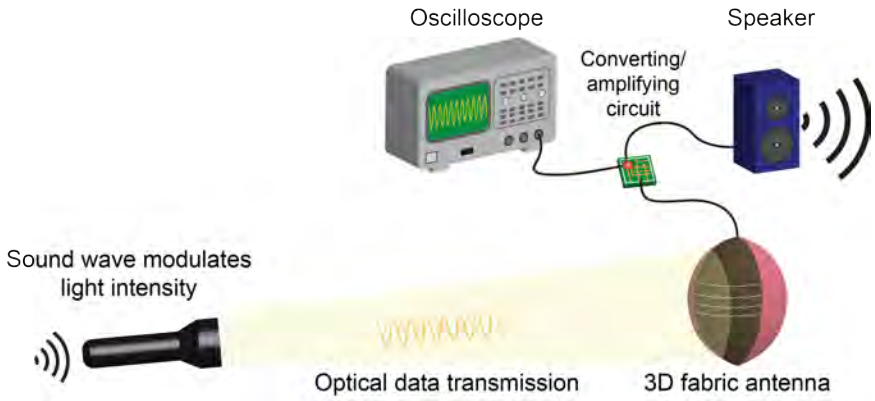


Figure 7-7: Testing set up for the optical fabric antenna

We find that at fabric strains of up to 15%, the $\mu$LEDs within the fabric antennas can faithfully detect complex LiFi signals. This is shown by the undeformed shape of the signals in figure 7-8 but even more so by the Fourier transform of these signals. Thanks to its three-dimensional shape, and thanks to the repartition of the $\mu$LEDs, our football antenna can receive signal from almost any direction: 360° horizontally and ±70° vertically. It also works for light sources placed at various distances, from 5cm to 2m in our experiments.

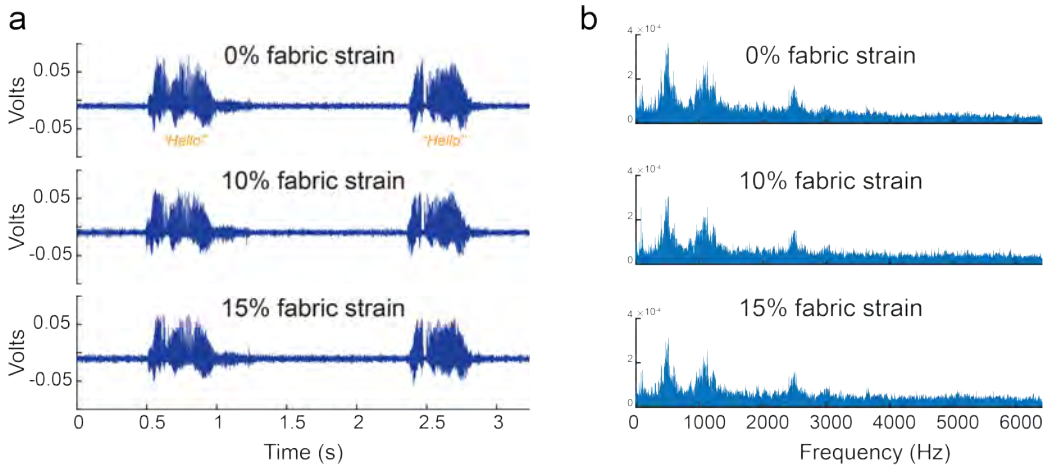


Figure 7-8: (**a**) Signal received by a reverse-biased $\mu$LED with a COCe fiber woven into an elastic plain weave ($\eta_{metal} = 15\%$). The source signal is a light source with amplitude modulated by an audio signal (recording of a voice saying "Hello" twice). Stretching the fabric does not modify the signal received by the fabric antenna. (**b**) Fast Fourier transform of the signals in (a), showing minimal distortion of the signal with strain.

These woven optical antennas prove to be stretchable, conformable, and given the scalability of textile manufacturing, can be designed to cover large areas.

## 7.3 Knitted temperature sensing fabric

### 7.3.1 Background

Physiological temperature carries a variety of information, from health to emotions. Skin temperature varies both spatially and temporally. The ability to rapidly and accurately detect localized changes in skin temperature, for example through a sensing

garment, has many applications. For instance, among diabetic patients, temperature monitoring on the sole of the feet has been shown to allow for early detection of inflammation, which can help avoid ulceration [124, 125]. Another possible application is frostbite prevention in extreme environments. Skin temperature monitoring has seen a growing interest in recent years [126]. Flexible and stretchable patch sensors [127] provide a very accurate mapping on a small area. In garments, metal wires have been locally woven into fabrics to build resistive temperature sensors [128, 129]. Another approach encapsulates small thermistors and incorporates them into fabrics, either through weaving [130], or inside channels built in the fabric [131, 132]. The thermistor approach is interesting as it allows for localized sensing, while keeping the sensor mechanically protected, and insensitive to humidity, compared to weaving a metal wire. However, none of these studies demonstrates direct knitting of the device, which would allow for close contact to the skin, easy fabrication and large fabric elasticity. In this section, we set out to propose such a solution.

### 7.3.2 Temperature sensing fibers

Temperature sensing fibers were made using the process presented in section 7.1. We connected thermistors (NTC Thermistor 2k 0201 from Panasonic Electronic Components) in series with a 40$\mu$m silver-coated copper wire, through soldering. Because these fiber would be knitted, we prepared a cylindrical COCe preform. The channel was also cylindrical, for several reasons:

- The thermistors have a square cross-section (0.3x0.3mm), so it is not possible to draw them in a thin rectangular channel.
- We can readily used the principles derived in 6.2.6 for knitting.
- Helical buckling in the cylindrical channel leads to a lower wire curvature, which is beneficial for fatigue life.

Thirty thermistors were successfully be drawn at once, in a 50m long continuous fiber, with the devices sliding in the channel (Figure 7-9). The fiber was then cut into different sections and the wire was buckled following the process established in chapter 4. To be knitted, the fibers were wrapped in a polyester thread as in section

6.2.5.


Figure 7-9: Photograph of a temperature sensing fiber with a thermistor connected to buckled electrodes.

Characterization of the temperature sensing properties of the wrapped fibers is presented in figure 7-10. We first calibrate the temperature sensitivity of the fibers by placing them in the cell of a dry bath heater at a controlled temperature, along with a thermometer. After waiting for thermal equilibrium (20 minutes), we record the temperature from the thermometer and the resistance of the thermistor. The fibers show an exponential temperature-resistance relationship, similar to a bare thermistor. Compared to a linear relationship, this provides additional sensitivity. Additionally, we evaluate the response time of our fibers. The fiber is held with the thermometer at room temperature, and suddenly plunged into the cell of the dry bath heater. On figure 7-10b, we see that, for a temperature difference of 4°C, between 20°C and 24°C, the fiber reaches 23.5°C (75% of total temperature change) within less than 3s. Equilibrium at 24°C is reached after one minute. Considering that skin temperature changes usually take place over several minutes, the response time of our wrapped fibers is well-fitted for skin temperature monitoring.

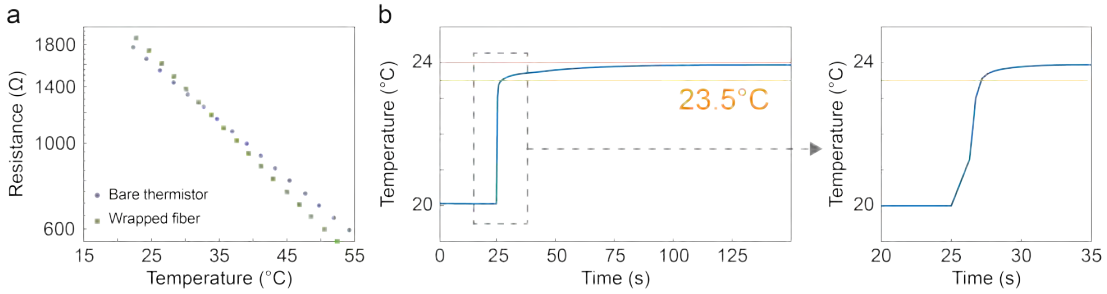


Figure 7-10: Characterization of the temperature sensing fibers. (**a**) Temperature - resistance calibration for a bare thermistor and a fiber with thermistor wrapped in polyester thread (log scale on the resistance axis). (**b**) Temperature measurement from a wrapped fiber upon sudden temperature change. The fiber was plunged into the 24°C heater at t=25s.

### 7.3.3 Knitting of a temperature sensing fabric

The wrapped temperature-sensing fibers were knitted along with cotton (Pearl cotton 3/2 from Halcyon) yarn into fabric samples. By applying the design principles determined in 6.2.6, we were able to knit the fibers and maintain the integrity of the electrodes and devices. We used fibers with a thickness-to-radius ratio $\chi = 0.46$, tube radius $a = 0.37$mm and a fiber elasticity $\eta_{metal} = 75\%$. Figure 7-11a shows a close up image of a knitted fiber, with the location of the device marked in black. A 10cmx10cm flat panel with two temperature sensing units was rolled and sewn into a tube to serve as a sleeve to measure wrist temperature (Figure7-11b).

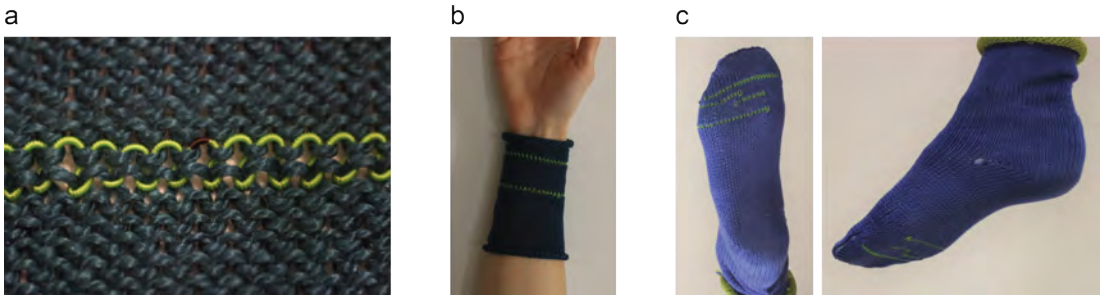


Figure 7-11: Photographs of temperature sensing fabrics. (**a**) Cotton temperature sensing fabric with a temperature sensing fiber. The location of the sensor is marked in black on the fiber. (**b**) Cotton temperature sensing fabric with two sensors, sewn into a sleeve. (**c**) Knitted sock (50%cotton - 50% bamboo yarn) with 4 temperature sensing fibers knitted into the sole.

In addition, we showed that the temperature sensing fibers could be incorporated into complex knitting structure by knitting them into a sock. We added a second knitting bed to our knitting machine to enable tubular knitting. The temperature sensing sock was knitted in a single piece, using a 50% cotton 50% Bamboo yarn (Bamboo Pop). As seen on figure 7-11c, four temperature sensing fibers were knitted in the sole of the sock. Only the fiber closest to the toes worked after knitting. Although the conditions for tubular knitting have to be adjusted, we see that our process enables knitting of functional fibers beyond just flat weft knitting.

### 7.3.4 Characterization

A flat sample of knitted temperature sensing fabric was placed on a hot plate heated at 30°C to reproduce typical skin temperature. To imitate the contact between a garment and the body, the fabric was laid flat, but no extra pressure was applied (which would result in closer contact with the plate). We mimicked local changes in skin temperature by placing heating or cooling elements, 1.5cm away from the thermistor. For heating, we used a loop of heating metal wire that we inserted between the hot plate and the fabric. For cooling, we placed an ice-cube on top of the fabric. Figure 7-12 displays the changes in temperature recorded by a thermistor in the fabric. For reference, we also measured the temperature on top of the fabric at the location of the sensor, using an infrared thermometer, before placing or removing the hot wire and the ice cube. We can notice that the temperature on the outside of the fabric does not vary as much as the temperature inside of it, due to the surrounding air. This illustrates the importance of placing the temperature sensors as close to the skin as possible. With sensors on the outside of the fabric, small changes in skin temperature could not be detected, especially if they are further away from the sensor.

From our measurements, we see that the fabric can faithfully and quickly detect local changes in surface temperature. Then by knitting an denser array of thermistors, we could use this type of fabric to map body temperature and quickly detect and localize abnormalities such and inflammations or frostbites.

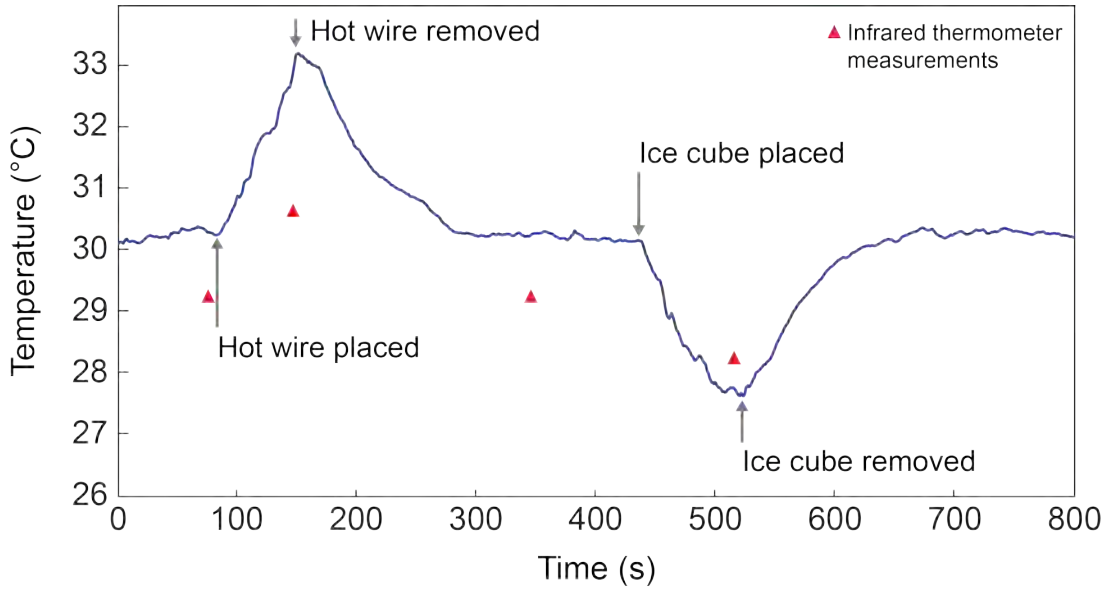


Figure 7-12: Temperature measurement from the knitted fabric placed on a hot plate. The red triangles indicate temperatures measured on top of the fabric with an infrared thermometer

## 7.4 Discussion and next steps

We have shown that, through pre-connection of micro devices, we can readily add functionality to elastic fibers with buckled electrodes. The main limitation of such an approach is the size of available devices, as the fibers should not be too large, especially if one intends to knit them. LEDs and thermistors exist in very small form factors, which enabled us to demonstrate two fabric systems. First we fabricated a textile LiFi antenna, that can detect optical signals from almost any direction, and show no signal distortion when it is stretched. Second, we made the first fully knitted garment with localized temperature sensing capability. These two proofs-of-concept could easily be perfected. It would be interesting, for example, to test their washability. In addition, the fast analysis of recorded data, as well as their transmission to a mobile device, constitute a whole field that we have not explored. This could be enabled by attaching a miniaturized circuit board to the fabric, but a much more elegant solution would incorporate memory chips and/or emitters such as RF chips, in the fiber itself. In reality, our device integration process is not limited to a single type of device, and multiple functionalities can be included in a single fiber,

and in a single fabric via proper connection of the different fiber. We foresee that, in future work, the back end connections of the different fibers will represent the main challenge.

# Chapter 8

# Conclusions and future directions

This thesis explores the process of making fabric systems using thermally drawn functional fibers. It starts by identifying elasticity as a fundamental requirement for textile fibers. It then goes through each step of design and fabrication of a fabric system. First, drawing of elastomeric materials enables fibers with an elastic cladding. Then, electrodes with high elasticity and high conductivity are added to these elastic fibers. Two approaches are proposed, relying on buckled or helical metal electrodes. Later, these fibers with elastic electrodes are utilized, along with traditional yarns, to build fabrics through weaving and knitting. Through all of these steps, experimental and analytical results are harnessed, to derive principles that can guide the design and fabrication of functional fibers and fabrics, regardless of their end purpose. Finally, a method is proposed to add micro-devices to fibers with buckled electrodes and two examples of systems are demonstrated: a woven fabric antenna, and a knitted temperature sensing garment. This work will be regarded as a success if, in the future, somebody who is making a functional textile for a specific purpose can come to it, and find useful tools and tips for his project. In this conclusion chapter we wish to expand upon opportunities to extend the reach of this work, and point at potential future interesting research studies or applications.

## 8.1 Leveraging materials and mechanics

### New materials

We demonstrated our methods using two elastomers, COCe and SEBS, and using copper or tungsten wires as electrodes. Exploring different polymers would broaden the set of mechanical and optical properties of the fibers. In addition, finding cladding materials with very different draw temperature would make a wider range of active materials available. For instance, a low temperature draw could allow for hydrogels to be drawn. On the opposite, a high temperature draw could give access to a variety of elastomer-nanoparticles composites, which require a higher temperature to flow. Furthermore. the twisting or buckling approach is not restricted to metal electrodes. For buckling, any material that comes as a wire could be used. In particular, buckling of carbon nanotube filaments would be an interesting avenue to explore. The twisting approach does not even require a material to exist in a wire form: any material that could be drawn as a straight, off-centered filament, could then be twisted into a helix. We think that this approach could be particularly useful for semiconductors.

### Three levels of control for mechanical properties

Our work highlighted at least three levels of control for mechanical properties: when drawing an elastomer, when fabricating the electrode, in particular with the helical approach, and when making the fabric, through the choice of a weaving or knitting pattern. Fabrics with mechanical properties that vary along their surface are of great interest for applications such as supportive or compression garments, exoskeletons or fabric-reinforced composites. Here we have the opportunity to create a gradient of mechanical properties in the fibers as well as in the fabric, which could effectively be leveraged in structural fabrics.

## 8.2 Textile manufacturing processes

While demonstrating weaving thermally drawn fibers along with elastic yarns, and knitting them for the first time, this work only scratches the surface of textile making.

### Weaving

Weaving thermally drawn fibers both is the warp and weft direction would allow to build a real network of functional fibers. By designing local surface connections between the fibers that cross, it would be possible to benefit from this network to reach more advanced functions.

### Knitting

Knitting being a complex process, more work should be focused on detailing the mechanical constraints applied to a yarn in a knitting machine. In the context of our study, extending the analysis of kinking to non-tubular fibers would be the first step. In addition, one should explore different knitting pattern and different knitting machines such as double bed or warp knitting.

### Industrial machines

Both for weaving and knitting, it would be interesting to transfer the principles established in this thesis to industrial apparatuses, such as a Jacquard loom and an automatic circular knitting machine.

## 8.3 Alternative methods to build functionality into elastic fibers

### 8.3.1 Buckled electrode in contact with a conductive surface

In this thesis we added functionality to our fibers by connecting micro devices via buckled electrodes. In thermally drawn fibers, it is more common to build a continuous fiber device, using a specific cross-sectional arrangement of materials. The role of the metal electrodes is to carry electricity along the whole fiber device. They need to be continuous, and to be in contact with the cross-sectional structure. It would be particularly interesting to study the use of buckled electrodes in this context. For example, if we consider a fiber with a capacitive structure such as the one depicted in figure 8-1, we could have two channels with buckled electrodes in contact with the capacitor plates made of an elastic conductive polymer nanocomposite. Then, the ability of the wires to serve as electrodes would depend on the density of contact points between the metal and the conductive polymer. Studying such a problem could open the door to new structures for elastic fibers.

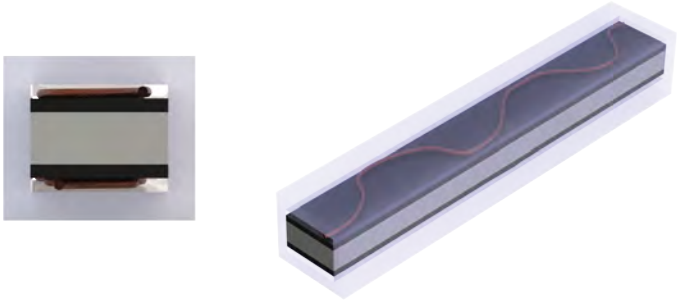

Figure 8-1: Cross-section and side view of a hypothetical capacitive elastic fiber: a dielectric material (grey) is sandwiched between two layers of a conductive elastomer nanocomposite (black). Each conductive layer forms one wall of a channel in which a buckled copper electrode lies.

### 8.3.2 Fully helical fiber

As explained in section 8.1, the twisting method is not limited to metal wires. Hence, one could design a fiber cross-section such that any material that is not intrinsically soft and highly elastic (metals, semiconductors, stiff polymer) is off-centered. Then by twisting the fiber, all stiff materials would follow a helical path. This approach would benefit greatly from a deeper analysis of the mechanics of helical fibers, and Finite Element Modelling would probably be the most appropriate tool to study such a complex system.

## 8.4 Fabric systems

Some areas of application would immediately benefit from the emergence of highly elastic electrodes

### Actuating fabric

Actuation is an obvious case where the ability to deform is key. Most designs of actuating fibers would require current to be carried along the fiber, either for Joule heating, to generate an electric or magnetic field... In particular, fibers that can actively extend or shrink axially require compliant and elastic electrodes, and are a promising opportunity for creating artificial muscles.

### Medical implants

Fabrics are already widely used inside the human body. For instance, after removing a brain tumor, a fabric is placed along the side of the cavity to stop bleeding and help the scarring process. The extraordinary compliance of fabrics makes them easy to fold or wrap around organs without damaging these. In addition, fabrics are porous membranes by construction, which is shown to be beneficial for cell growth. [133]. Furthermore, in industry, TPEs are actively being developed and tested for biocompatibility, in order to use them in medical implants. Lubrizol Health is an

example of a company that offers a wide range of biocompatible TPEs (Pellethane ©). Leveraging the development of biocompatible TPEs, one could explore functional medical implants in the form of textile, such as a light emitting fabric for optogenetics.

## Back end and data

Finally we want to highlight what we think will soon become the main challenge in making fabric systems: back end connection and data treatment. Functional fibers require a power source (which could also be a fiber) and a mean to exchange data with a computer or a mobile devices. Encompassing computing capabilities and emitters within the fiber would avoid having to attach a miniaturized circuit board to the fabric, and appears as the next big step toward fabric systems.

# Appendix A

# Draw-induced buckling

## Elastic strain in the draw

Typically, viscous deformation in the necking zone is assumed to be the only type of deformation during thermal drawing [21, 134]. However, when drawing elastomers, elastic deformation also plays a significant role both in and below the necking zone as the fiber is pulled by the capstan and stretched (see figure A-1a). In the necking zone, because the melted polymer is not a viscous fluid but a viscoelastic fluid, both viscous and elastic deformation happen. Below the necking zone, between the furnace and the capstan, the thin solid elastomeric fiber is pulled under a certain stress: this stress also generates strain in the cladding.

The amount of elastic strain induced in the draw, $\varepsilon_{clad}$, can be increased by changing the ratio of elastic to viscous deformation in the necking zone, which is quantified by the Weissenberg number of the flow [135]:

$$W_i = \tau U / L \tag{A.1}$$

Where *tau* is the relaxation rate of the polymer ($s^{-1}$), $U$ is the speed of deformation ($m{\cdot}s^{-1}$), or the speed of the capstan pulling on the fiber, and $L$ is the characteristic length of deformation, or the diameter of the preform. To increase $W_i$, one can either decrease the temperature, which increases $\tau$, or increase the draw speed $U$. However,

if $W_i$ is too high, elastic deformation will dominate over viscous deformation in the draw, which leads to the fiber breaking. In practice, increasing the Weissenberg number is equivalent to increasing the stress during the draw. This stress will also result in more elongation in the bottom part of the draw. Hence, the higher the draw stress, the higher $\varepsilon_{clad}$. Experimentally, we found that the level of strain induced during the draw remains below 10%.

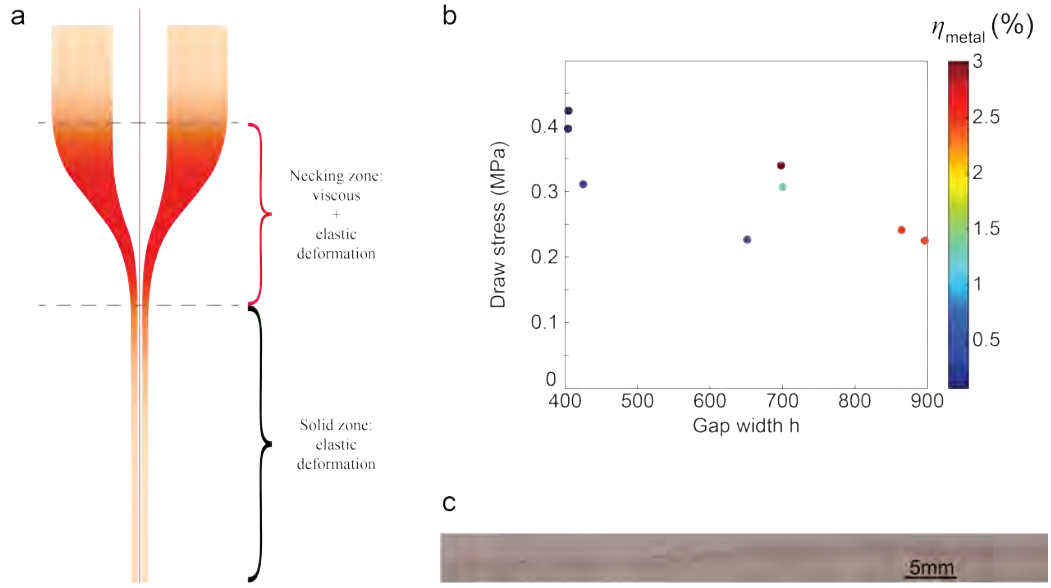


Figure A-1: (**a**) Modes of deformation of the cladding during the draw, in and below the necking zone. (**b**) Draw-induced buckling, quantified by $\eta_{metal}$, for a 50$\mu$m copper electrode in COCe, depending on the draw stress and size of the gap. (**c**) Photograph of a fiber with 3% of draw-induced elasticity.

## Relaxation and buckling after the capstan

For the cladding strain to result in buckling of the electrode, the relaxation force of the elastomer needs to be transmitted to the wire and compress it. In a roller set up, the rollers enforce the compression by clamping the cladding and the wire together. In a regular draw, the cladding relaxes as it comes out of the capstan. One end of the fiber is pinched by the capstan but the other one is not. Hence, the compressive force is only transmitted to the wire through friction between the shrinking elastomer and the wire. This has two practical consequences. First, the compressive force is much

lower, because the wire is only in contact with the walls of the gap (whichever walls) in some points and sections, but not through the whole length. Second, friction is shown to increase the buckling load [136, 112]. As a result, for the same cladding strain, much less buckling will be induce through friction than through pinching both ends of the wire

In summary, draw-induced buckling involves less cladding strain, and less buckling for an equivalent cladding strain. Figure A-1b shows the level of electrode elasticity, $\eta_{metal}$, achieved during the draw, depending on the measured draw stress and the width of the channel (as smaller channels lead to less buckling, see section 4.4.2). In our experiments, we were only able to induce up to 3% buckling during the draw, which is why our work focuses on post-draw buckling.

# Appendix B

# Creating helices through a rotating draw

An effective approach to create helical structures within a thermally drawn fiber is to rotate the preform while drawing it. This approach was successfully used by Zhang et al. [74] to fabricate helical SEBS-carbon black composite electrodes. The principle is simple: by rotating the preform from the top of the furnace and keeping it fixed at the bottom of the draw, where the capstan pulls the fiber, we induce a gradient in rotation speed along the draw. In the necking zone, which is the hottest zone of the draw, where the materials are in a viscous state, this rotation induces a rotational shear flow in addition to the usual tensile flow. This shear flow allows to create a helix in situ. The pitch of the final helix depends both on the draw speed and on the rotation speed of the preform. It is to be noticed that any material that is off-centered in the preform will then come out as a helix in the rotated fiber, whereas the cylindrical cladding should simply remain a cylinder. The principle of this approach is depicted in figure B-1, as well as the apparatus that we made to explore this method early in our work. A motor is held by the clamp of the draw tower and generates spinning of the preform holder. In a draw using convergence, the spool of wire is mounted on the rotating holder.

If the rotating draw successfully yielded in-fiber helical structures, we found it to not be suitable to draw metal electrodes. We first tried to rotate the preform

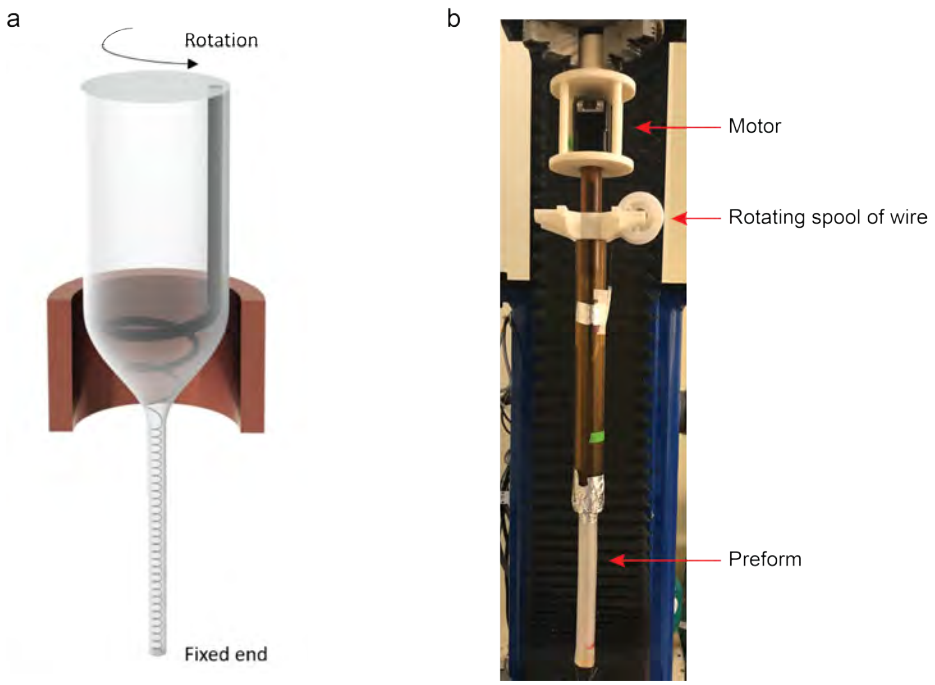


Figure B-1: Rotating draw (**a**)Principle (**b**) Apparatus

while drawing solders. Numerous attempts were made, and the most promising ones used an Indium Tin eutectic solder (InSn, $T_m = 118°C$) and SEBS for the cladding. In particular, InSn does not contain bismuth, which makes it less brittle than most low temperature solders. We managed to draw fibers with a metal helix, as seen on figure B-2a. However, although the electrode looks continuous on the side-view image, resistance measurements revealed that it was broken. We believe the elongation that the fiber undergoes between the furnace and the capstan (see appendix A) is larger than what the helical electrode could bear.

We then tried to rotate the preform to create a helical structure while drawing a solid copper wire using convergence. Due to the tension in the wire, the solid metal cut through the soft cladding towards the center, leading to a cladding twisted around the straight wire instead of a helical wire within a straight cladding (figure B-2b). In addition, a high rotation speed is necessary to achieve a small helical pitch, and the higher the rotation speed, the more pronounced the centering of the electrode and the twisting of the cladding.

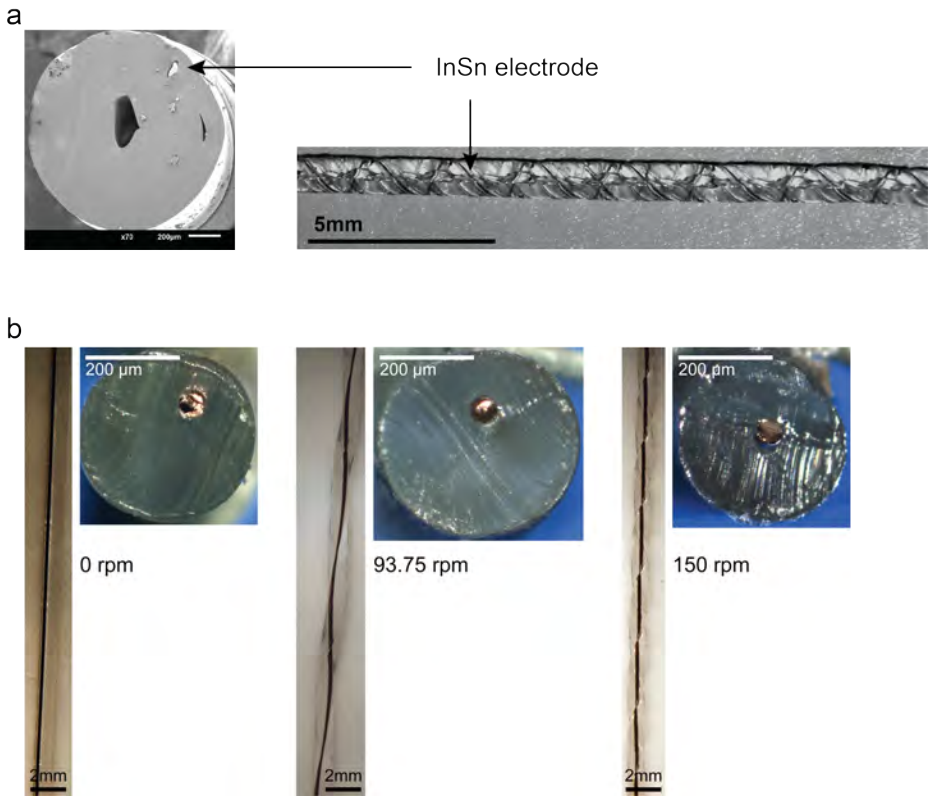


Figure B-2: Results of the rotating draw (**a**) InSn electrodes drawn while rotating the preform. SEM image of the cross section and optical image of the side view. (**b**) Fibers drawn by rotating the preform to create a helical structure while drawing a solid copper wire using convergence. Side view and cross-section for three different rotation speeds: the higher the rotation speed, the more pronounced the centering of the electrode and the twisting of the cladding.

# Bibliography


[1] Kathryn C. Mitchell. Abrasion testing of candidate outer-layer fabrics for lunar extravehicular activity space suits. In *40th International Conference on Environmental Systems, ICES 2010*. 2010.

[2] Ying Chih Lai, Jianan Deng, Steven L. Zhang, Simiao Niu, Hengyu Guo, and Zhong Lin Wang. Single-Thread-Based Wearable and Highly Stretchable Triboelectric Nanogenerators and Their Applications in Cloth-Based Self-Powered Human-Interactive and Biomedical Sensing. *Advanced Functional Materials*, pages 1–10, 2016.

[3] Shayan Seyedin, Joselito M. Razal, Peter C. Innis, Ali Jeiranikhameneh, Stephen Beirne, and Gordon G. Wallace. Knitted Strain Sensor Textiles of Highly Conductive All-Polymeric Fibers. *ACS Applied Materials and Interfaces*, 7(38):21150–21158, 2015.

[4] Andreas Leber, Alexis Gérald Page, Dong Yan, Yunpeng Qu, Shahrzad Shadman, Pedro Reis, and Fabien Sorin. Compressible and Electrically Conducting Fibers for Large-Area Sensing of Pressures. *Advanced Functional Materials*, 30(1):1–10, 2020.

[5] Wanchul Seung, Manoj Kumar Gupta, Keun Young Lee, Kyung Sik Shin, Ju Hyuck Lee, Tae Yun Kim, Sanghyun Kim, Jianjian Lin, Jung Ho Kim, and Sang Woo Kim. Nanopatterned textile-based wearable triboelectric nanogenerator. *ACS Nano*, 9(4):3501–3509, 2015.

[6] Junwen W Zhong, Yan Zhang, Qize Z Zhong, Qiyi Y Hu, Bin Hu, Zhong Lin Wang, Jun Zhou, Zhong LinWang, Jun Zhou, Zhong Lin Wang, and Jun Zhou. Fiber-Based Generator for Wearable Electronics and Mobile Medication. *ACS Nano*, 8(6):6273–6280, 2014.

[7] Zhibin Yang, Jue Deng, Xuli Chen, Jing Ren, and Huisheng Peng. A Highly Stretchable, Fiber-Shaped Supercapacitor. *Angewandte Chemie*, 125(50):13695–13699, 2013.

[8] Yongping Fu, Xin Cai, Hongwei Wu, Zhibin Lv, Shaocong Hou, Ming Peng, Xiao Yu, and Dechun Zou. Fiber supercapacitors utilizing pen ink for flexible/wearable energy storage. *Advanced Materials*, 24(42):5713–5718, 2012.

[9] Wei Zeng, Lin Shu, Qiao Li, Song Chen, Fei Wang, and Xiao Ming Tao. Fiber-based wearable electronics: A review of materials, fabrication, devices, and applications. *Advanced Materials*, 26(31):5310–5336, 2014.

[10] Matteo Stoppa and Alessandro Chiolerio. Wearable electronics and smart textiles: A critical review. *Sensors (Switzerland)*, 14(7):11957–11992, 2014.

[11] Samuel Poincloux, Mokhtar Adda-Bedia, and Frédéric Lechenault. Geometry and Elasticity of a Knitted Fabric. *Physical Review X*, 8(2):1–14, 2018.

[12] Shun Chen, Xiao Tian, Tao Hua, Kahei Chan, Jimin Fu, and Ben Niu. Exploring the relationship between applied fabric strain and resultant local yarn strain within the elastic fabric based on finite element method. *Journal of Materials Science*, 55(23):10258–10270, 2020.

[13] F. Boussu, N. Trifigny, C. Cochrane, and V. Koncar. Fibrous sensors to help the monitoring of weaving process. *Smart Textiles and Their Applications*, pages 375–400, 2016.

[14] Waqar Iqbal, Yaming Jiang, Ye Xiong Qi, and Lei Xu. Yarn Damage Evaluation in the Flat Knitting Process. *Autex Research Journal*, 2020.

[15] Darren J. Lipomi. Stretchable Figures of Merit in Deformable Electronics. *Advanced Materials*, pages 1–4, 2015.

[16] Burak Temelkuran, Shandon D. Hart, Gilles Benoit, John D. Joannopoulos, and Yoel Fink. Wavelength-scalable hollow optical fibres with large photonic bandgaps for CO2 laser transmission. *Nature*, 420(6916):650–653, 2002.

[17] Gabriel Loke, Rodger Yuan, Michael Rein, Tural Khudiyev, Yash Jain, John Joannopoulos, and Yoel Fink. Structured multimaterial filaments for 3D printing of optoelectronics. *Nature Communications*, 10(1), 2019.

[18] Tural Khudiyev, Jung Tae Lee, Jason R. Cox, Eric Argentieri, Gabriel Loke, Rodger Yuan, Grace H. Noel, Ryoichi Tatara, Yang Yu, Frannie Logan, John Joannopoulos, Yang Shao-Horn, and Yoel Fink. 100 m Long Thermally Drawn Supercapacitor Fibers with Applications to 3D Printing and Textiles. *Advanced Materials*, 32(49), 2020.

[19] Tural Khudiyev, Benjamin Grena, Gabriel Loke, Chong Hou, Hyeonji Jang, Jinhyuk Lee, Grace H. Noel, Juliette Alain, John Joannopoulos, Kang Xu, Ju Li, Yoel Fink, and Jung Tae Lee. Thermally drawn rechargeable battery fiber enables pervasive power. *Materials Today*, 52(xx):80–89, 2022.

[20] Andres Canales, Xiaoting Jia, Ulrich P. Froriep, Ryan A. Koppes, Christina M. Tringides, Jennifer Selvidge, Chi Lu, Chong Hou, Lei Wei, Yoel Fink, and Polina Anikeeva. Multifunctional fibers for simultaneous optical, electrical and chemical interrogation of neural circuits in vivo. *Nature Biotechnology*, 33(3):277–284, 2015.

[21] A F Abouraddy, M Bayindir, G Benoit, S D Hart, K Kuriki, N Orf, O Shapira, F Sorin, B Temelkuran, and Y Fink. Towards multimaterial multifunctional fibres that see, hear, sense and communicate. *Nature Materials*, 6(May):336, 2007.

[22] Gabriel Loke, Wei Yan, Tural Khudiyev, Grace Noel, and Yoel Fink. Recent Progress and Perspectives of Thermally Drawn Multimaterial Fiber Electronics. *Advanced Materials*, 32(1), 2020.

[23] Wei Yan, Grace Noel, Gabriel Loke, Elizabeth Meiklejohn, Tural Khudiyev, Juliette Marion, Guanchun Rui, Jinuan Lin, Juliana Cherston, Atharva Sahasrabudhe, Joao Wilbert, Irmandy Wicaksono, Reed W Hoyt, Anais Missakian, Lei Zhu, Chu Ma, John Joannopoulos, and Yoel Fink. Single fibre enables acoustic fabrics via nanometre-scale vibrations. *Nature* /, 603:616, 2022.

[24] Michael Rein, Valentine Dominique Favrod, Chong Hou, Tural Khudiyev, Alexander Stolyarov, Jason Cox, Chia Chun Chung, Chhea Chhav, Marty Ellis, John Joannopoulos, and Yoel Fink. Diode fibres for fabric-based optical communications. *Nature*, 560(7717):214–218, 2018.

[25] Seongjun Park, Yuanyuan Guo, Xiaoting Jia, Han Kyoung Choe, Benjamin Grena, Jeewoo Kang, Jiyeon Park, Chi Lu, Andres Canales, Ritchie Chen, Yeong Shin Yim, Gloria B. Choi, Yoel Fink, and Polina Anikeeva. One-step optogenetics with multifunctional flexible polymer fibers. *Nature Neuroscience*, 20(4):612–619, 2017.

[26] Marc Joseph Antonini, Atharva Sahasrabudhe, Anthony Tabet, Miriam Schwalm, Dekel Rosenfeld, Indie Garwood, Jimin Park, Gabriel Loke, Tural Khudiyev, Mehmet Kanik, Nathan Corbin, Andres Canales, Alan Jasanoff, Yoel Fink, and Polina Anikeeva. Customizing MRI-Compatible Multifunctional Neural Interfaces through Fiber Drawing. *Advanced Functional Materials*, 31(43):1–15, 2021.

[27] German Alberto Parada and Xuanhe Zhao. Soft Matter rsc.li/soft-matter-journal Ideal reversible polymer networks. *Soft Matter*, 14:5186, 2018.

[28] Richard J. Spontak and Nikunj P. Patel. Thermoplastic elastomers: fundamentals and applications. *Current Opinion in Colloid & Interface Science*, 5(5-6):333–340, 11 2000.

[29] Chi Lu, Seongjun Park, Thomas J. Richner, Alexander Derry, Imogen Brown, Chong Hou, Siyuan Rao, Jeewoo Kang, Chet T. Moritz, Yoel Fink, and Polina Anikeeva. Flexible and stretchable nanowire-coated fibers for optoelectronic probing of spinal cord circuits. *Science Advances*, 3(3), 2017.

[30] Yunpeng Qu, Tung Nguyen-Dang, Alexis Gérald Page, Wei Yan, Tapajyoti Das Gupta, Gelu Marius Rotaru, René M. Rossi, Valentine Dominique Favrod, Nicola Bartolomei, and Fabien Sorin. Superelastic Multimaterial Electronic

and Photonic Fibers and Devices via Thermal Drawing. *Advanced Materials*, 30(27):1–8, 2018.

[31] Mehmet Kanik, Sirma Orguc, Georgios Varnavides, Jinwoo Kim, Thomas Benavides, Dani Gonzales, Thimothy Akintilo, C. Cem Tasan, Anantha P. Chandrakasan, Yoel Fink, and Polina Anikeeva. Strain-programmable fiber-based artificial muscle. *Science*, 365(July):145–150, 2019.

[32] Juliette S. Marion, Nikhil Gupta, Henry Cheung, Kirmina Monir, Polina Anikeeva, and Yoel Fink. Thermally Drawn Highly Conductive Fibers with Controlled Elasticity. *Advanced Materials*, 2022.

[33] A. Peterlin. Drawing and extrusion of semi-crystalline polymers. *Colloid & Polymer Science*, 265(5):357–382, 1987.

[34] Jonathan Rivnay, Huiliang Wang, Lief Fenno, Karl Deisseroth, and George G. Malliaras. Next-generation probes, particles, and proteins for neural interfacing. *Science Advances*, 3(6), 2017.

[35] Stéphanie P. Lacour, Grégoire Courtine, and Jochen Guck. Materials and technologies for soft implantable neuroprostheses. *Nature Reviews Materials*, 1(10), 2016.

[36] James C. Barrese, Juan Aceros, and John P. Donoghue. Scanning electron microscopy of chronically implanted intracortical microelectrode arrays in non-human primates. *Journal of Neural Engineering*, 13(2), 2016.

[37] Chi Lu, Ulrich P. Froriep, Ryan A. Koppes, Andres Canales, Vittorio Caggiano, Jennifer Selvidge, Emilio Bizzi, and Polina Anikeeva. Polymer Fiber Probes Enable Optical Control of Spinal Cord and Muscle Function in Vivo. *Advanced Functional Materials*, 24(42):6594–6600, 2014.

[38] Mathias Kolle, Alfred Lethbridge, Moritz Kreysing, Jeremy J. Baumberg, Joanna Aizenberg, and Peter Vukusic. Bio-inspired band-gap tunable elastic optical multilayer fibers. *Advanced Materials*, 25(15):2239–2245, 2013.

[39] Andreas Leber, Beth Cholst, Joseph Sandt, Nicolas Vogel, and Mathias Kolle. Stretchable Thermoplastic Elastomer Optical Fibers for Sensing of Extreme Deformations. *Advanced Functional Materials*, 29(5), 2019.

[40] Huichan Zhao, Kevin O'Brien, Shuo Li, and Robert F. Shepherd. Optoelectronically innervated soft prosthetic hand via stretchable optical waveguides. *Science Robotics*, 1(1), 2016.

[41] Jingjing Guo, Xinyue Liu, Nan Jiang, Ali K. Yetisen, Hyunwoo Yuk, Changxi Yang, Ali Khademhosseini, Xuanhe Zhao, and Seok Hyun Yun. Highly Stretchable, Strain Sensing Hydrogel Optical Fibers. *Advanced Materials*, 28(46):10244–10249, 2016.

[42] Hyelim Kim and Sunhee Lee. Electrical heating properties of various electro-circuit patterns coated on cotton fabric using graphene/polymer composites. *Textile Research Journal*, 89(19-20):4114–4130, 2019.

[43] Takeo Yamada, Yuhei Hayamizu, Yuki Yamamoto, Yoshiki Yomogida, Ali Izadi-Najafabadi, Don N Futaba, and Kenji Hata. A stretchable carbon nanotube strain sensor for human-motion detection. *Nature Nanotechnology*, 6(5):296–301, 2011.

[44] C. Shemelya, F. Cedillos, E. Aguilera, E. Maestas, J. Ramos, D. Espalin, D. Muse, R. Wicker, and E. MacDonald. 3D printed capacitive sensors. In *Proceedings of IEEE Sensors*, pages 1–4, 11 2013.

[45] Tran Quang Trung and Nae Eung Lee. Recent Progress on Stretchable Electronic Devices with Intrinsically Stretchable Components. *Advanced Materials*, 29(3), 2017.

[46] Jianyong Ouyang. Application of intrinsically conducting polymers in flexible electronics. *SmartMat*, 2(3):263–285, 2021.

[47] Laure V. Kayser and Darren J. Lipomi. Stretchable Conductive Polymers and Composites Based on PEDOT and PEDOT:PSS. *Advanced Materials*, 31(10), 2019.

[48] Pengcheng Li, Kuan Sun, and Jianyong Ouyang. Stretchable and Conductive Polymer Films Prepared by Solution Blending. *ACS Applied Materials and Interfaces*, 7(33):18415–18423, 2015.

[49] Hyung Joon Shim, Sung Hyuk Sunwoo, Yeongjun Kim, Ja Hoon Koo, and Dae Hyeong Kim. Functionalized Elastomers for Intrinsically Soft and Biointegrated Electronics. *Advanced Healthcare Materials*, 2002105:1–33, 2021.

[50] Chunya Wang, Tomoyuki Yokota, and Takao Someya. Natural biopolymer-based biocompatible conductors for stretchable bioelectronics. *Chemical Reviews*, 121(4):2109–2146, 2021.

[51] Yves Bréchet, Jean Yves Y. Cavaillé, Emmanuelle Chabert, Laurent Chazeau, Rémy Dendievel, Lionel Flandin, and Catherine Gauthier. Polymer based nanocomposites: Effect of filler-filler and filler-matrix interactions. *Advanced Engineering Materials*, 3(8):571–577, 2001.

[52] Michael D. Dickey. Stretchable and Soft Electronics using Liquid Metals. *Advanced Materials*, 29(27):1–19, 2017.

[53] Adam C. Siegel, Derek A. Bruzewicz, Douglas B. Weibel, and George M. Whitesides. Microsolidics: Fabrication of three-dimensional metallic microstructures in poly(dimethylsiloxane). *Advanced Materials*, 19(5):727–733, 2007.

[54] Shu Zhu, Ju Hee So, Robin Mays, Sharvil Desai, William R. Barnes, Behnam Pourdeyhimi, and Michael D. Dickey. Ultrastretchable fibers with metallic conductivity using a liquid metal alloy core. *Advanced Functional Materials*, 23(18):2308–2314, 2013.

[55] Zhijun Ma, Qiyao Huang, Qi Xu, Qiuna Zhuang, Xin Zhao, Yuhe Yang, Hua Qiu, Zhilu Yang, Cong Wang, Yang Chai, and Zijian Zheng. Permeable superelastic liquid-metal fibre mat enables biocompatible and monolithic stretchable electronics. *Nature Materials*, 20(6):859–868, 2021.

[56] John A. Rogers, Takao Someya, and Yonggang Huang. Materials and mechanics for stretchable electronics. *Science*, 327(5973):1603–1607, 2010.

[57] Yinji Ma, Xue Feng, John A. Rogers, Yonggang Huang, and Yihui Zhang. Design and application of 'J-shaped' stress-strain behavior in stretchable electronics: A review. *Lab on a Chip*, 17(10):1689–1704, 2017.

[58] Taisong Pan, Matt Pharr, Yinji Ma, Rui Ning, Zheng Yan, Renxiao Xu, Xue Feng, Yonggang Huang, and John A. Rogers. Experimental and Theoretical Studies of Serpentine Interconnects on Ultrathin Elastomers for Stretchable Electronics. *Advanced Functional Materials*, 27(37):1–8, 2017.

[59] R Chad Webb, Andrew P Bonifas, Alex Behnaz, Yihui Zhang, Ki Jun Yu, Huanyu Cheng, Mingxing Shi, Zuguang Bian, Zhuangjian Liu, Yun-Soung Kim, Woon-Hong Yeo, Jae Suk Park, Jizhou Song, Yuhang Li, Yonggang Huang, Alexander M Gorbach, and John A Rogers. Ultrathin conformal devices for precise and continuous thermal characterization of human skin. *Nature materials*, 12(10):938–44, 2013.

[60] Kan Li, Xu Cheng, Feng Zhu, Linze Li, Zhaoqian Xie, Haiwen Luan, Zhouheng Wang, Ziyao Ji, Heling Wang, Fei Liu, Yeguang Xue, Changqing Jiang, Xue Feng, Luming Li, John A. Rogers, Yonggang Huang, and Yihui Zhang. A Generic Soft Encapsulation Strategy for Stretchable Electronics. *Advanced Functional Materials*, 29(8), 2019.

[61] Kyung In Jang, Kan Li, Ha Uk Chung, Sheng Xu, Han Na Jung, Yiyuan Yang, Jean Won Kwak, Han Hee Jung, Juwon Song, Ce Yang, Ao Wang, Zhuangjian Liu, Jong Yoon Lee, Bong Hoon Kim, Jae Hwan Kim, Jungyup Lee, Yongjoon Yu, Bum Jun Kim, Hokyung Jang, Ki Jun Yu, Jeonghyun Kim, Jung Woo Lee, Jae Woong Jeong, Young Min Song, Yonggang Huang, Yihui Zhang, and John A. Rogers. Self-assembled three dimensional network designs for soft electronics. *Nature Communications*, 8(May):1–10, 2017.

[62] Xu He, Yunlong Zi, Hengyu Guo, Haiwu Zheng, Yi Xi, Changsheng Wu, Jie Wang, Wei Zhang, Canhui Lu, and Zhong Lin Wang. A Highly Stretchable Fiber-Based Triboelectric Nanogenerator for Self-Powered Wearable Electronics. *Advanced Functional Materials*, page 1604378, 2016.

[63] Min Ju Yun, Yeon Hyang Sim, Dong Yoon Lee, and Seung I. Cha. Highly stretchable large area woven, knitted and robust braided textile based interconnection for stretchable electronics. *Scientific Reports*, 11(1):1–10, 2021.

[64] Dae-Hyeong Kim, Jong-Hyun Ahn, Won Mook Choi, Hoon-Sik Kim, Tae-Ho Kim, Jizhou Song, Younggang Y. Huang, Zhuangjian Liu, Chun Lu, and John A. Rogers. Stretchable and Foldable Silicon Integrated Circuits. *Science*, 320(April):507–511, 2008.

[65] Martin Kaltenbrunner, Tsuyoshi Sekitani, Jonathan Reeder, Tomoyuki Yokota, Kazunori Kuribara, Takeyoshi Tokuhara, Michael Drack, Reinhard Schwödiauer, Ingrid Graz, Simona Bauer-Gogonea, Siegfried Bauer, and Takao Someya. An ultra-lightweight design for imperceptible plastic electronics. *Nature*, 499(7459):458–63, 2013.

[66] Yinji Ma, Kyung In Jang, Liang Wang, Han Na Jung, Jean Won Kwak, Yeguang Xue, Hang Chen, Yiyuan Yang, Dawei Shi, Xue Feng, John A. Rogers, and Yonggang Huang. Design of Strain-Limiting Substrate Materials for Stretchable and Flexible Electronics. *Advanced Functional Materials*, 26(29):5345–5351, 2016.

[67] Qiang Ma and Yihui Zhang. Mechanics of Fractal-Inspired Horseshoe Microstructures for Applications in Stretchable Electronics. *Journal of Applied Mechanics, Transactions ASME*, 83(11):1–19, 2016.

[68] Hangfei Li, Shisheng Cai, Yingchao Zhang, Keh Chih Hwang, Yinji Ma, and Xue Feng. Local wrinkling versus global buckling of stiff film bonded to finite-thick substrate. *Extreme Mechanics Letters*, 29:100453, 2019.

[69] Noémie Chocat, Guillaume Lestoquoy, Zheng Wang, Daniel M. Rodgers, John D. Joannopoulos, and Yoel Fink. Piezoelectric fibers for conformal acoustics. *Advanced Materials*, 24(39):5327–5332, 2012.

[70] Michael Rein, Etgar Levy, Alexander Gumennik, Ayman F. Abouraddy, John Joannopoulos, and Yoel Fink. Self-assembled fibre optoelectronics with discrete translational symmetry. *Nature Communications*, 7:1–8, 2016.

[71] Guillaume Lestoquoy, Noémie Chocat, Zheng Wang, John D. Joannopoulos, and Yoel Fink. Fabrication and characterization of thermally drawn fiber capacitors. *Applied Physics Letters*, 102(15), 2013.

[72] Shai Maayani, Christopher Foy, Dirk Englund, and Yoel Fink. Distributed Quantum Fiber Magnetometry. *Laser and Photonics Reviews*, 13(7):1–7, 2019.

[73] Andreas Leber, Chaoqun Dong, Rajasundar Chandran, Tapajyoti Das Gupta, Nicola Bartolomei, and Fabien Sorin. Soft and stretchable liquid metal transmission lines as distributed probes of multimodal deformations. *Nature Electronics*, 3(6):316–326, 2020.

[74] Yujing Zhang, Xiyuan Li, Jongwoon Kim, Yuxin Tong, Emily G. Thompson, Shan Jiang, Ziang Feng, Li Yu, Jinhua Wang, Dong Sam Ha, Harald Sontheimer, Blake N. Johnson, and Xiaoting Jia. Thermally Drawn Stretchable Electrical and Optical Fiber Sensors for Multimodal Extreme Deformation Sensing. *Advanced Optical Materials*, 2001815:1–9, 2021.

[75] Herzl Chai. The post-buckling response of a bi-laterally constrained column. *Journal of the Mechanics and Physics of Solids*, 46(7):1155–1159, 1998.

[76] Wassim Borchani, Nizar Lajnef, and Rigoberto Burgueño. Energy method solution for the postbuckling response of an axially loaded bilaterally constrained beam. *Mechanics Research Communications*, 70:114–119, 2015.

[77] Pengcheng Jiao, Wassim Borchani, and Nizar Lajnef. Large deformation solutions to post-buckled beams confined by movable and flexible constraints: A static and dynamic analysis. *International Journal of Solids and Structures*, 128:85–98, 2017.

[78] Pengcheng Jiao, Wassim Borchani, Hassene Hasni, and Nizar Lajnef. Static and dynamic post-buckling analyses of irregularly constrained beams under the small and large deformation assumptions. *International Journal of Mechanical Sciences*, 124-125(October 2016):203–215, 2017.

[79] Junfeng Xiao and Xi Chen. Buckling morphology of an elastic beam between two parallel lateral constraints: Implication for a snake crawling between walls. *Journal of the Royal Society Interface*, 10(85), 2013.

[80] Yuan Liu, Xueju Wang, Yameng Xu, Zhaoguo Xue, Yi Zhang, Xin Ning, Xu Cheng, Yeguang Xue, Di Lu, Qihui Zhang, Fan Zhang, Jianxing Liu, Xiaogang Guo, Keh Chih Hwang, Yonggang Huang, John A. Rogers, and Yihui Zhang. Harnessing the interface mechanics of hard films and soft substrates for 3D assembly by controlled buckling. *Proceedings of the National Academy of Sciences of the United States of America*, 116(31):15368–15377, 2019.

[81] Siavash Nikravesh, Donghyeon Ryu, and Yu Lin Shen. Instabilities of Thin Films on a Compliant Substrate: Direct Numerical Simulations from Surface Wrinkling to Global Buckling. *Scientific Reports*, 10(1):1–19, 2020.

[82] Shuodao Wang, Jizhou Song, Dae Hyeong Kim, Yonggang Huang, and John A. Rogers. Local versus global buckling of thin films on elastomeric substrates. *Applied Physics Letters*, 93(2):1–4, 2008.

[83] J. M.T. Thompson and A. R. Cliampneys. From helix to localized writhing in the torsional post-buckling of elastic rods. *Proceedings of the Royal Society A: Mathematical, Physical and Engineering Sciences*, 452(1944):117–138, 1996.

[84] Basile Audoly and Yves Pomeau. *Elasticity and geometry: from hair curls to the non-linear response of shells*. Oxford University Press, Oxford, 2010.

[85] R. Yin, X. M. Tao, and B. G. Xu. Mathematical Modeling of Yarn Dynamics in a Generalized Twisting System. *Scientific Reports*, 6:1–13, 2016.

[86] R. Furferi, L. Governi, and Y. Volpe. A novel method for ring spinning performance evaluation based on Computer Aided analysis of yarn geometry. *International Journal of Mechanics*, 6(4):212–221, 2012.

[87] C. Lawrence. Fibre to Yarn: Filament Yarn Spinning. In Rose Sinclair, editor, *Textiles and Fashion: Materials, Design and Technology*, chapter 10, pages 191–212. Elsevier Ltd, Oxford, 2014.

[88] W. Miller, P. B. Hook, C. W. Smith, X. Wang, and K. E. Evans. The manufacture and characterisation of a novel, low modulus, negative Poisson's ratio composite. *Composites Science and Technology*, 69(5):651–655, 2009.

[89] M. R. Sloan, J. R. Wright, and K. E. Evans. The helical auxetic yarn - A novel structure for composites and textiles; Geometry, manufacture and mechanical properties. *Mechanics of Materials*, 43(9):476–486, 2011.

[90] J. R. Wright, M. R. Sloan, and K. E. Evans. Tensile properties of helical auxetic structures: A numerical study. *Journal of Applied Physics*, 108(4), 2010.

[91] Michał Kwietniewski and Danuta Miedzińska. Numerical analysis of Helical Auxetic Yarn elastomeric core tension. *AIP Conference Proceedings*, 2078(March), 2019.

[92] Ning Jiang, Yu Chen, and Hong Hu. Theoretical Modeling on the Deformation Behavior of Auxetic Tubular Braid Made from Modified Circular Braiding Technique. *Physica Status Solidi (B) Basic Research*, 257(10):1–11, 2020.

[93] S J Kadolph and S B Marcketti. *Textiles*. Pearson, 2017.

[94] Adeel Zulifqar, Zubair Khaliq, and Hong Hu. Textile Mechanics. In *Handbook of Fibrous Materials*, chapter 18, pages 455–476. John Wiley & Sons, Ltd, 2020.

[95] Quantis. Measuring Fashion 2018: Environmental Impact of the Global Apparel and Footwear Industries Study Full report and methodological considerations. Technical report, Quantis-intl.com, 2018.

[96] Tao Hua. Fabric Making Technologies. In *Handbook of Fibrous Materials*, chapter 19, pages 477–498. John Wiley & Sons, Ltd, 2020.

[97] Samir Kumar Neogi. *Role of yarn tension in weaving*. Woodhead publishing India in textiles. Woodhead Publishing India PVT. Limited, New Delhi, 2016.

[98] Nicolas Trifigny, Fern M. Kelly, Cédric Cochrane, François Boussu, Vladan Koncar, and Damien Soulat. PEDOT:PSS-based piezo-resistive sensors applied to reinforcement glass fibres for in situ measurement during the composite material weaving process. *Sensors (Switzerland)*, 13(8):10749–10764, 2013.

[99] Ali Maziz, Alessandro Concas, Alexandre Khaldi, Jonas Stålhand, Nils Krister Persson, and Edwin W.H. Jager. Knitting and weaving artificial muscles. *Science Advances*, 3(1):1–12, 2017.

[100] Stana Kovačevič, Krešimir Hajdarović, and Ana Marija Grancarić. Influence of Warp Loading on Weaving Machines upon Yarn Deformation. *Textile Research Journal*, 70(7):603–610, 2000.

[101] H. Nosraty, Ali A.A. Jeddi, and M. Jamshidi Avanaki. Fatigue Behavior of Filament Warp Yarns under Cyclic Loads during Weaving Process. *Textile Research Journal*, 79(2):154–165, 2009.

[102] Kunigunde H. Cherenack, Thomas Kinkeldei, Christoph Zysset, and Gerhard Troster. Woven Thin-Film metal interconnects. *IEEE Electron Device Letters*, 31(7):740–742, 2010.

[103] K Greenwood. RELAXATION PHENOMENA IN WEAVING. *Journal of the Textile Institute Proceedings*, 48(3):P206–P213, 1957.

[104] D J Spencer. *Knitting Technology: A Comprehensive Handbook and Practical Guide*. Woodhead Publishing series in textiles. Technomic publishing, Lancaster, Pensylvania, 2001.

[105] Jiaqing Xiong, Jian Chen, and Pooi See Lee. Functional Fibers and Fabrics for Soft Robotics, Wearables, and Human–Robot Interface. *Advanced Materials*, 2002640:1–43, 2020.

[106] Wenjing Fan, Qiang He, Keyu Meng, Xulong Tan, Zhihao Zhou, Gaoqiang Zhang, Jin Yang, and Zhong Lin Wang. Machine-knitted washable sensor array textile for precise epidermal physiological signal monitoring. *Science Advances*, 6(11):1–11, 2020.

[107] Rajesh Mishra and Michal Petru. Application of knitted fabrics in textile structural composites. In Subhankar Maity, Sohel Rana, Pintu Pandit, and Kunal Singha, editors, *Advanced Knitting Technology*, The Textile Institute Book Series, pages 411–470. Woodhead Publishing, 2021.

[108] Julianna Abel, Jonathan Luntz, and Diann Brei. Hierarchical architecture of active knits. *Smart Materials and Structures*, 22(12), 2013.

[109] Xing Liu and Xuhong Miao. Analysis of yarn tension based on yarn demand variation on a tricot knitting machine. *Textile Research Journal*, 87(4):487–497, 2017.

[110] V. Svetnickiene and Ricardas Čiukas. Technical and classical yarns friction properties investigation. *Mechanika*, 60(4):54–58, 2006.

[111] J. T. Miller, T. Su, E. B. Dussan V., J. Pabon, N. Wicks, K. Bertoldi, and P. M. Reis. Buckling-induced lock-up of a slender rod injected into a horizontal cylinder. *International Journal of Solids and Structures*, 72:153–164, 2015.

[112] Tianxiang Su, Nathan Wicks, Jahir Pabon, and Katia Bertoldi. Mechanism by which a frictionally confined rod loses stability under initial velocity and position perturbations. *International Journal of Solids and Structures*, 50(14-15):2468–2476, 2013.

[113] L G Brazier. On the flexure of thin cylindrical shells and other "thin" sections. *Proceedings of the Royal Society of London. Series A, Containing Papers of a Mathematical and Physical Character*, 116(773):104–114, 1927.

[114] F. A. Emmerling. Nonlinear Bending of Curved Tubes. *Flexible Shells*, pages 175–191, 1984.

[115] Lei Chen. Nonlinear stability analysis of elastic cylinders under global bending. *Applied Mechanics and Materials*, 638-640:1754–1757, 2014.

[116] T. Vodenitcharova and L. C. Zhang. Mechanism of bending with kinking of a single-walled carbon nanotube. *Physical Review B - Condensed Matter and Materials Physics*, 69(11):1–7, 2004.

[117] Animangsu Ghatak and Apurba Lal Das. Kink instability of a highly deformable elastic cylinder. *Physical Review Letters*, 99(7), 2007.

[118] C R Calladine. *Theory of Shell Structures*. Cambridge University Press, 1983.

[119] Barbara Hepworth. 13—The biaxial load-extension behaviour of a model of plain weft-knitting—part I. *Journal of the Textile Institute*, 69(4):101–107, 1978.

[120] Željko Penava, Diana Šimić Penava, and Lozo Miloš. Experimental and analytical analyses of the knitted fabric off-axes tensile test. *Textile Research Journal*, 91(1-2):62–72, 2021.

[121] W J Shanahan and R Postle. 23—A THEORETICAL ANALYSIS OF THE TENSILE PROPERTIES OF PLAIN-KNITTED FABRICS. PART I: THE LOAD-EXTENSION CURVE FOR FABRIC EXTENSION PARALLEL TO THE COURSES. *The Journal of The Textile Institute*, 65(4):200–212, 1974.

[122] W J Shanahan and R Postle. 28—A THEORETICAL ANALYSIS OF THE TENSILE PROPERTIES OF PLAIN-KNITTED FABRICS. PART II: THE INITIAL LOAD-EXTENSION BEHAVIOUR FOR FABRIC EXTENSION PARALLEL TO THE WALES. *The Journal of The Textile Institute*, 65(5):254–260, 1974.

[123] Gilles Dusserre, Laura Balea, and Gérard Bernhart. Elastic properties prediction of a knitted composite with inlaid yarns subjected to stretching: A coupled semi-analytical model. *Composites Part A: Applied Science and Manufacturing*, 64:185–193, 2014.

[124] Sicco A. Bus, Wouter B. Aan De Stegge, Jeff G. Van Baal, Tessa E. Busch-Westbroek, Frans Nollet, and Jaap J. Van Netten. Effectiveness of at-home skin temperature monitoring in reducing the incidence of foot ulcer recurrence in people with diabetes: A multicenter randomized controlled trial (DIATEMP). *BMJ Open Diabetes Research and Care*, 9(1):1–11, 2021.

[125] Ian L. Gordon, Gary M. Rothenberg, Brian D. Lepow, Brian J. Petersen, David R. Linders, Jonathan D. Bloom, and David G. Armstrong. Accuracy of a foot temperature monitoring mat for predicting diabetic foot ulcers in patients with recent wounds or partial foot amputation. *Diabetes Research and Clinical Practice*, 161:108074, 2020.

[126] Qiao Li, Li Na Zhang, Xiao Ming Tao, and Xin Ding. Review of Flexible Temperature Sensing Networks for Wearable Physiological Monitoring. *Advanced Healthcare Materials*, 6(12), 2017.

[127] Qilin Hua, Junlu Sun, Haitao Liu, Rongrong Bao, Ruomeng Yu, Junyi Zhai, Caofeng Pan, and Zhong Lin Wang. Skin-inspired highly stretchable and conformable matrix networks for multifunctional sensing. *Nature Communications*, 9(1):1–11, 2018.

[128] Muhammad Dawood Husain and Richard Kennon. Preliminary investigations into the development of textile based temperature sensor for healthcare applications. *Fibers*, 1(1):2–10, 2013.

[129] Qiao Li, Hui Chen, Zi Yuan Ran, Li Na Zhang, Rui Fang Xiang, Xi Wang, Xiao Ming Tao, and Xin Ding. Full fabric sensing network with large deformation for continuous detection of skin temperature. *Smart Materials and Structures*, 27(10):105017, 2018.

[130] Pasindu Lugoda, Theodore Hughes-Riley, Rob Morris, and Tilak Dias. A wearable textile thermograph. *Sensors (Switzerland)*, 18(7):1–22, 2018.

[131] Abiodun Komolafe, Russel Torah, Helga Nunes-Matos, Michael Tudor, and Steve Beeby. Integration of temperature sensors in fabrics. *FLEPS 2019 - IEEE International Conference on Flexible and Printable Sensors and Systems, Proceedings*, pages 30–31, 2019.

[132] Irmandy Wicaksono, Carson I. Tucker, Tao Sun, Cesar A. Guerrero, Clare Liu, Wesley M. Woo, Eric J. Pence, and Canan Dagdeviren. A tailored, electronic textile conformable suit for large-scale spatiotemporal physiological sensing in vivo. *npj Flexible Electronics*, 4(1), 2020.

[133] Dena Shahriari, Gabriel Loke, Ian Tafel, Seongjun Park, Po Han Chiang, Yoel Fink, and Polina Anikeeva. Scalable Fabrication of Porous Microchannel Nerve Guidance Scaffolds with Complex Geometries. *Advanced Materials*, 31(30):1–8, 2019.

[134] Alexis G. Page, Mathias Bechert, François Gallaire, and Fabien Sorin. Unraveling radial dependency effects in fiber thermal drawing. *Applied Physics Letters*, 115(4), 2019.

[135] Rob Poole. THE BRITISH SOCIETY OF RHEOLOGY The Deborah and Weissenberg numbers. *Rheology Bulletin*, 53(2):32–39, 2012.

[136] Guohua Gao and Stefan Miska. Effects of friction on post-buckling behavior and axial load transfer in a horizontal well. *SPE Journal*, 15(4):1110–1124, 2010.